NTNU
Norwegian University of
Science and Technology

Scanning Precession Electron Diffraction Study of 2xxx Series Aluminium Alloys Exhibiting Several Coexisting Strengthening Phases

Jonas Kristoffer Sunde

Master of Science in Physics and Mathematics
Submission date: June 2016
Supervisor: Randi Holmestad, IFY
Co-supervisor: Sigurd Wenner, IFY

Norwegian University of Science and Technology
Department of Physics

Abstract

In this master's thesis, the technique of scanning precession electron diffraction (SPED) within the field of transmission electron microscopy (TEM), has been applied in the study of two high solute 2xxx series Al alloys. This is a class of Cu-containing, age-hardenable Al alloys that gain their mechanical strength through numerous metastable precipitates formed during heat treatment. It is the morphology and statistics of these precipitates, including aspect ratios, number densities, volume fractions, and more, which to a large extent determine the alloy's macroscopic properties.

In the studied alloys, many different precipitates exist, some of which are not well defined crystallographically. These precipitates have various morphologies, ranging from long needles to thin plates, and coexist with constituent particles as well as with dispersoids. The resulting microstructure is complex both in terms of coexistence, and by precipitates deviating from commonly defined phases. This makes complete characterization a demanding task, for which techniques are required to enable statistical treatment of precipitate distributions in terms of their atomic structure. Throughout this thesis, SPED is applied to heat-treated Al-Cu-Li and Al-Mg-Cu-Ag alloys, shedding light on the distribution of phases present and the complex interplay between these microstructural features.

The employed technique yielded high quality data sets, which through subsequent data processing enabled a detailed phase mapping of these multi-component Al alloys. Among the main results presented, are virtual dark field images highlighting all separate orientations of individual main strengthening precipitates in several low-order Al zone-axes. In many aspects, the obtained images are of higher quality as compared to corresponding conventional TEM imaging techniques. The virtual images exhibit a sharper, more consistent contrast, as well as a higher signal-to-noise ratio.

In addition, high spatial resolution orientational mappings of Al-Cu-(Mn,Fe) dispersoids have been obtained through diffraction pattern indexing. The obtained mappings achieve high reliability indices, and experimentally confirm the 10-fold rotation-twinned substructure of these particles. Furthermore, decomposition algorithms acting on the obtained data sets, yielded a semi-automatic method identifying eight different matrix-precipitate orientations of S-phases, as well as other valuable component patterns. In total, this provided a detailed phase mapping of the $[001]_{\mathrm{Al}}$ zone-axis in the Al-Mg-Cu-Ag alloy.

The contained work in this thesis validates SPED as a powerful analytical technique, enabling extraction of valuable information based on an accurate crystallographic fingerprint of the studied specimens. The technique is an important step in the direction of modern TEM methodologies, with increased focus on large data acquisition and analysis.

Samandrag

Denne mastergradsavhandlinga har anvendt teknikken skannande presesjonselektrondiffraksjon (SPED) innan feltet transmisjonselektronmikroskopi (TEM), i studiet av to ulike 2xxx-serie aluminiumslegeringar med høg elementtilsetting. Dette er ein klasse Cu-heldande aluminiumslegeringar som får deira mekaniske styrke gjennom talrike, metastabile presipitat som dannast under utherding. Det er morfologi og statistikk av desse presipitata, herunder dimensjonsforhold, taltettheit, volumfraksjonar, m.m., som i stor grad determinerer materialet sine makroskopiske eigenskapar.

I dei studerte legeringane dannar det seg fleire ulike presipitat. Nåkre av desse er ikkje klårt definerte krystallografisk. Presipitata har forskjellige morfologiar, og varierer frå lange nåler til tynne plater. Desse sameksisterer med andre intrametalliske fasar, herunder dispersoidar og inklusjonspartiklar. Dette gjev ein kompleks mikrostruktur, både som følge av sameksistens, og av enkelte fasar sitt avvik frå veldefinerte strukturar. Dette gjer fullstendig mikrostrukturkarakterisering utfordrande, og krev teknikkar kapable til å gjere statistisk behandling av presipitatfordelingar basert på den underliggande atomstrukturen. Gjennom avhandlinga er SPED anvendt på utherda Al-Cu-Li- og Al-Mg-Cu-Ag-legeringar, for å belyse den individuelle fordelinga av eksisterande fasar og samhandlinga mellom desse.

Den anvendte teknikken gav datasett av høg kvalitet, som saman med vidare databehandling gjorde det mogleg å gjere detaljert fasekartlegging av desse komplekse fleirkomponentlegeringane. Blant dei viktigaste resultata er framstillinga av virtuelle mørkefeltsbilete, som viser alle orienteringar av dei individuelle hovudpresipitata frå fleire forskjellige lågordens soneaksar. I mange aspekt er teknikken sine oppnådde resultat av høgare kvalitet enn for tilsvarande konvensjonelle TEM-teknikkar. Blant anna viser framstilte virtuelle bilete ein skarpare, meir konsistent kontrast, samt eit høgare signal-til-støy forhold.

I tillegg er det vist orienteringskart med høg romleg oppløysing av Al-Cu-(Mn,Fe)-dispersoidar, som er framstilt ved bruk av diffraksjonsmønsterindeksering. Dei framstilte karta syner gode pålitelegheitsindeksar, og bekreftar eksperimentelt den 10-foldige rotasjonstvillingstrukturen til desse partiklane. Vidare, ved å bruke dekomponeringsalgoritmar på innsamla datasett, vart det mogleg å semi-automatisk identifisere åtte matrise-presipitat-orienteringar av S-fasar, saman med andre verdifulle komponentbilete. Saman gav dette ei detaljert fasekartlegging av $[001]_{Al}$ soneaksen i Al-Mg-Cu-Ag-legeringa.

Det samla arbeidet i avhandlinga validerar SPED som ein allsidig analytisk teknikk, som tillèt ekstraksjon av verdifull informasjon basert på eit detaljert kystallografisk fingeravtrykk av det studerte materialet. Teknikken er eit viktig steg i retninga for moderne TEM-metodar, gjennom eit auka fokus på innsamling av større datasett og vidare analyse.

Preface

This master's thesis was written during the spring semester of 2016 as the fulfillment of my master's degree in applied physics at the Norwegian University of Science and Technology, NTNU. The experimental work was carried out at the Department of Physics, and the thesis was written at the division of condensed matter physics with professor Randi Holmestad as main supervisor.

The thesis is to some extent built on previously obtained results, as presented in the author's project work titled 'Precipitation of Several Coexisting Strengthening Phases in Aluminium Alloys', written during the autumn of 2015. Some of the contents in this project work are re-given here, in order to better present the full scope of scientific work performed during the final year of my MSc studies in applied physics and mathematics.

The thesis serves a dual purpose; studying the multiphase nature of 2xxx series Al alloys, as well as providing an introduction to the SPED technique. It is intended for readers who are interested with one or both of these topics.

I would like to thank my two indispensable supervisors professor Randi Holmestad and postdoc Sigurd Wenner for all their valuable help and enlightening discussions. I would also like to thank senior engineers Ragnhild Sæterli and Bjørn Gunnar Soleim for dedicating much of their time towards ensuring the TEM stays operational, as well as teaching me how to use the different techniques of TEM. Furthermore, I am very grateful for the helping efforts of the TEM group as a whole, being a most professional and enjoyable scientific environment to be a part of.

Trondheim, June, 2016

Jonas Kristoffer Sunde

List of Abbreviations

AA Artificial Ageing

BSS Blind Source Separation

CL Al-Cu-Li alloy

CL/CA Condenser Lens/Condenser Aperture

(C)TEM (Conventional) Transmission Electron Microscope/y

DP Diffraction Pattern

FEG Field Emission Gun

GP-zone Guinier-Preston zone

HRTEM High-Resolution Transmission Electron Microscopy

HT High Tension

MCA Al-Mg-Cu-Ag alloy

MFP Mean Free Path

NBD Nanobeam Diffraction

OA Over-Aged

OL/OA Objective Lens/Objective Aperture

RT Room Temperature

SAED Selected Area Electron Diffraction

SHT Solution Heat Treatment

(S)PED (Scanning) Precession Electron Diffraction

SSSS Super-Saturated Solid Solution

(S)TEM (Scanning) Transmission Electron Microscopy

VA Virtual Aperture

(V)BF (Virtual) Bright-Field

(V)DF (Virtual) Dark-Field

ZA Zone-Axis

Nominal Alloy Compositions

Table 1: Nominal elemental compositions of the two alloys Al-Mg-Cu-Ag (MCA) and Al-Cu-Li (CL). They are given as atomic percentages, at.%, and weight percentages, wt.%.

MCA	Elements							
at.%	Al	Mg	Cu	Ag	Fe	Mn	Other	Total solute
	97.05	1.137	1.305	0.128	0.099	0.277	<0.01	2.95
wt.%	Al	Mg	Cu	Ag	Fe	Mn	Other	Total solute
	94.75	1.000	3.000	0.500	0.200	0.550	<0.01	5.25
CL	Elements							
at.%	Al	Cu	Li	Si	Fe	Mn	Other	Total solute
	92.69	1.246	5.704	0.0	0.095	0.264	<0.01	7.31
wt.%	Al	Cu	Li	Si	Fe	Mn	Other	Total solute
	94.75	3.000	1.500	0.0	0.200	0.550	<0.01	5.25

Contents

Chapter 1

Introduction

Throughout the history of humankind, the mastering and development of novel materials have had a huge impact both culturally and technologically. This is most evident from the names given to large eras of history such as the Bronze ages, Iron ages and so forth. Our modern society is no exception, which is reflected in our extensive utilization of metals and semiconductors. These materials form the cornerstone of our technological progress and surrounds our everyday lives.

It is the metals that are most abundant. They are found in vast amounts of applications, ranging from nuts and bolts to automobile chassis and space-crafts. It is a billion dollar business ever-expanding as a result of increased demands with regards to high strength, corrosion resistance, increased functionality and lighter weight. With the additional important requirement of being environmentally beneficial, aluminium (Al) has emerged as one of the metals of the future.

This master's thesis builds further upon materials previously studied in the Research Council of Norway funded FRINATEK project No. 221714; 'Fundamental Investigations of Precipitation in the Solid State with focus on Al-based Alloys', which has been active since year 2013. The project studies different Al alloys from the main series, having various compositions, and usually high in solute contents. These alloys are not fit for industrial applications, but rather suited for studying precipitate phases, which form during heat treatment. The project's purpose is to describe the characteristics of precipitate evolution during artificial ageing (AA), and the interplay of the different phases involved.

The idea of using high solute additions is to provoke more pronounced behaviour in the precipitation sequences, which might lead to an increased understanding of the interplay of common alloying elements. This could further provide important insights, and highlight new aspects in existing industrial alloy compositions.

The most common Al alloy systems used in the industry are Al-Cu (2xxx), Al-Mg-Si (6xxx) and Al-Mg-Zn (7xxx), with other elements added in smaller amounts to enhance precipitation, or otherwise improve the mechanical properties. Being able to understand the influence of varying compositions and material treatments down to the nm- and atomic-level, is of fundamental importance to the future development of novel materials.

This master's thesis emphasize on this by trying to achieve increased and improved information extraction, using large data acquisition and subsequent data processing. This will be pursued in applying the technique of scanning precession electron diffraction (SPED). The focus will be with 2xxx series Al alloys, i.e. Cu-containing.

Two different FRINATEK 2xxx series Al alloys are studied:

- **MCA**: Al-Mg-Cu-Ag
- **CL**: Al–Cu–Li

The nominal elemental compositions of the two alloys are given in table 1, shown in the opening pages of this thesis. Al-Mg-Cu-Ag alloys are known to predominantly form hexagonal, plate-shaped Ω-precipitates during age hardening, forming on $\{111\}_{\mathrm{Al}}$-planes [1]. In addition, they produce large lath-shaped S-precipitates forming on $\{001\}_{\mathrm{Al}}$-planes [2]. Al-Cu-Li alloys are known to mainly produce a mix of hexagonal, plate-shaped T1- and octagonal (sometimes rectangular), plate-shaped θ'-precipitates, forming on $\{111\}_{\mathrm{Al}}$- and $\{001\}_{\mathrm{Al}}$-planes respectively [3], [4]. Furthermore, these precipitates coexist with preceding phases in the precipitation sequences, as well as with constituent particles and dispersoids.

Among the main interests with microstructure analysis of Al alloys, is the calculation of precipitate statistics; including aspect ratios, volume fractions (%) and number densities (#/nm^3) at different alloy conditions. Especially for alloys exhibiting several different types of main strengthening phases, this requires thorough and repeated use of different imaging techniques in several low-order zone-axis (ZA) oriented grains in the specimen. The morphology and coexistence of the different precipitates, can render high quality imaging used for statistics, more difficult to perform. An important factor such as the calculation of volume fractions, requires clear and sharp images of the relevant precipitates.

In the studied Al alloys, the microstructure is complex as a result of the coexistence of several different phases, whose dimensions have grown very large due to the high solute content. The lath- and plate-shaped morphologies of the different precipitates have grown to form a maze of closely spaced, and sometimes overlapping structures. Many of the conventional imaging techniques in transmission electron microscopy (TEM) fail to capture the essence of such multiphase structures. For instance, it is challenging to obtain images from individual phases of sufficient quality to fully capture the precipitate boundaries, and whether or not the phases are overlapping.

Throughout this thesis, SPED is applied to alloy CL and MCA in the over-aged (OA) condition, attempting to establish an improved method for studying multiphase Al alloys. Through subsequent data processing, this method has been reported to enable extraction of valuable crystallographic information and orientational relationships in complex multiphase materials [5].

The main thesis objectives are:

1. Acquisition of high quality SPED data sets from several low-order Al ZAs in both alloys

2. Formation of virtual images, highlighting individual precipitate distributions within the multi-component matrix, whose separate diffraction patterns (DPs) in the precession electron diffraction (PED) pattern stack are identified by comparison to DP simulations

3. To obtain images through several conventional imaging techniques; including High-Resolution TEM (HRTEM), Dark-Field- and Bright-Field TEM (DF- and BFTEM), and High-Angle Annular Dark-Field- (HAADF) and BF-STEM, and comparing these to the obtained virtual images

4. Extract additional information from the SPED data sets through 'machine learning'

The work contained in this thesis contributes to establish SPED's foothold at the TEM Gemini centre, NTNU. The technique follows the general trend of modern TEM methodologies, by having increased focus on obtaining large, multidimensional data sets, and further apply data processing in order to extract valuable information. Furthermore, the technique is applied within a core competence area of the group, i.e. with Al alloys, which sets the bar high with regards to what extracted data is deemed valuable.

Being among the first extended works applying this technique in this research environment, the thesis will have a two-fold focus throughout; applying the technique of SPED combined with subsequent data processing for extracting valuable information in multiphase Al alloys, as well as providing a future reference for SPED work at the TEM Gemini centre.

The rest of this thesis is organized as follows: chapter 2 gives a brief introduction to the theory and background behind several topics of importance for understanding the motivation behind the thesis, the experimental methods employed, and most importantly, for understanding the results obtained. Chapter 3 describes the experimental procedures used leading to the obtained results presented in chapter 4. Consequently, in chapter 5 the results are discussed in relation to presented theory and previously obtained results. Finally, chapter 6 draws concluding remarks, highlighting the findings of the report, before chapter 7 suggests what further work should be done on the topic of the thesis. Additional results are presented in the appendices A and B.

Chapter 2

Theory and Background

This chapter provides the information necessary in order to understand the applied experimental methods, as well as the obtained results of this thesis.

The presentation is coarsely divided in three; motivating the use of aluminium, explaining the microstructural origin of aluminium's interesting properties, and lastly, the scientific methods by which one studies this material.

2.1 Aluminium

Aluminium (Al) is a silvery, soft, paramagnetic and ductile metal. It makes up about 8.3% of the earth's crust by weight, which makes it the most abundant metal on earth. However, it is extremely rare in its pure state, owing to its very high chemical reactivity. In nature it is commonly found as aluminium oxide, Al_2O_3, constituting part of over 270 different minerals. Aluminium is a very light metal with a density of 2700 kg/m^3, and it exhibits great corrosion resistance through the effect of passivation. Its electrical and thermal conductivities are only surpassed by those of gold (Au), silver (Ag) and copper (Cu) among the metals, and out of these, aluminium is by far the lightest. A brief summary of the properties of aluminium is listed in table 2.1.

By forming Al alloys, which significantly improve upon pure aluminium's adverse effects, this metal has emerged as a highly attractive and versatile material. It is increasingly becoming the metal of choice in future applications, for reasons to be elaborated in the following. The major areas of application include transportation, building and construction, containers and packaging, electrical conductors as well as machinery and equipment [6], [7].

2.1.1 The brief history and development of aluminium

Aluminium was first discovered as a constituent of the red, clay-like ore, bauxite, in 1821 in Les Beaux, France. However, it had to wait until the late 1820s before it was first developed in its pure form, a feat usually credited to the german chemist Friedrich Wöhler. The production of pure aluminium remained exceedingly difficult to perform until the late

Table 2.1: Physical properties of the element aluminium (Al) [6].

Properties	Value
Atomic number (Z)	13
Electronic configuration	$[Ne]s^2p^1$
Density	2700 kg/m^3
Crystallographic structure	face-centered cubic (fcc)
Lattice parameter	4.04 Å
Electrical conductivity	35.0 MS/m (at 20 °C)
Thermal conductivity	237 W/(m· K)
Young's modulus	70 GPa
Shear modulus	26 GPa
Bulk modulus	76 GPa
Melting point	660.32 °C
Boiling point	2470 °C
Molar heat capacity	24.20 J/(mol·K)

1880s, and throughout this period it was even considered more valuable than gold [8].

It was first after the independent and parallel development of the Hall-Héroult electrolytic process due to Charles Martin Hall and Paul Héroult, that large-scale production of aluminium was made feasible [9]. The ore of bauxite is most commonly found within a belt around the equator, where it is dug out of mines a few meters below the ground. The bauxite containing clay is then transported to large facilities where it is first washed, before the remaining bauxite is crushed. After refinement through the Bayer-process, the intermediate product is the white powder alumina, or aluminium-oxide, Al_2O_3. The alumina is subsequently transported and used in large-scale smelters, where aluminium is produced through the Hall-Héroult electrolytic process.

In this process, huge currents ranging from 150-450 kA are driven through a positively charged carbon anode, a narrow layer of cryolite-alumina mixed bath and a negatively charged carbon cathode. Carbon-dioxide, CO_2, among many other gases is formed at the anode, and a liquid aluminium layer develops below the cryolite-alumina mixture near the cathode. The liquid metal is then tapped directly from the smelters and driven to a casting house. Here, different alloying elements are added for ensuring the right material properties. After this stage the products are usually ingots, bolts and sheets. The final re-shaping of the products usually happens at the customers through extrusion or rolling [10].

2.1.2 Properties and alloys

The main interest in using aluminium is not usually with its pure form state, which is relatively weak. High purity Al exhibits an annealed yield strength of only 7-11 MPa, and a tensile strength of 47 MPa. For comparison, common structural steels, which are among

the main competitor materials, exhibit typical yield strengths ranging from 200-400 MPa, and tensile strengths in the range of 400-550 MPa. However, by adding small amounts of other elements such as Silicon (Si), Magnesium (Mg), Zinc (Zn) and/or Copper (Cu), thus forming an alloy, Al's strength and properties can be greatly improved. The total addition varies, but is typically only a few at.%.

The strongest of Al alloys can be made comparable in strength to those of medium strength structural steels. As an example, certain high strength 7xxx series Al alloys have displayed yield strengths reaching 700 MPa [11]. Important to bear in mind, is that whereas steel has a typical density of 8000 kg/m^3, Al alloys have only about 1/3 of this value at 2700 kg/m^3. They are also more malleable than most steels, thus being the metal of choice in more complicated structures. Furthermore, the composition and material treatments can be tailored to suit a vast amount of areas of application.

Aluminium alloys are divided into two main groups; foundry alloys and wrought alloys. The categories reflect the two main methods of fabrication. Foundry alloys are fabricated by casting without applying any additional deformation during production. Wrought alloys however, are forged, extruded or rolled after the casting process. The alloys are further characterized by the labeling yxxx for wrought alloys and yxx.x. for casting alloys. For wrought alloys, the y denotes the main group of alloying elements, and the trailing x'es denote modification and amount of alloying elements. The classification follows the 'International Aluminium Alloy Designation System' [12].

The convention is similar for casting alloys, but here the last x denotes the product form. An added classification factor defines the alloys as heat treatable or non-heat treatable (synonymous to age hardenable). Heat treatable means that the atomic arrangement can be altered when the alloy is exposed to elevated temperatures for a certain amount of time. The different systems are summarized in table 2.2.

Importantly, it should also be noted that there are several downsides to using Al alloys. Among their main disadvantages they exhibit low endurance limits, lower hardness than achievable with structural steel, as well as a very low melting point of 660 °C. Requirements for very high strength in for instance certain car components located near the engine room make Al alloys second to steel.

2.1.3 Areas of application

Despite the fact that most Al alloys cannot compete with the high strength of the strongest of structural steels, due to their very light weight, they reign supreme in terms of a higher strength-to-weight ratio. This makes it the metal of choice in applications where a lighter weight is greatly beneficial, such as in the transport industry or in buildings and constructions. The light weight allows for great costs savings due to reduced fuel consumption and easier workability.

Furthermore, its high conductivity-to-weight ratio makes it outperform that of copper (Cu). It therefore finds important application in high-voltage cables, connectors and distribution bars. And even though high purity 1xxx Al alloys does not outperform the

Table 2.2: Classification of the different Al alloy series as determined by the 'International Aluminium Alloy Designation System', with additional classification of age-hardenability.

Wrought Alloys		
Series	Elements	Age hardenable
1xxx	> 99% Al	non-age hardenable
2xxx	Al-Cu and Al-Cu-Li	age hardenable
3xxx	Al-Mn	non-age hardenable
4xxx	Al-Si and Al-Mg-Si	age hardenable
5xxx	Al-Mg	non-age hardenable
6xxx	Al-Mg-Si	age hardenable
7xxx	Al-Mg-Zn	age hardenable
8xxx	Other elements	age hardenable

Casting Alloys		
Series	Elements	Age hardenable
1xx.x.	> 99% Al	non-age hardenable
2xx.x.	Al-Cu	age hardenable
3xx.x.	Al-Si-Cu and/or Al-Mg-Si	some are age hardenable
4xx.x.	Al-Si	non-age hardenable
5xx.x.	Al-Mg	non-age hardenable
6xx.x.	Currently not in use	-
7xx.x.	Al-Mg-Zn	age hardenable
8xx.x.	Al-Sn	age hardenable
9xx.x.	Other elements	-

conductivity of copper, strongly shifting metal prices makes Al important also within smaller scale electrical wiring. Due to its lightness, impermeability and corrosion resistance, it has a huge area of application within foils and packaging, where it is an undisputed champion [13].

Although Al production is a very energy intensive process, the metal allows for 'infinite' recyclability, thus leading to great cost savings in the long run. It is estimated that approximately 70-75% of all aluminium ever produced is still in use today. In recycling aluminium, only 5% of the initial production energy is needed [10]. A summary of common areas of application for the different Al alloy series is shown in table 2.3.

Table 2.3: Common areas of application for the different main Al alloy series [11].

Series	Applications
1xxx	Piping, chemical tanks and bus bars
2xxx	Auto-mobile chassis and space-crafts
3xxx	Pots, pans and heat exchangers
4xxx	Filler material (fusion welding and brazing)
5xxx	Ships, bridges and buildings
6xxx	Automotive body-panels, windows, ladders, offshore structures
7xxx	Aircrafts, space-crafts and competitive sporting equipment
8xxx	e.g. Al-Sn: bearings in cars and trucks, Al-Fe-Si: foils and closures

2.2 Crystallography

A *crystal* is a perfectly ordered, periodic structure in space. It is a geometric concept, and therefore the repeated unit constituting the crystal could in principle be anything. However, the concept is most commonly used when speaking of physical materials existing in nature. Here, on nature's smallest of scales, the basic building blocks are atoms, molecules and ions.

By first considering a crystal as an ordered array of points, without regards to what the structure associated with these points might be, the most important concept in describing crystalline materials is that of a *Bravais lattice*. Simply put, if every point of a lattice is equivalent, in the sense that every point's geometric surroundings are identical in all respects, the lattice is termed a Bravais lattice. A Bravais lattice must exhibit translational symmetry. Therefore, with the origin attached to one lattice point, every point of a Bravais lattice can be defined through the set of points

$$\mathbf{R}_{\text{hkl}} = h\mathbf{a}_1 + k\mathbf{a}_2 + l\mathbf{a}_3, \tag{2.1}$$

where h, k and l are integers. The vectors $\mathbf{a}_1$, $\mathbf{a}_2$ and $\mathbf{a}_3$ are termed *primitive* vectors, and their combination $\mathbf{R}_{\text{hkl}}$ is the lattice vector connecting all the points of the Bravais lattice.

Now, we attach to every lattice point a *unit cell*. The unit cell is the periodically repeated structure of the crystal. Its general shape is a parallelepiped spanned by the primary lattice vectors $\mathbf{a}_\text{i}$. Translating this parallelepiped through all the lattice vectors, defined through equation 2.1, spans the total volume of the crystal. If it does so without any overlap, it is termed a *primitive* unit cell.

The structure linked to the unit cell is not limited to single atoms. In general, the unit cell can have a *basis* consisting of several atoms, molecules, ions, whole protein structures, and so forth. This requires an additional basis coordinate vector $\mathbf{r}_\text{j} = \langle u_\text{j}\mathbf{a}_1, v_\text{j}\mathbf{a}_2, w_\text{j}\mathbf{a}_3 \rangle$, which locates the jth basis constituent relative to the lattice point, i.e. the origin of the unit cell, $\mathbf{R}_{\text{hkl}}$. u_j, v_j and w_j are fractions < 1 of the primitive lattice vectors, $\mathbf{a}_\text{i}$. A crystal is defined by the combination of a lattice and basis, see figure 2.2 (a). This is mathemat-

ically expressed as a convolution of the two. In total, every constituent of the crystalline material is reached through the vector $\mathbf{r} = \mathbf{R}_{hkl} + \mathbf{r}_j$.

There are in total seven different crystal systems, each defined by the lengths of primary lattice vectors $\mathbf{a}_i$, and the angles between them (α, β, γ). In order of increasing symmetry operations they are; triclinic, monoclinic, orthorhombic, tetragonal, trigonal (rhombohedral), hexagonal and cubic. In some of these systems it is possible to find more than one equivalent lattice point. This further defines simple/primitive (P), end/side/base-centered (C), body-centered (I) and face-centered (F) lattices. In total this defines 14 Bravais lattices as shown in figure 2.1.

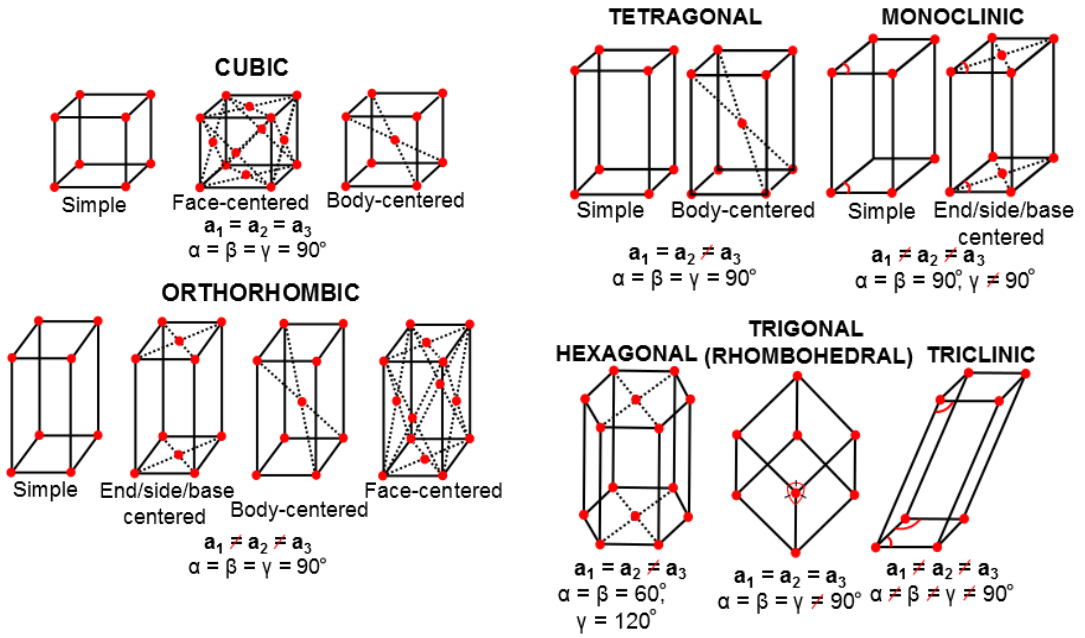

Figure 2.1: A schematic showing the 14 different Bravais Lattices. Notations are explained in the text. Figure inspired by [14] p.16-18.

Combining this classification with possible symmetry operations such as rotations, mirror planes (m) and a combination of these, gives a unit cell's *point group*. Allowed rotations compatible with translational symmetry are given by angles $\phi = 2\pi/n$, where n is an integer in the set {1,2,3,4 and 6}. A combination of a rotation, n, with a subsequent mirror plane, known as rotation-inversion, is denoted $\bar{n}$. In all, this defines 32 different point groups. A final classification includes rotations and reflection in combination with translation, i.e. the operations of screw axes and glide planes. These further increase the classification to 230 different *space groups*.

For example, Al exhibits cubic symmetry and has the space group #225, denoted $Fm\bar{3}m$. This implies that the unit cell of Al is face-centered cubic (fcc), having two non-equivalent mirror planes and a three-fold rotation-inversion axis (along the cube diagonals). For a comprehensive and explicit derivation it is referred to any textbook on crystallography. For a shorter introduction it is referred to Ch. 1 of [15] or [16].

In addition to crystal structure space groups, another important topic for describing the crystalline structure of Al alloys, where precipitate structures are embedded in the matrix, are *orientational relationships*. This will also be of importance in the later topics of scattering and diffraction. First one must recall the notions of atomic planes and directions in the lattice.

Lattice directions are denoted [hkl], using three *Miller indices* h, k and l, whose direction is parallel to the vector $\mathbf{R}_{\text{hkl}}$ of equation 2.1. An atomic plane is denoted (hkl), where the indices are defined as the smallest integers without a common divisor, being the reciprocal of the intersection of a plane with the axes of the unit cell parallelepiped. Should the crossing be along negative axes, it is denoted by a bar over the corresponding Miller index. A set of equal planes is denoted {hkl}, and a set of equal directions is denoted ⟨hkl⟩.

For example, if the lattice plane should cross the $\mathbf{a}_1$ axis midway, this would correspond to a crossing at 1/2 $\mathbf{a}_1$, and thus the Miller index $h = 2$. The [100] direction in the cubic system is along the $\mathbf{a}_1$ edge, and [111] is along the diagonal of the cube. Examples of these definitions are shown in figure 2.2 (a).

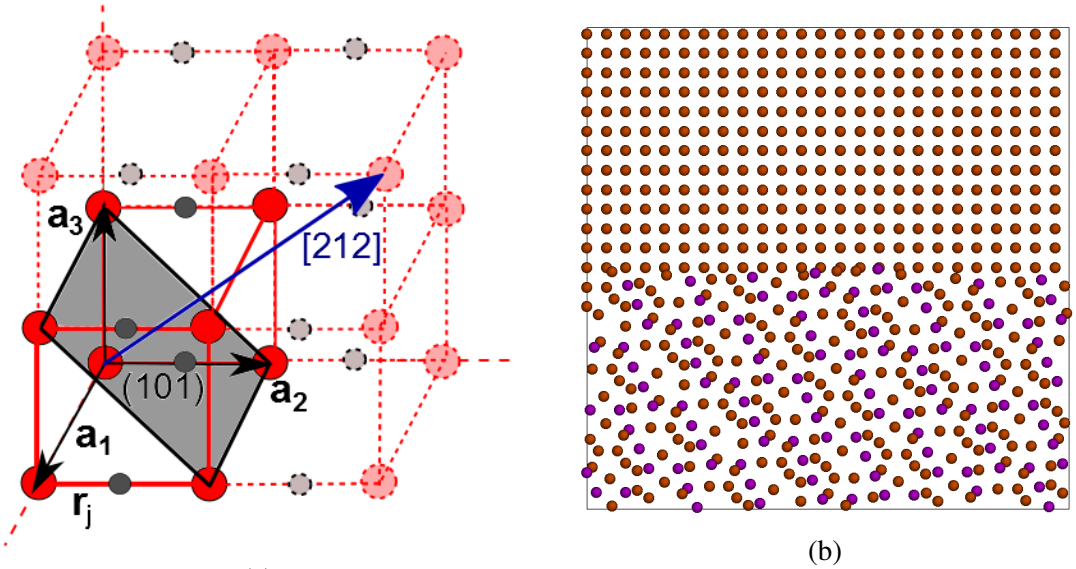

(a) (b)

Figure 2.2: (a) Example of direction- and plane indexation in a generic primitive (P) tetragonal crystal, $\mathbf{a}_2 = \mathbf{a}_3 < \mathbf{a}_1$. The crystal has a basis consisting of two atoms, drawn as red and grey spheres. (b) One of the possible orientational relationships between the Ω-precipitate and the surrounding Al matrix in the $[001]_{\text{Al}}$ ZA, as allowed by the orientational relationship of equation 2.2.

For a stack of different materials, or a multiphase material such as Al alloys, it is important to specify the orientational relationships between the different crystalline phases. In Al, this relation is between the embedded precipitate structures and the surrounding matrix. The degree of coherency to the surrounding matrix determines the strain associated with the mismatch. It also determines the possible growth directions of the precipitate, which further decides the morphology of the precipitate. An orientational relationship can for instance be specified as

$$(001)_{\Omega}||(111)_{\mathrm{Al}},\ \ \langle 010\rangle_{\Omega}||\langle 110\rangle_{\mathrm{Al}}\ \text{ or }\ \langle 310\rangle_{\Omega}||\langle 110\rangle_{\mathrm{Al}}\ [1]. \tag{2.2}$$

Here, Ω denotes an Al_2Cu-precipitate commonly found in 2xxx series Al alloys. The relation indicates that the $\{001\}_{\Omega}$-plane runs in parallel to the $\{111\}_{\mathrm{Al}}$-planes. Furthermore, it indicates two pairs of parallel directions in the precipitate relative to the Al matrix. In total, these relations fully specify the orientation of the Ω-precipitate relative to the surrounding Al matrix, see figure 2.2 (b). An image of an Ω-precipitate embedded in an Al matrix is shown in figure 2.3.

Calculating angles between matrix constituents characterized by indices [hkl] and [mno], is accomplished by the vector product formula, $\mathbf{u}\cdot\mathbf{v} = \mathrm{uv}\cos\theta$, as

$$\cos\theta = \frac{hn + kn + lo}{\sqrt{h^2k^2l^2}\sqrt{m^2n^2o^2}}. \tag{2.3}$$

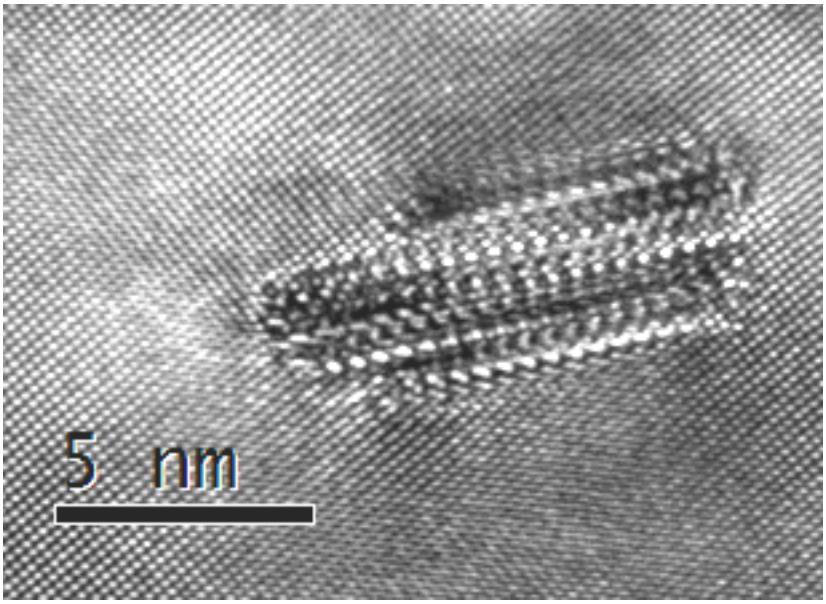

Figure 2.3: HRTEM image of an Ω-precipitate embedded in an Al matrix, as observed near the $[001]_{\mathrm{Al}}$ ZA in alloy MCA.

2.3 Precipitation Hardening

The properties of Al alloys are not solely determined by their atomic composition. In fact, the final properties of an alloy are crucially dependent on all preceding material treatments. These include, but are not limited to; casting parameters, homogenization cycle, annealing, extrusion- and ageing parameters. The graph in figure 2.4 shows an example Al alloy pre-treatment.

The homogenization cycle consists of pre-heating the Al alloy to high temperatures, typically 570-600 °C, after the casting process. The purpose is to even out the heterogeneous microstructure, which allows for improved workability. Pre-heating the alloy before extrusion/rolling is done to dissolve most of the precipitate phases that have formed in the preceding stages, thus softening the material. The ageing parameters can be separated into solution heat treatment (SHT), quench rates, natural ageing (NA) and artificial ageing (AA). The different treatments can also be divided into five major groups denoted by the letters F, O, H, W and T. The former three denote as-fabricated, annealed and cold-worked. The latter two denote denote solution treated and age hardened, which will henceforth be discussed under the term heat treatment [12].

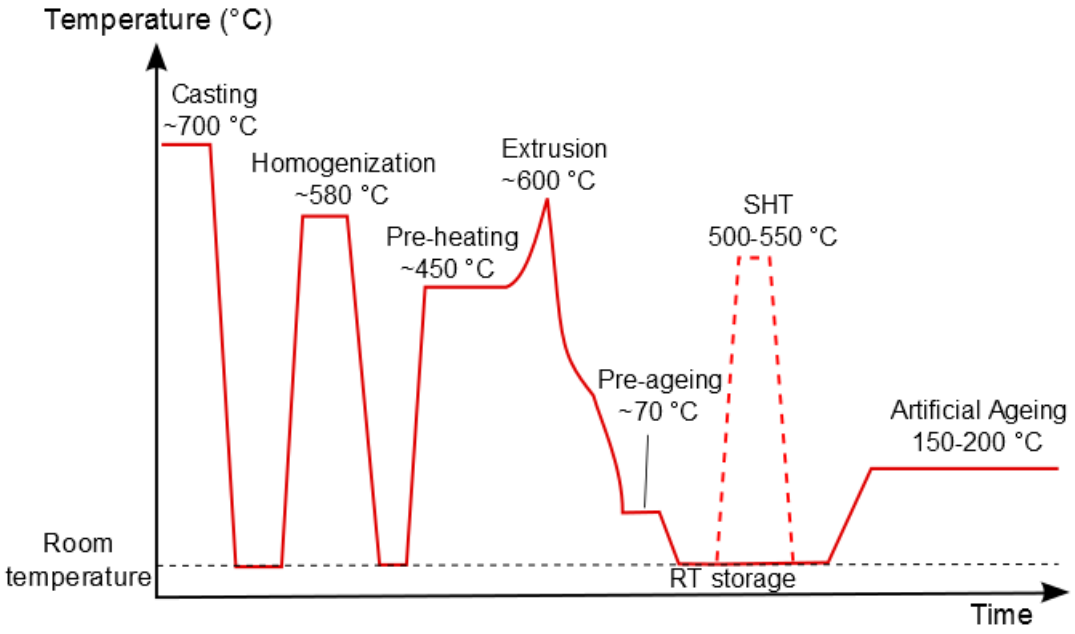

Figure 2.4: Example of a thermo-mechanical treatment of a typical Al alloy. For scientifically studied alloys it is usually added a SHT step after extrusion.

Al alloys can be tailored to a specific set of properties by fine tuning the different aforementioned material treatments. They all involve restructuring of the constituent atoms. The discovery that certain Al alloys can achieve increased hardness after heat treatment was published in 1911 by Alfred Wilm. His findings were linked to the development of a light-weight and strong alloy, *Duralumin*, which had additions of Cu, Mg and Mn [8]. Its underlying cause however, was not explained until the late 1930s, and was attributed to

nano-sized, metastable precipitates forming throughout the Al matrix. The precipitates, along with other defects in the Al matrix, prevent the generation and movement of *dislocations*, which leads to an increased material strength. The resistance against *slip*, i.e. the movement of dislocations, is the source of any alloy's strength [17]. The following sections elaborate on these topics.

2.3.1 Dislocations and strain

In reality, perfect crystals do not exist. Every real material with an underlying crystal lattice is prone to several different defects, which for metals account for many of their interesting properties. Every atom of a crystalline material is bound to the surrounding material by a certain energy W_b, which is on the order of a few eV. At a finite temperature, T, there is a finite probability, p, that this atom acquires sufficient energy to 'jump' from its initial position to a neighbouring site, given as

$$p = \exp\left(-W_\mathrm{b}/\mathrm{k_b}T\right),$$

where $\mathrm{k_b}$ denotes Boltzmann's constant. The site to which the atom jumps can be a vacant site, or an *interstitial* site. An interstitial site is a position in between those of the normally occupied lattice sites. The possible positions depend on the underlying lattice. Interstitial jumping creates two defects; a vacancy at the initial position and an interstitial atom at the new position. Defects consisting of only a single atom are called point defects. They can also occur in pairs which is termed *Frenckel defects*. Point defects may also be due to impurity atoms such as those introduced by alloying elements in the Al matrix. Small impurity atoms may go into interstitial positions. If they are similar in size to the surrounding matrix atoms they tend to go substitutional [14]. Figure 2.5 shows examples of different defects in a crystalline lattice.

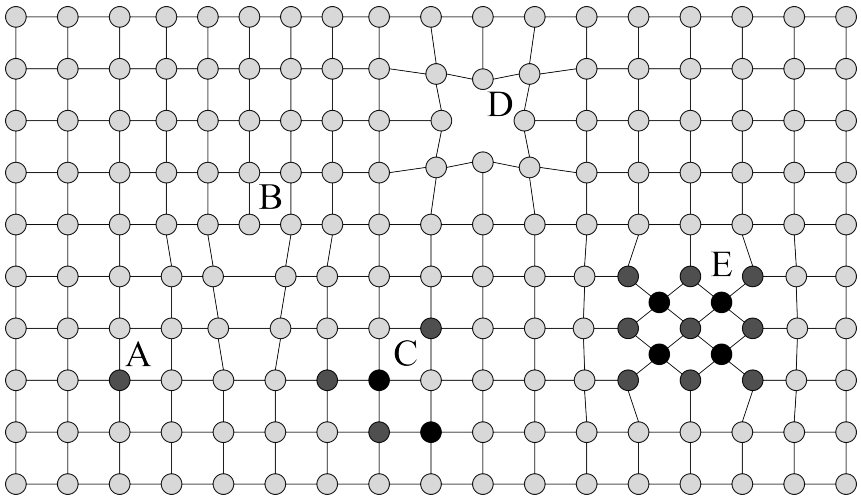

Figure 2.5: Lattice defects in a generic crystalline solid. A: Substitutional solute atom, B: Dislocation, C: Cluster of solute atoms, D: Vacancy, E: Precipitate phase [18].

Point defects can be termed one-dimensional. Extended regions of lattice defects, referred to as two-dimensional defects, are called *dislocations*. Dislocations are of great importance in physical metallurgy, as they to a large extent determine the mechanical strength and plasticity of materials. The main dislocation types are *edge*- and *screw* dislocations.

An edge dislocation may be visualized as an added (or lacking) half-plane of atoms within a lattice. It is also termed a *line defect*, because the locus of defective points produced due to the defect lie along a line, **l**. The line runs along the bottom of the extra half-plane. In proximity of the the dislocation the neighbouring atoms are distorted and strained, giving rise to deviations from the ideal lattice configuration, see figures 2.5 (B-marking) and 2.6.

Due to this strain, a dislocation energy may be associated with the defect. Similarly to the interaction of electrical charges, these elastic distortions might attract or repel each other. Furthermore, they might also neutralize or annihilate each other. Here, the notions of equal or opposite are determined through the concept of a *Burger's vector*, **b**. By forming a closed circuit in, say, the anti-clockwise direction around the dislocation, running from unit cell to unit cell, the Burger's vector forms the mismatch between the number of unit cells passed in moving from the right to left, up and down, see figure 2.6. Equal dislocations means equal **b**-vectors. Correspondingly, opposite means opposite (anti-parallel) **b**-vectors.

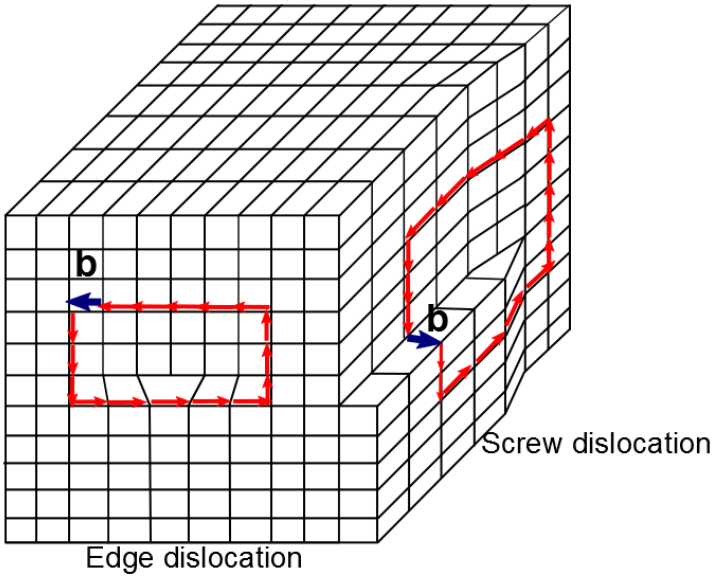

Figure 2.6: The Burger's vector construction for two fundamental two-dimensional defects, namely edge- and screw dislocations.

The second type of fundamental dislocations is the screw dislocation. If a shear stress is applied to the end of a metal bar, then the top end of the bar will be displaced with respect to the bottom edge by a slip vector **s** over a glide plane. The screw dislocation line is located at the leading edge of the shift of the face and runs parallel to the slip vector. A

plane perpendicular to this dislocation line will be connected together to form a helix as a result of the dislocation displacement, like a screw. The Burger's vector is constructed in the same manner as for the edge dislocation. For pure screw dislocations it runs parallel to the dislocation line.

At angles other than perpendicular and parallel of the **b**-vector to the dislocation line, one has a mixed dislocation. Dislocations belong to the whole piece of a given crystal material. It cannot terminate within the crystal, and the Burger's vector is constant along a dislocation line. When dislocations meet and combine, the resulting dislocation will be the sum of the two Burger's vectors. If they are initially opposite, they will meet and annihilate. Plastic deformation of a material comes about by slip along planes in the material. Such slip may be described as motions of dislocations until they reach the surface of the material [14], [17].

As previously mentioned, the presence of different defects hinder the movement of dislocations, and this is due to the associated strain field of the defects. The strain field acts as a restraining force on moving dislocations. For Al alloys after thermo-mechanical treatment, the main resistance against dislocation movement is provided by:

- Grain structure
- Dislocations
- Atoms in solid solution
- Solute clusters/Guinier Preston (GP) zones
- Precipitates

Depending on the size, density and strength of these structures, the moving dislocation will either loop around or shear them. For strong strain fields the dislocation will usually loop around, and for weaker fields it will usually shear the precipitate. It is therefore understandable how the control of the precipitate statistics provide control of important alloy properties such as hardness and ductility.

2.3.2 Secondary phases in Al alloys

Along the different material pre-treatment procedures of figure 2.4, the added energy enables the alloying elements to diffuse through the Al matrix, and eventually form different secondary phases embedded within it. The secondary phases in Al based alloys are generally subdivided into three classes: constituent particles, dispersoids and precipitates.

Constituent particles are phases that form by a liquid-solid eutectic reaction during solidification, e.g. after casting. These may proceed to transform during further high temperature exposure, e.g. homogenizing or solution heat treatments. In most applications, constituent phases are undesirable as they are generally detrimental to the material's macroscopic properties, and especially to damage tolerance. Some constituent particles (e.g. eutectic θ+S-phases) can also cause localized melting at temperatures that are lower than

in similar composition alloys which do not contain the constituent particles. This may limit high temperature thermo-mechanical treatments. Constituent particles are generally a different type of inter-metallic phase in the matrix, and are often referred to as 'coarse inter-metallics'. In general, the particles are coarse with sizes ranging from one to several tens of μm. Particle size decreases as solidification rate increases, as Fe and/or Si content decrease, and as the amount of deformation during mechanical and thermo-mechanical processing increases [19].

Two groups of phases may be distinguished according to their stabilities in industrial alloys: one is generally insoluble during heat treatment, and the other is generally soluble provided the amount of main alloying atoms is kept below solubility limits. The insoluble phases arise mostly from Fe and/or Si impurities, which, in commercial alloys for structural applications, are very often present because of the high cost of reducing total impurity levels to below the maximum solubility levels ($\approx$ 0.1 wt.%). These constituent particles are insoluble because of the low solubility of Fe in Al, and the low solubility of Si in Al alloyed with Mg. The soluble constituent phases can be dissolved during heat treatment, by virtue of the high solubility of Cu and Mg in Al [20].

The constituent phases, and especially the insoluble ones, are normally deleterious for the mechanical properties as they are the sources of crack initiation and corrosion, and enhanced crack growth, while they make no substantial contribution to the yield strength of the alloy.

Dispersoid particles usually form during homogenization, and are generally 'finer' than the constituent particles. In Al alloys used in structural applications, their main purpose is to control the grain structure during high temperature heat treatment and to provide resistance against re-crystallization. The main types are Zr, Mn, Cr and Sc containing phases.

With sizes in the range of 0.02–0.5 μm, they are much smaller than constituent particles [21]. Because of the low solubility of the main dispersoid forming elements Mn, Zr and Cr, dispersoids can not be dissolved to an appreciable extent by subsequent solid state thermal treatments.

Precipitates are fine phases or clusters that form during ageing. These are the main phases of interest in controlling Al alloy properties, and the focus will be with these in the following.

2.3.3 Heat treatment

The purpose of heat treating Al alloys is to alter the material's atomic structure along the different stages of production, and finally to achieve the desired material properties of the end-product. The alloy is kept at different temperatures at various times, from the time of casting until final area of application. The heat treatment procedure applied in scientific works studying precipitate evolution, is usually dived into three main parts; solution heat treatment (SHT), natural ageing (NA) or room temperature storage (RT-storage) and artificial ageing (AA). Different treatments are commonly abbreviated TX, where X is a number and T denotes the alloy being subjected to age hardening [12].

2.3.3.1 Solution heat treatment

Solution heat treatment consists of heating the alloy to a high temperature (>400 °C) for a time, t, usually >30 min. The temperature is chosen such that the solubility of solute elements is the highest without any liquid form transition. The effect is to dissolve all phases consisting of solute elements in the Al matrix, leading to a near homogeneous distribution. An additional effect is to introduce vacancies in the matrix. The density of vacancies, D_v, present in a metal increases exponentially, as expressed through the relation

$$D_{\mathrm{v}} = (\text{const.}) \cdot \exp\left[\frac{E_{\mathrm{v}}}{\mathrm{k_B}T}\right].$$

Here, E_{v} is the energy required to introduce a vacancy in the matrix and, T, is the absolute temperature measured in Kelvin. The diffusion of substitutional solute atoms is dependent on vacancies in the matrix. Vacancy diffusion is many orders of magnitude larger than the self-diffusion of solute atoms. This process is therefore crucial to form atomic clusters and subsequent growth of precipitates. After SHT the alloy is often quickly water quenched to RT, thus preserving the homogeneous atomic distribution.

2.3.3.2 Natural ageing

The state reached after SHT and subsequent quenching is termed a super-saturated solid solution (SSSS). Due to the quick temperature drop after SHT, the alloy has not had time to separate out substitutional atoms. Thus more alloying elements are dissolved in the matrix than normally allowed. This state is not stable, even at RT. The solute atoms diffuse through the matrix resulting in formation of different phases. This process is actually how the age hardening mechanism was first discovered. It is however, a very slow process as a consequence of the exponential temperature dependence.

2.3.3.3 Artificial ageing

During this stage of the heat treatment procedure, the Al alloy is kept at elevated temperatures typically ranging from 150-200 °C for a certain amount of time. The time of the process is chosen in order to achieve a specific set of precipitates forming in the matrix. The elevated temperature acts to lower the energy barrier for formation of initial atomic clusters. The time and temperature varies with alloy composition and desired properties. After treatment, the alloy is quickly quenched to RT in order to 'freeze' the atoms in place, and thus obtaining the sought alloy condition. Compared to SSSS, this is not a particularly unstable condition, and further NA proceeds very slowly [17].

2.3.4 Nucleation and precipitation sequences

Many materials, including Al alloys, are polycrystalline. They consist of many grains of individual crystallites. The grain boundaries (GBs), sometimes called the interphases, comprise complicated patterns of defects and dislocations, and provide a gradual link holding the crystal lattice together, see figure 2.7.

Phase transformations within the Al matrix are due to a rearrangement of the atomic structure. In addition, it may produce a compositional change and/or a strain formation. For Al alloys, the most important phase transformation is of type crystal 1 $\rightarrow$ crystal 2 with accompanying rearrangement, compositional change and strain formation.

By gradually heating the alloy from RT, the constituent atoms start to vibrate more rapidly. This causes the effective lattice parameter, a, to increase in size. At a certain temperature, T_{trans}, a phase transformation is initiated. The process is not spontaneous, but a gradual change due to an initial formation (*nucleation*) of small regions of a crystal 2 phase within the crystal 1 matrix, referred to as an *atomic cluster*. The barrier to be overcome is due to the positive free energy, σ_{S}, associated with the surface area of the nuclei. The initial nuclei are very small, some 10 Å, and presumably spherical in shape. Correspondingly, they have a very high surface-to-volume ratio. In addition to the formation of additional clusters, these grow in size, leading to formation of GP-zones. Proceeding, for some alloys these eventually grow and lead to a complete transformation of a crystal 1 into a crystal 2. Essentially, all phase transformations occur by a nucleation and growth of nuclei [17].

When the new phase nucleates, it usually forms at some discontinuity in the parent matrix, such as a GB or a dislocation. This is due to the threshold energy requirement, σ_{S}, of the nuclei. Material systems undergoing phase transformation attempt to reduce the σ_{S}-barrier by having nucleation occurring on a pre-existing surface. This 'wipes out' some of the preexisting surface in trade for a reduced energy cost. However, nucleation may also form within a uniform region of the parent matrix. One distinguishes these two types of nucleation as *homogeneous* and *heterogeneous*. Homogeneous nucleation denotes new phases forming uniformly throughout the bulk of the parent phase. Heterogeneous nucleation denotes phases forming preferentially at inhomogeneities in the parent phase.

In most Al alloys, the equilibrium phase does not form immediately upon ageing. It is preceded by several metastable phases in a *precipitation sequence*. The equilibrium precipitate is that of lowest free bulk energy, σ_{B}. They are however not the first phases to form due to their associated high interface energy, σ_{I}. Therefore, phases being more coherent with the Al matrix form first due to a lower σ_{I}-threshold. These phases necessarily have higher σ_{B}. They provide a smaller bulk energy gain as compared to the uniform distribution of solute elements, and form at relatively low temperatures. Further increasing the temperature and time, these more coherent phases will no longer provide the highest energy gain, and eventually the equilibrium phases will be the primary ones to form [17].

The different alloy systems have a large number of possible precipitate phases. The precipitate types that form, their physical dimensions and their distribution in the Al matrix, are crucially dependent on parameters such as alloy composition, age hardening, heating/cooling rates, deformations, storage time and more. By increasing the AA times, the relative fractions of the different types of precipitates change. Each of the precipitates have a preferred alloy composition and heat treatment time for maximizing its presence.

For the MCA alloy, the suggested precipitation sequence is [1], [2]

$$\text{SSSS} \rightarrow \text{Atomic Clusters} \rightarrow \text{GP-zones} \rightarrow \theta'', \text{S}'' \rightarrow \theta', \text{S}' \rightarrow \theta, \text{S} \rightarrow \Omega, \text{S}, \tag{2.4}$$

where the different θs, Ss and Ω denote different characteristic precipitates in the sequence. The Ω-precipitation sequence is not completely resolved, but it has been found that addition of the elements Ag and Mg could change the precipitation sequence from θ/S to Ω [22]. The CL alloy shows the sequence [3], [23]

$$\text{SSSS} \rightarrow \text{Atomic Clusters} \rightarrow \text{GP-zones} \rightarrow \theta'', \text{T1}' \rightarrow \theta', \text{T1} \rightarrow \theta, \text{T1}, \tag{2.5}$$

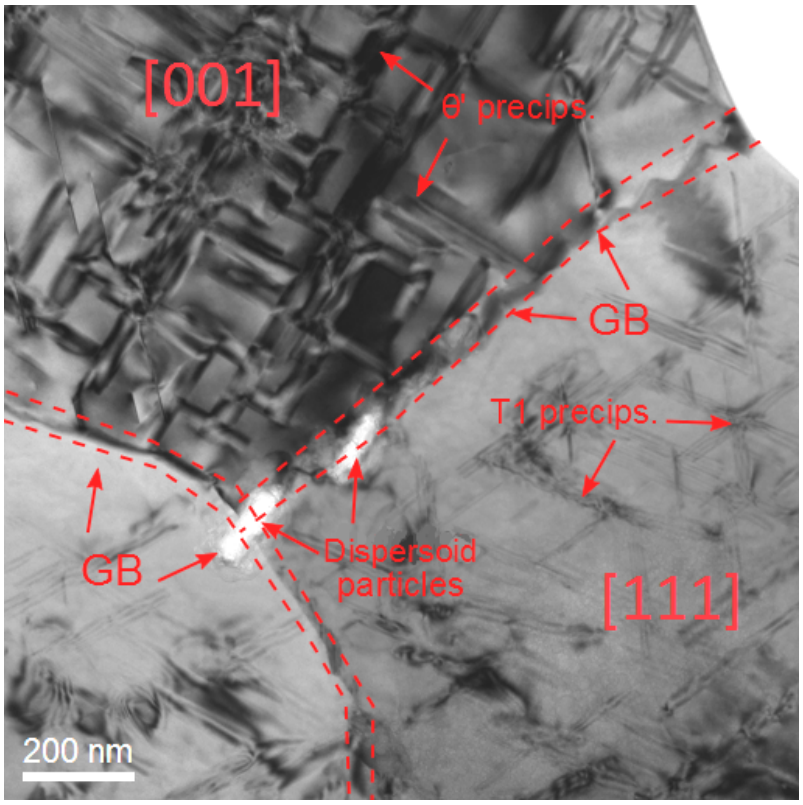

Figure 2.7: BFTEM image showing GBs between three individual Al grains. Upper left grain is oriented near the $[001]_{\text{Al}}$ ZA, and the lower right grain is oriented near the $[111]_{\text{Al}}$ ZA. Dispersoids forming on the GBs are highlighted, in addition to characteristic T1- and θ'-precipitates, as forming in the CL alloy.

where again the different θs and Ts, denote different characteristic precipitates in the sequence. The cited Dwyer-paper also shows that the thickness of T1-precipitate plates is nearly constant, measuring ≈ 1.39 nm. This will be of relevance later in this thesis. The atomic compositions and morphologies of the different precipitates in these Al alloys will be shown later in this thesis.

2.4 Physical Principles and Operation Modes of TEMs

The transmission electron microscope (TEM) operates through many of the same principles as the familiar optical microscope. There are however several important differences which make the TEM much more complex, and many times as powerful and versatile. Most notably, whereas the optical microscope uses visible light focused through curved glass lenses, the TEM uses electrons focused through a multitude of magnetic coil lenses, deflectors and apertures achieving the same goal; to provide a clear, magnified image of the specimen under study. Furthermore, as indicated by the term *transmission*, the final image as recorded on a fluorescent screen or a CCD camera, is a 2D projection formed by electrons having transmitted the sample.

Through the well-known wave-particle duality principle due to De Broglie, the electron exhibits wave properties similar to optical light [24]. The De Broglie wavelength, λ, for an electron with rest mass, m_0, and momentum, p, is given as

$$\lambda = \frac{\mathrm{h}}{p},$$

where h denotes Planck's constant. The interdependency of wavelength and momentum means that depending on the electron's speed its effective wavelength is altered. The obtained speed is adjustable by varying its energy. In the TEM, the electron achieves a high energy by acceleration through a high-voltage source, with a typical output of 60-500 kV.

At 100 kV, the electron reaches a speed of 55% of c, the speed of light in vacuum. Hence, the theory of electron scattering in the TEM therefore needs to take into account relativistic effects. Using the relativistic energy relation $E_\mathrm{k} = \sqrt{p^2c^2 + m_0^2c^4} - m_0c^2$, the wavelength can consequently be written as [25]

$$\lambda = \frac{\mathrm{h}}{\sqrt{2m_0eU(1 + eU/2m_0c^2)}}. \tag{2.6}$$

Here, eU denotes the energy obtained when the electron is accelerated through the column potential, U, having the elementary charge, e.

At 200 kV acceleration voltage, the effective electron wavelength is equal to 2.51 pm. This is a miniscule wavelength as compared to the far end of the visible light spectrum (violet $\approx$ 380 nm), thus allowing much smaller structures to be observed. However, unlike optical microscopy, where obtained resolutions approach that of applied wavelengths,

due to the poor performance of electron optical lenses, obtainable resolutions are much poorer than the pm-range. In many present day conventional TEMs (CTEMs), experimentally achievable resolutions are in the regime of 2 Å (< 1 Å combined with aberration corrections) [25]. A typical TEM column is displayed in figure 2.8.

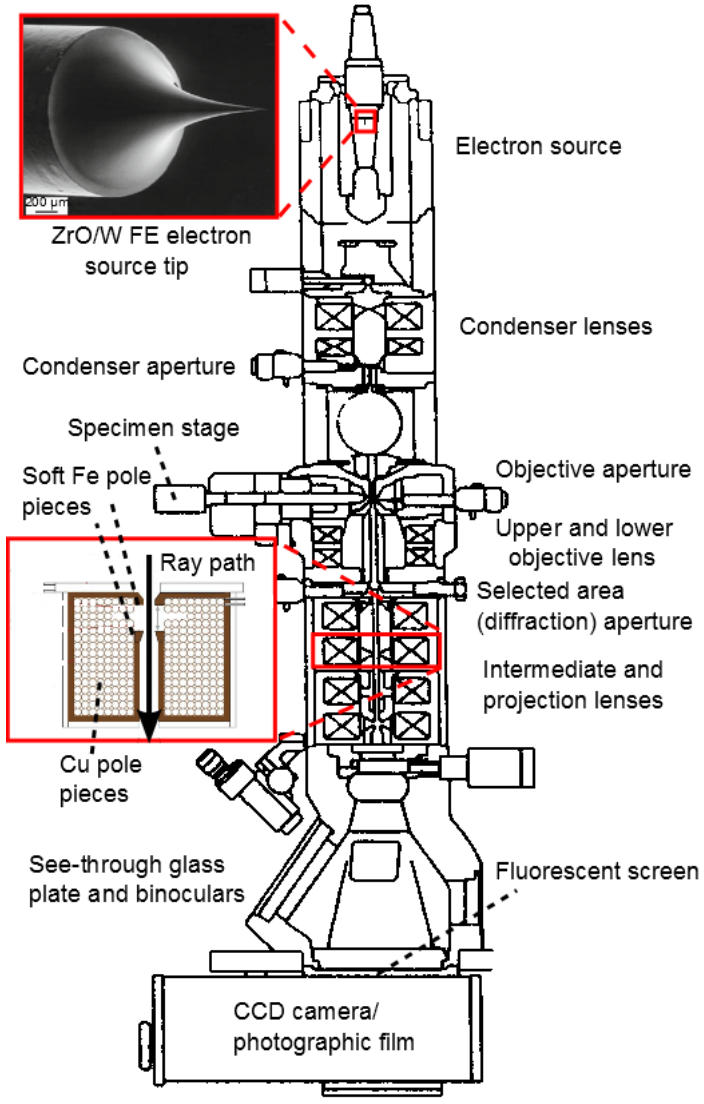

Figure 2.8: A typical TEM column with basic electron optical hardware setup. Upper insert: Field emission (FE) ZrO/W electron source tip. Lower insert: electron lenses consist of a dense set of concentric Cu-rings encircling the column. The magnetic field resulting from the current running through these Cu-elements focuses the electron beam through the Lorentz force in a helical, spiraling motion. Figures combined and adapted from [25].

2.4.1 Electron diffraction

Despite the electrons being highly energetic after being accelerated through the high voltage at the electron source, the electrons interact strongly with solid materials. The interaction is both due to the inherent elementary charge, e, as well as the associated **E**-field of the electron wave. As an example, 200 keV electrons exhibit a typical mean free path (MFP) of 130 nm in Al. The calculation of electronic MFPs is an intricate quantum mechanical problem, depending on several factors, among others the Z-number of the material. In order to achieve electron transmission, as well as clear, interpretable images, the specimens need to be made very thin. Suitable thicknesses are normally < 200 nm.

There are several different electron-specimen interactions giving rise to different scattering mechanisms, and different types of secondary signals. Some of these are shown in figure 2.9.

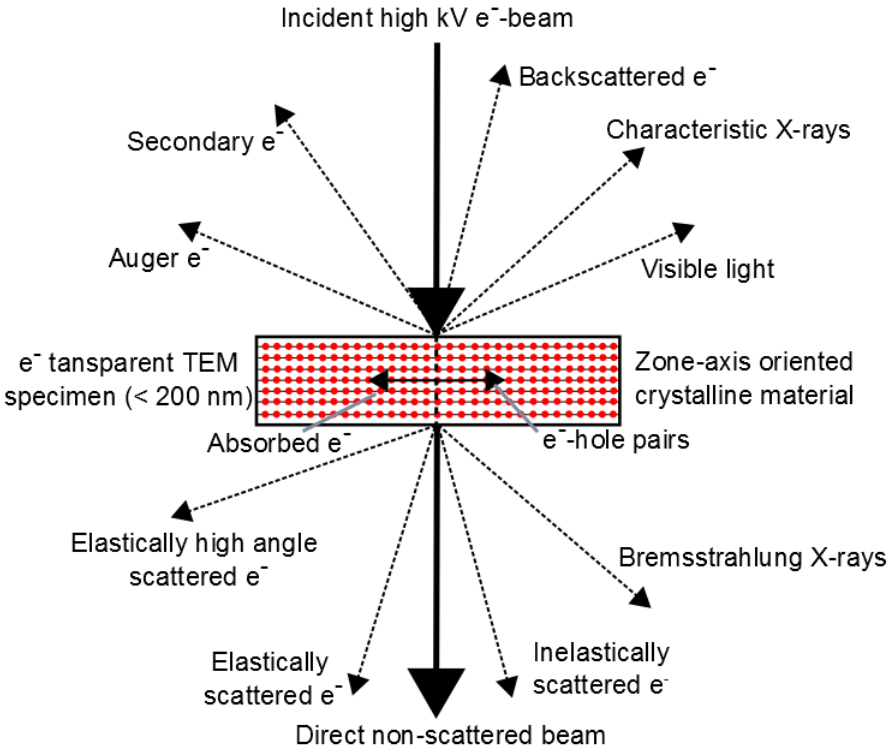

Figure 2.9: Different types of electron-specimen interactions, scattering mechanisms and secondary signals generated from electron scattering on a generic ZA oriented crystalline material. Arrows indicate relative angular distributions, greatly exaggerated for clarity.

The scattering is termed *elastic* if it leaves the state of the specimen atoms unaltered after transmission, i.e. with its initial energy, $E_0 = eU$. *Inelastic* scattering alters the state of the specimen. This can include single electron excitations, or collective excitations such as plasmon generation. Furthermore, one distinguishes coherent or non-coherent interactions dependent on whether the phase coherency is preserved after the scattering event.

The different types of interactions lead to different characteristic angular distributions, which are exploited using different imaging techniques [26].

When electromagnetic (EM) radiation with wavelength comparable to inter-atomic distances is incident upon a crystal lattice, the atomic clouds from each atom may spread the incoming radiation elastically in all directions with equal frequency. The radiation from all atoms in the lattice will interfere, which results in stringent conditions for maximum intensity distributions around the crystal. This unique set of directions in space is described by Bragg's law, the fundamental relation in diffraction theory, which reads

$$2d_{\text{hkl}} \sin(\theta_{\text{hkl}}) = n\lambda. \tag{2.7}$$

Bragg's law relates the the inter-planar distance, d_{hkl}, the scattering angle, θ_{hkl} and the wavelength, λ. Consult [15] for a concise derivation. Real space interpretation visualizes specularly scattered radiation from atomic planes (hkl), giving constructive interference when the wave path difference equal an integer multiple of wavelengths, $n\lambda$. Its well-known reciprocal space equivalent, the Laue condition, reads

$$\mathbf{Q} = \mathbf{k}_{\text{f}} - \mathbf{k}_{\text{i}} = \mathbf{g}_{\text{mno}} + \mathbf{s}. \tag{2.8}$$

Here, $\mathbf{Q}$ is the total scattering vector, and $\mathbf{k}_{\text{f}}$ and $\mathbf{k}_{\text{i}}$ denote the wave vector of the scattered and incoming electron wave respectively. The solid-state physics convention of defining $k = 2\pi/\lambda$, will be used in the following. The reciprocal lattice vector, $\mathbf{g}_{\text{mno}}$, describes a specific point in reciprocal space, corresponding to the planar set (mno) in real space. Furthermore, it is here included possible small deviations from the Bragg condition through the *excitation error*, $\mathbf{s} = \langle s_{\text{x}}, s_{\text{y}}, s_{\text{z}} \rangle$.

Equation 2.8 is visualized through the well-known Ewald-sphere construction, see figure 2.10. The excitation error connects the point $\mathbf{g}_{\text{mno}}$ in reciprocal space to the Ewald sphere in the direction parallel to the incident beam direction $\mathbf{k}_{\text{i}}$.

The construction of *Laue zones* is very useful for the indexing and computation of electron-diffraction patterns (DPs). The product of a translation vector, $\mathbf{R}_{\text{hkl}}$, of the crystal lattice and a reciprocal lattice vector $\mathbf{g}_{\text{mno}}$,

$$\mathbf{g}_{\text{mno}} \cdot \mathbf{R}_{\text{hkl}} = mh + nk + ol = N,$$

is an integer, N. If $N = 0$, all the $\mathbf{g}_{\text{mno}}$ for a given value of $\mathbf{R}_{\text{hkl}}$, lie on a plane through the origin of the reciprocal lattice and are normal to the *zone axis* (ZA), $\mathbf{R}_{\text{hkl}}$, or [hkl]. The system of lattice planes that belongs to these values of $\mathbf{g}_{\text{mno}}$ forms a bundle of planes that have the ZA as a common line of intersection. The reciprocal lattice plane that contains the corresponding $\mathbf{g}_{\text{mno}}$ is called the zero-order Laue zone (ZOLZ). For $N = 1, 2, ...$ the first- (FOLZ), second-, and higher-order (HOLZ) Laue zones, respectively, are obtained. These are parallel to the zero-order Laue zone. This means that the Laue zones are parallel sections through the reciprocal lattice, see figure 2.10.

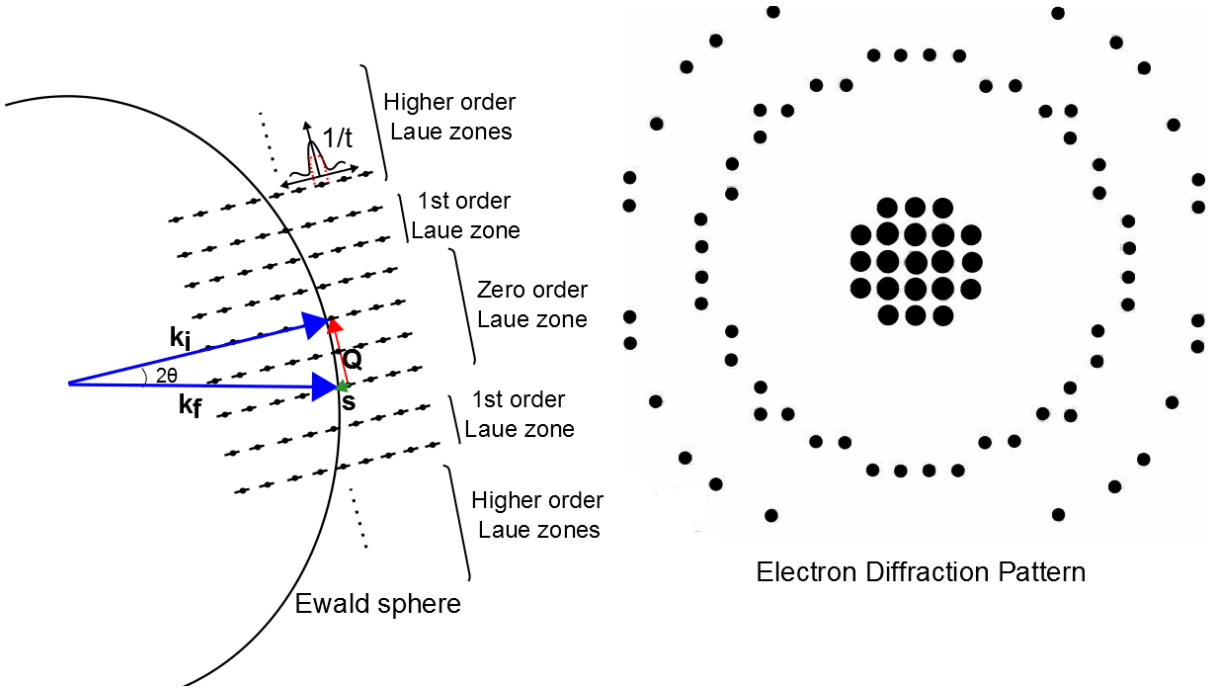

Figure 2.10: The Ewald-sphere construction for elastic scattering on a crystalline material. The reciprocal lattice points are expanded into reciprocal lattice rods in the direction normal to the incident beam, as explained through kinematic scattering theory. A typical resulting electron DP exhibiting HOLZ reflections from electron scattering on a ZA oriented crystal is shown to the right. Notations are explained in the text.

After having briefly explained the directions into which the beam can scatter, we turn to the intensity of the resulting diffraction spots. The intensity of a reflection is proportional to the square of the modulus of the *crystal structure factor*, i.e.

$$I \propto |F_{\text{crystal}}(\mathbf{Q})|^2.$$

One defines the crystal structure factor, $F_{\text{crystal}}(\mathbf{Q})$, as the amplitude of the waves scattered by the crystal at unit distance in the direction $(\mathbf{k}_\text{i}+\mathbf{Q})$, as given by equation 2.8. Assuming the crystal to be parallelepipedal in shape, with edge lengths $L_\text{i} = M_\text{i} a_\text{i}$, $i = (1,2,3)$, parallel to the fundamental vectors $\mathbf{a}_\text{i}$, the defining equation becomes [26]

$$\begin{aligned} F_{\text{crystal}}(\mathbf{Q}) &= \sum_{\text{crystal}} f_\text{j}(\mathbf{Q}) \exp\left(-\text{i}(\mathbf{Q}+\mathbf{s})\cdot(\mathbf{R}_\text{hkl}+\mathbf{r}_\text{j})\right) \\ &= \sum_{h=1}^{M_1}\sum_{k=1}^{M_2}\sum_{l=1}^{M_3} \exp\left(-\text{i}(\mathbf{Q}+\mathbf{s})\cdot\mathbf{R}_\text{hkl}\right) \sum_j f_\text{j}(\mathbf{Q}) \exp\left(-\text{i}(\mathbf{Q}+\mathbf{s})\cdot\mathbf{r}_\text{j}\right). \end{aligned} \quad (2.9)$$

The sum runs over all crystal atoms, reached through the vector sum $(\mathbf{R}_\text{hkl} + \mathbf{r}_\text{j})$. The term on the left hand side is called the *lattice amplitude*, and depends only on the external

shape of the crystal. The term on the right hand side is called the *structure amplitude*, and depends only on the positions and type of the atoms inside the unit cell. These will henceforth be denoted G and $F_{\text{uc}}(\mathbf{Q})$ respectively. As previously, $\mathbf{r}_{\text{j}}$ is the relative position of the jth atom in the basis, whose scattering is described through an *atomic scattering amplitude*, $f_{\text{j}}(\mathbf{Q})$. The atomic scattering amplitude for electrons, is in the first Born approximation given as [24]

$$f_{\text{j}}(\mathbf{Q}) = \frac{2\pi me}{h^2} \int_{-\infty}^{\infty} V(\mathbf{r}) \exp\left(-\text{i}\mathbf{Q}\cdot\mathbf{r}\right)\text{d}\mathbf{r}. \tag{2.10}$$

$V(\mathbf{r})$ is the atomic potential, and the integral is taken over the full atom extent. This is essentially a Fourier transform, reminiscent of the theory of X-ray- and optical light diffraction. For elastic scattering, $|\mathbf{k}_{\text{i}}|=|\mathbf{k}_{\text{f}}|=|\mathbf{k}|$, and hence the scattering triangle of figure 2.10 becomes isosceles. Application of the cosine-rule and the definition of the wave-number, k, yields the important relation

$$Q = \sqrt{|\mathbf{k}|^2(1-\cos^2(2\theta))} = \frac{4\pi}{\lambda}\sin\theta. \tag{2.11}$$

The atomic potential, $V(\mathbf{r})$, is related to the atomic charge density, $\rho(\mathbf{r})$, through Poisson's equation,

$$\nabla^2 V(\mathbf{r}) = -\frac{e[\rho_{\text{n}}(\mathbf{r}) - \rho_{\text{e}}(\mathbf{r})]}{\epsilon_0}. \tag{2.12}$$

Here, $\rho_{\text{n}}(\mathbf{r})$ is the charge density of the atomic nucleus, and $\rho_{\text{e}}(\mathbf{r})$ is the atomic electron density. ϵ_0 is the permittivity of vacuum. To a good approximation, $\rho_{\text{n}}(\mathbf{r})$ is taken to be a point charge of strength Z, i.e. the atomic number. Writing equation 2.10 as

$$f_{\text{i}}(\mathbf{Q}) = \frac{2\pi me}{h^2Q^2} \int_{-\infty}^{\infty} V(\mathbf{r})\nabla^2 \exp\left(-\text{i}\mathbf{Q}\cdot\mathbf{r}\right)\text{d}\mathbf{r},$$

and further doing integration by parts, making use of $V(-\infty) = V(\infty) = 0$, gives

$$f_{\text{i}}(\mathbf{Q}) = -\frac{2\pi me}{h^2Q^2} \int_{-\infty}^{\infty} \exp\left(-\text{i}\mathbf{Q}\cdot\mathbf{r}\right)\nabla^2 V(\mathbf{r})\text{d}\mathbf{r}. \tag{2.13}$$

Now, substituting equation 2.12 into equation 2.13 gives

$$\begin{aligned} f_{\text{i}}(\mathbf{Q}) &= -\frac{2\pi me^2}{\epsilon_0 h^2Q^2} \int_{-\infty}^{\infty} \exp\left(-\text{i}\mathbf{Q}\cdot\mathbf{r}\right)[Z\delta(\mathbf{r}) - \rho_{\text{e}}(\mathbf{r})]\text{d}\mathbf{r} \\ &= -\frac{2\pi me^2}{\epsilon_0 h^2Q^2}[Z - f^{\mathbf{X}}(\mathbf{Q})], \end{aligned} \tag{2.14}$$

where $f^{\mathbf{X}}(\mathbf{Q})$ is the scattering factor for X-rays. Equation 2.14 is the Mott formula [24]. This equation directly relates the electron and X-ray scattering factors. The first term is due to Rutherford scattering by the nucleus, which is recognized by making use of equation 2.11 defining Q. The second term is due to scattering by the atomic electrons.

Now, substituting equation 2.8 into the lattice sum of equation 2.9, and using $\mathbf{g}_{\text{mno}} \cdot \mathbf{a}_{\text{i}} = N$, where N is an integer, it becomes

$$G = \sum_{h=1}^{M_1} \sum_{k=1}^{M_2} \sum_{l=1}^{M_3} \exp[-i(\mathbf{Q} + \mathbf{s}) \cdot \mathbf{R}_{\text{hkl}}] = \sum_{h,k,l} \exp(-i\mathbf{s} \cdot \mathbf{R}_{\text{hkl}}).$$

The phase, -$i\mathbf{s} \cdot \mathbf{R}_{\text{hkl}}$, varies very slowly in moving through the crystal. It can therefore, to a good approximation, be replaced by an integral over the crystal volume $V = L_1 L_2 L_3$. With the volume of the unit cell, $V_{\text{e}} = a_1 a_2 a_3$, one obtains

$$\begin{aligned} G_{\text{x}} = \frac{1}{a_1} \int_{-L_1/2}^{L_1/2} \exp(-is_{\text{x}}x)\mathrm{d}x &= \frac{1}{\pi s_{\text{x}} a_1} \frac{\exp(\pi i s_{\text{x}} L_1) - \exp(-\pi i s_{\text{x}} L_1)}{2i} \\ &= \frac{\sin(\pi s_{\text{x}} M_1 a_1)}{\pi s_{\text{x}} a_1}, \end{aligned}$$

in total giving

$$I(\mathbf{Q}) = |F_{\text{uc}}(\mathbf{Q})|^2 |G|^2 = |F_{\text{uc}}(\mathbf{Q})|^2 \frac{\sin^2(\pi s_{\text{x}} M_1 a_1)}{(\pi s_{\text{x}} a_1)^2} \frac{\sin^2(\pi s_{\text{y}} M_2 a_2)}{(\pi s_{\text{y}} a_2)^2} \frac{\sin^2(\pi s_{\text{z}} M_3 a_3)}{(\pi s_{\text{z}} a_3)^2}. \tag{2.15}$$

The typical TEM specimen is approximately a thin plate, thickness t, with its lateral dimensions L_2 and L_3 far exceeding t. The *sinc*-terms of equation 2.15 tend to δ-functions for large L_2 and L_3. The total intensity diffracted by a thin plate of thickness, t, is thus

$$I(\mathbf{Q}) = |F_{\text{uc}}(\mathbf{Q})|^2 |G|^2 = \frac{|F|^2 L_2 L_3}{V_{\text{e}}^2} \frac{\sin^2(\pi t s_{\text{x}})}{(\pi s_{\text{x}})^2} \delta(s_{\text{y}}) \delta(s_{\text{z}}). \tag{2.16}$$

Equation 2.16 shows that the intensity $I(\mathbf{Q})$ is spread out in the form of a spike normal to the crystal plate. This is also the well-known diffracted intensity distribution in optics from a slit of width t. The full width at half maximum (FWHM) in reciprocal space is approximately t^{-1}. The consequence in the Ewald-sphere construction is that to extend the point to lines of width t^{-1} in the direction normal to the crystal plate. The resulting rods are known as reciprocal lattice rods, or *rel-rods* for short, see figure 2.10.

One can further calculate the absolute intensity emerging from the crystal. Consider the total intensity scattered into a solid angle $\mathrm{d}\Omega$ about the diffracted beam. In real space, $r^2 \mathrm{d}\Omega = \mathrm{d}S$, where $\mathrm{d}S$ is an area element on a plane of radius r. In reciprocal space, $\mathrm{d}\Omega = \mathrm{d}s_{\text{y}} \mathrm{d}s_{\text{z}} / k^2 \cos\theta$. Hence, the total intensity scattered over the sphere of radius r about the diffracted beam direction, $\mathbf{k}_{\text{f}} = \mathbf{k}_{\text{i}} + \mathbf{Q}$, is

$$\int I(\mathbf{Q})\mathrm{d}S = \int |F_{\mathrm{uc}}(\mathbf{Q})|^2|G|^2\mathrm{d}S = \frac{|F_{\mathrm{uc}}(\mathbf{Q})|^2 L_2 L_3}{k^2 V_{\mathrm{e}}^2 \cos\theta}\frac{\sin^2(\pi t s_{\mathrm{x}})}{(\pi s_{\mathrm{x}})^2}\int \delta(s_{\mathrm{y}})\mathrm{d}s_{\mathrm{y}}\int \delta(s_{\mathrm{z}})\mathrm{d}s_{\mathrm{z}}.$$

Now, $L_2 L_3 \cos\theta$ is the area of the crystal projected along $\mathbf{k}_{\mathrm{f}} = \mathbf{k}_{\mathrm{i}} + \mathbf{Q}$. Hence, the intensity per unit area of the diffracted beam is

$$I(t) = \frac{|F_{\mathrm{uc}}(\mathbf{Q})|^2}{k^2 V_{\mathrm{e}}^2 \cos^2\theta}\frac{\sin^2(\pi t s_{\mathrm{x}})}{(\pi s_{\mathrm{x}})^2}.$$

Now, it is common to rename $s_{\mathrm{x}} = s$, being the component of **s** normal to the crystal plate, and to introduce the *extinction length*, ξ_{g}, having units of length, defined as

$$\xi_{\mathrm{g}} = \pi k V_{\mathrm{e}} \cos\theta / F_{\mathrm{uc}}(\mathbf{Q}).$$

Typical values for ξ_{g} are a couple of hundred Å.

Finally, the intensity scattered through 2θ, as given by Bragg's law (equation 2.7), in the gth diffracted beam from a crystal of thickness t, in the kinematical theory, is thus

$$I(t) = \left(\frac{\pi}{\xi_{\mathrm{g}}}\right)^2 \left(\frac{\sin(\pi t s)}{\pi s}\right)^2.$$

Now, here comes an important warning sign, normally negligible in the theory of X-ray diffraction. $I(t)$ cannot be greater than unity, i.e. the incident beam intensity. At the exact Bragg position, $s = 0$, and

$$I(t) = \left(\frac{\pi t}{\xi_{\mathrm{g}}}\right)^2.$$

Hence, an upper limit of the foil thickness, t_{max}, for which kinematical theory is valid at the Bragg position is $t_{\mathrm{max}} = \xi_{\mathrm{g}}/\pi$. With typical extinction distances in the range of a few hundred Å, $t_{\mathrm{max}} \approx 100$ Å. In fact, this is very much an upper limit, as kinematical theory assumes a single scattering event, and hence assumes that the diffracted beam is very much weaker than the incident beam. For larger deviations s, from the exact Bragg condition, the kinematical theory holds to a slightly better extent.

With typical TEM specimen thicknesses in the range 50-150 nm, it is apparent that in electron diffraction there is need for an extended theory including dynamical effects. Furthermore, due to the high electron speeds obtained, a theory of diffraction and electron microscopy must take into account relativistic effects. Fortunately, it is found that correcting for relativistic masses $m = m_0(1 - v^2/c^2)^{-1/2}$, and wavelengths (see equation 2.6), adequately accounts for this aspect.

The intensities diffracted from a perfect crystal of thickness, t, at the Bragg position $s = 0$ in the *two-beam* dynamical theory are

$$I_0(t) = \cos^2(\pi t/\xi_g)$$
$$I_g(t) = \sin^2(\pi t/\xi_g).$$

In multiple scattered waves there are dynamic exchanges of intensity between different Bragg diffracted beams. This alters the intensity distribution in the diffraction plane. Among other important results, some kinematically forbidden reflections can be present in the diffraction pattern. The theory quickly becomes intricate, and is far to extensive to include in this section. Suggested literature is found in [24] and [26]. The basic topics have been covered, and most importantly, it is shown that dynamical effects are of importance in electron diffraction experiments, which will be shown later in this thesis.

2.4.2 TEM operation modes

The TEM is a powerful analytical tool, capable of extracting a range of complementary information about specimens under study, and achieving this at a very high spatial resolution, in some cases, world leading. There exists a wealth of different operational modes, each of which is specialized to highlight a specific specimen aspect.

Common for all the different imaging techniques in TEM, is that the electrons having transmitted the specimen are detected. Techniques using only the non-scattered electrons are used in Bright-Field (BF) microscopy. Using the elastically scattered electrons provides diffraction, or Dark-Field (DF) microscopy. The inelastically scattered electrons are used in different spectroscopy techniques, in addition to characteristic X-rays and electrons emitted by the specimen due to excitation of the constituent atoms. The main imaging techniques applied are described in more detail in the following. Figure 2.8 provides a nice reference for the different instrumental aspects mentioned below.

Starting at the very top of the TEM column sits the electron gun. Here, the electrons are withdrawn from an electron source, and subsequently accelerated over the high-tension (HT) voltage. Then, through a series of lenses, deflectors and apertures, the electron beam is either focused to a very small, convergent probe, or it is adjusted to a broader parallel beam impinging onto the specimen plane. This upper part of the column is referred to as the condenser lens system, see figure 2.11, indicating its purpose of ensuring a condensed beam.

The most important lens in the TEM is the *objective lens* (OL), which comes directly before or after the specimen plane, depending on whether one applies a STEM or TEM setup respectively. After having transmitted the specimen, the electrons originating from a certain point in the specimen plane, are focused by the OL to a certain point in the image plane of the OL. In *imaging mode*, this is the plane captured on the fluorescent screen, or the CCD camera, after it has been further magnified by intermediate lenses. In imaging

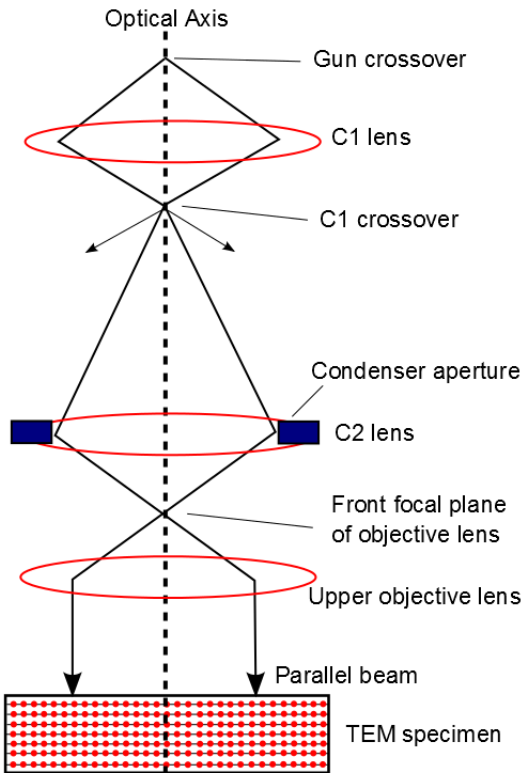

Figure 2.11: Ray diagram through the condenser lens system of the TEM. Figure adapted from [25].

mode, there are mainly three different techniques; BF-, DF- and HRTEM.

Bright-Field TEM: In BFTEM, only the direct, non-diffracted beam is used to form an image of the specimen. This is realized by placing a small objective aperture (OA) in the back focal plane (BFP) of the OL. This is the plane where the DP is formed. By placing the OA over the central 000-spot, i.e. the non-diffracted beam, and thus blocking out all other diffracted beams, one obtains a BF-image. The method renders specimen features that are symmetrically oriented with respect to the incident beam dark. A BFTEM ray path schematic is shown in figure 2.12 (a).

Dark-Field TEM: Similarly, by selecting one or multiple diffracted spots in the DP plane, one obtains a DF-image. Simply put, it bears some resemblance to a negative of BF-images. The DP holds key information regarding the specimen microstructure, and by selecting different DP reflections, one can highlight many interesting features of the material. For instance, in a stack of different materials, such as a heterogeneous semiconductor, one can select the diffraction spots corresponding to the different layer lattice spacings, hence forming an image of this layer individually.

High-Resolution TEM: In HRTEM, no OA is inserted, as this put in analogy works as a low-pass frequency filter. Non-diffracted and all diffracted beams are allowed to interfere and form an image. The image is further strongly magnified by the intermediate lenses. This constitues a powerful technique, capable of obtaining atomic resolutions, see figure 2.3. Image interpretation can on the other hand become more difficult, as complex interference phenomena and dynamical effects can seemingly correspond to real specimen features.

Diffraction mode: If the sample is crystalline, there will be strong intensity peaks in certain directions, as determined by the crystal structure and orientation, elaborated in the preceding section. In diffraction mode, rays that leave the sample with a specific angle, will be focused to a specific point in the BFP of the OL. A DP is thus formed onto this plane. By adjusting the intermediate lens system, this plane can be projected onto the screen, thus obtaining diffraction mode, see figure 2.12 (b). This is one of the great advantages of the TEM, i.e. to easily switch between the two powerful modes of operation.

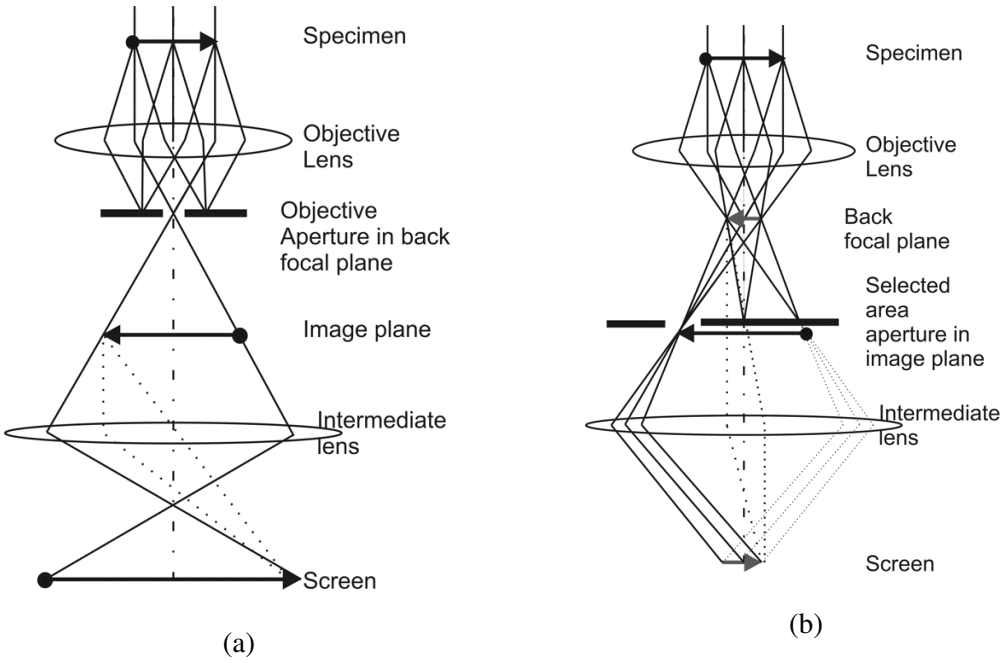

Figure 2.12: (a) Ray propagation through the TEM column in BFTEM imaging mode. The OA only allows the non-diffracted beams to pass on to form the final image. (b) Ray propagation in diffraction mode. Rays that leave the sample with a specific angle are here focused to a specific point in the BFP of the OL. In this plane, a selected area aperture is inserted. This is seen to only allow these specific electrons to pass on to form the final image. Figures adapted from [27]

Scanning TEM: In STEM, information about the specimen is collected in a serial acquisition mode. Unlike the image mode, the specimen is illuminated with a convergent electron beam which is focused to a small spot at the height of the specimen plane. To

record an image, the electron probe is scanned within a rectangular area of interest on the specimen. On each position, the probe is propagated through the specimen, and due to electron scattering, part of the electrons are scattered away from their initial trajectories. The scattering distribution in the far-field behind the specimen corresponds to a DP. Since the electron probe is convergent, the DP contains reflection discs as opposed to the normal spots. The total electron intensity hitting the detector of choice, which selects a certain angular range, is integrated to yield a total pixel intensity.

If the crystal spacing is large enough, or the convergence angle is sufficiently large, the diffraction disks in the diffraction pattern partially overlap. This coherent partial overlap is a requirement for achieving atomic resolution.

BF-STEM: Positioning a circular electron detector on the forward scattered beam yields a bright-field STEM micrograph. If there are no scatterers in the beam path, the signal will correspond to the total beam current. If there are, the BF-signal corresponds to the total beam current minus the integrated intensity that is scattered to angles beyond the area of the BF-detector.

(HA)ADF-STEM: By using an annular detector, instead of recording the forward scattered beam, one records an annular dark-field (ADF) signal. The BF- and ADF-signals are complementary to each other. If there are no scatterers in the beam path, the ADF signal is zero. If there are, the ADF signal reflects the scattering power (for the selected annular range) of the object in the beam path. The selected angular range can be adjusted by changing the magnification of the projected DP on the detector. A common configuration is to choose a high-angle ADF- (or HAADF-) setting which collects the electrons scattered to high angles. The integration of the high-angle scattering over a large area warrants that coherence effects are suppressed and averaged out [28]. This is a second powerful technique which can obtain atomic resolutions, with the important addition of Z-contrast and reduced coherence effects. Image interpretation becomes much easier than for HRTEM.

Nano-Beam Diffraction: In NBD-mode, one applies a very small, collimated beam focused to a spot with a typical size of 1 nm (with a field emission gun (FEG) source). The beam is in a near parallel configuration, having only a slight convergence angle, α. This allows recordings of DPs from small specimen regions. The diffraction spots will be expanded into small discs due to the finite convergence angle. A closely related diffraction mode, **Convergent-Beam Electron Diffraction** (CBED), uses a small beam with a large convergence angle. In this mode the discs greatly expand, and features within the discs related to dynamical scattering and underlying point- and space groups of the material can be discerned. Schematics of the ray propagation in these diffraction modes are shown in figure 2.13 (a) and (b).

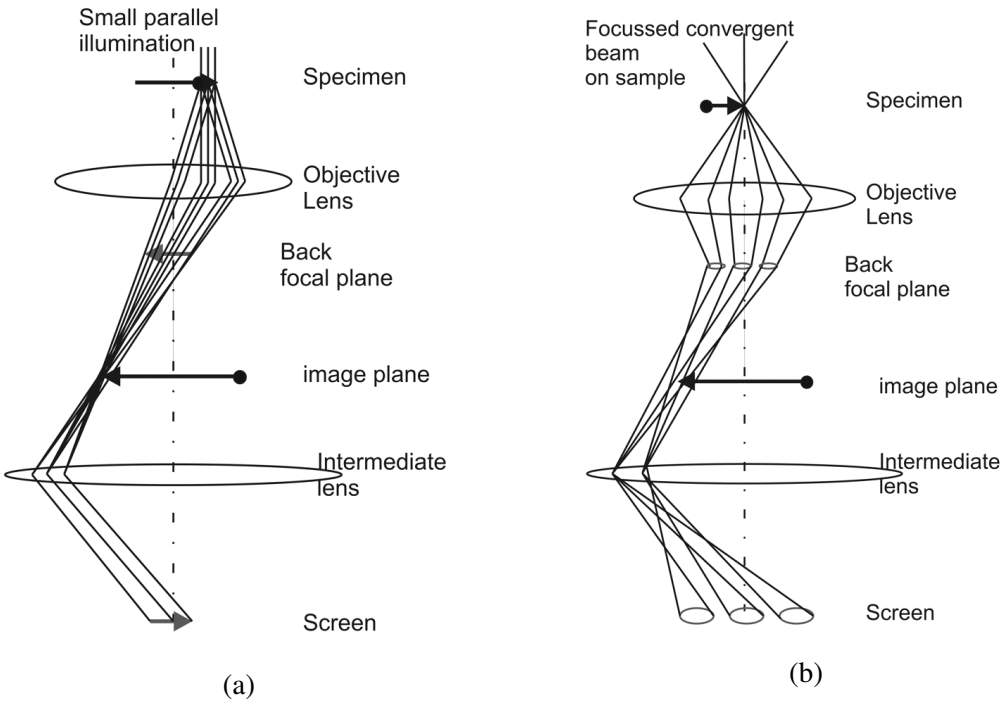

Figure 2.13: (a) Ray propagation through the TEM column in a near parallel illumination in the NBD-mode. (b) Ray propagation through the TEM column in the CBED-mode. The reflections in CBED is seen to consist of expanded diffraction pattern discs. The focused probes in both operation modes allow the study of small specimen areas. Figures adapted from [27].

2.4.3 Scanning precession electron diffraction

The main experimental technique employed throughout this thesis is a modification and combination of two more conventional techniques, briefly explained in the foregoing section. In this work, SPED was used in a modified NBD-setup. The NBD-mode ensures a very narrow beam coupled with a small convergence angle, α. This allows diffraction studies of small specimen areas, and makes the diffraction spots expand to smaller discs, see figure 2.14 (b). In this mode it is introduced an additional *precession* angle, φ. The beam thus transmits the specimen at an incoming angle φ, to the optical axis, and in addition having an inherent convergence angle α. Furthermore, the deflected beam is made to precess in circular motion around the optical axis, while maintaining a near constant probe size on the specimen plane. In the subsequent column stages, the precessing motion is 'undone', thus re-obtaining a beam running in parallel to the optical axis. The net result being a 'hollow-cone' rocking motion of the beam above, and ('de-rocking') below the specimen, see figure 2.14 (a).

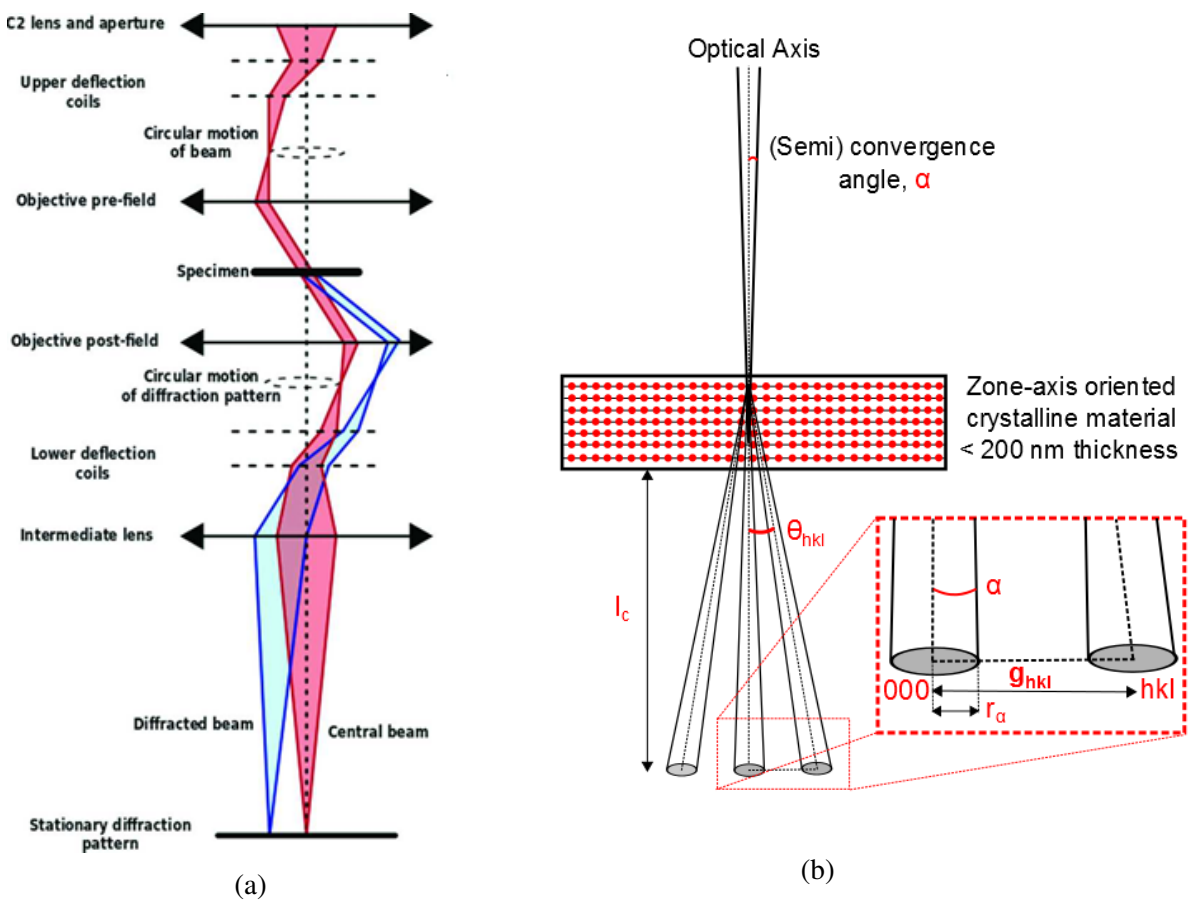

Figure 2.14: (a) Beam propagation through the optical system in the (S)PED setup. Red and blue rays indicate two differently diffracted ray paths running through the TEM column [29]. (b) Ray path schematic illustrating diffraction from a ZA oriented crystal applying a convergent beam, and the resulting DP discs. The notations have been introduced in the section on diffraction theory, apart from l_c and r_α, which denote the employed camera length and diffraction disc radius respectively.

From its introduction, some 20 years ago [30], PED has grown to become a vital tool in electron crystallography. It is primarily used in two ways: to determine crystal structures, by identifying lattice parameters and symmetry, ultimately solving the atomic structure *ab initio*. The second, doing Scanning PED, for mapping the local orientation of the specimen, allowing investigation of texture, rotation and strain at nm-scale [29].

The advantages of PED arise due to the ability of recording a larger number of reflections than in a conventional selected area electron diffraction (SAED) pattern, see figure 2.15. This is due to an effective 'integration' across the Bragg condition due to the precessing beam. The hollow-cone rocking motion of the beam necessarily translates to a similar motion of the Ewald-sphere construction. The Ewald-sphere excites different reflections during its rocking motion, which is what is meant by an effective 'integration'. The resulting intensities are in a sense 'more kinematic' in nature, among others due to an averaging over specimen surface buckling by the precessing motion. The intensities of weaker reflections become relatively stronger, as seen from this figure. Cited references further explain and motivate this technique. It is applied throughout this thesis on multiphase Al alloys, which in theory would greatly benefit from a powerful crystallographic technique.

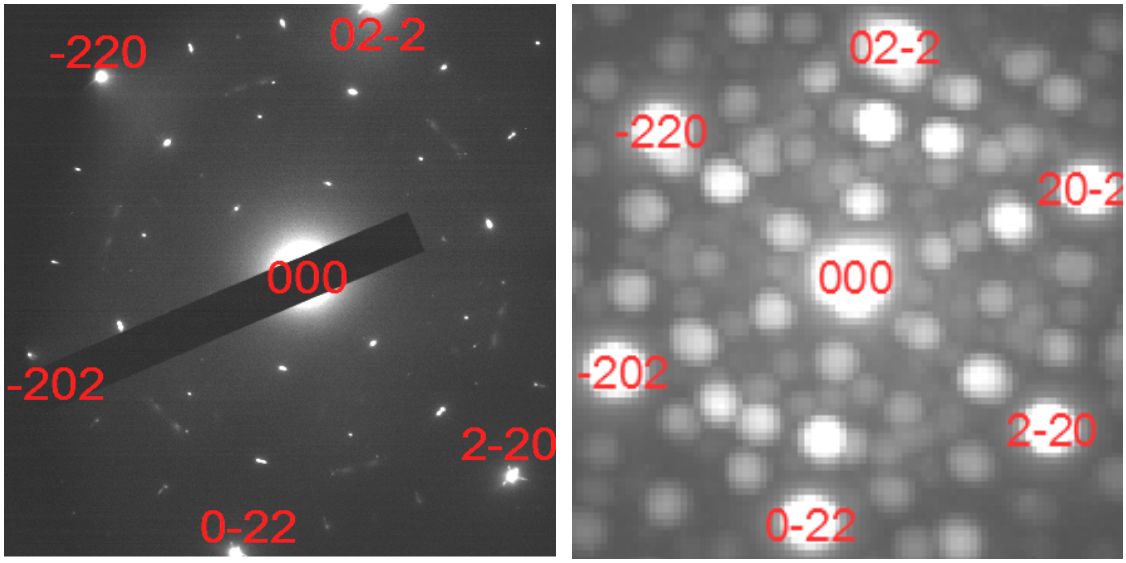

(a) (b)

Figure 2.15: (a) Recorded SAED pattern from a $[111]_{Al}$ ZA oriented grain in alloy CL. An inserted beam stopper is seen blocking the bulk of the 000-reflection. (b) Sum of 40 000 PED patterns acquired near the $[111]_{Al}$ ZA in alloy CL. It was recorded at approximately the same area as the SAED pattern in (a), using a precession angle of 1°.

Chapter 3

Experimental Methods

This chapter explains the experimental procedures used throughout this thesis. The presentation is divided in three sections. First presented are the two 2xxx series Al alloys studied, and the thermo-mechanical pre-treatments applied in obtaining over-aged (OA) alloy conditions. Consequently, the conducted TEM studies are elaborated. Here, the SPED setup and scan parameters used are explained. The third and final section explains the different data processing procedures applied in working with the acquired SPED data.

3.1 Materials and Heat Treatments

The two Al alloys investigated in this thesis were obtained from the global materials manufacturer American Elements [31] in the form of 4 kg bolts. Upon arrival, the alloys were further extruded into long cylindrical bars with a diameter of 20 mm, using a ram speed of 0.5 mm/s. After extrusion, they were cut into many smaller cylinders each some 13 mm high. The nominal elemental compositions of the two alloys are given in table 3.1, which is re-given from the opening pages of this thesis for simplicity. The alloys form a part of the materials selection in the FRINATEK project, No. 221714. The property measurements on alloy CL, together with TEM specimen preparation procedures, are contained in the author's project work [32]. Therefore, for a complete specimen preparation procedure from cut cylinders to electron transparent TEM specimens, this work should be consulted. The same preparation procedure was used for alloy MCA.

The two alloys were given different heat treatment procedures. The following pre-treatments are better understood in conjunction with figure 2.4. Both alloys were subjected to 4 hours of homogenization. Homogenization temperatures were set to 440 °C for alloy MCA, and 400 °C for alloy CL. The alloys were pre-heated to a temperature slightly above extrusion temperatures. 400 °C and 380 °C were used for alloy MCA and CL respectively. Extrusion was conducted at $\approx$ 390 °C and $\approx$ 370 °C for MCA and CL respectively. The temperatures may increase beyond the stated ones during extrusion, but the profiles were water cooled directly after emerging from the extrusion press, hence it should not deviate significantly.

Table 3.1: Nominal elemental compositions of the two alloys Al-Mg-Cu-Ag (MCA) and Al-Cu-Li (CL). They are given as atomic percentages, at.%, and weight percentages, wt.%.

MCA	Elements							
at.%	Al	Mg	Cu	Ag	Fe	Mn	Other	Total solute
	97.05	1.137	1.305	0.128	0.099	0.277	<0.01	2.95
wt.%	Al	Mg	Cu	Ag	Fe	Mn	Other	Total solute
	94.75	1.000	3.000	0.500	0.200	0.550	<0.01	5.25
CL	Elements							
at.%	Al	Cu	Li	Si	Fe	Mn	Other	Total solute
	92.69	1.246	5.704	0.0	0.095	0.264	<0.01	7.31
wt.%	Al	Cu	Li	Si	Fe	Mn	Other	Total solute
	94.75	3.000	1.500	0.0	0.200	0.550	<0.01	5.25

Solution heat treatment was carried out in a liquid salt bath at 440±1 °C for the MCA alloy, and 500±1 °C for the CL alloy. The liquid salt maintains an even temperature distribution throughout, and ensures an efficient heating of submerged samples. The temperature was monitored at even intervals using a thermocouple Amprobe TM45A. The SHT time was set to 1 hour for both alloys, which was deemed sufficient in order to distribute the alloying elements homogeneously throughout the Al matrix. After SHT, the alloys were quickly water quenched to room temperature (RT), thus obtaining super-saturated solid solutions.

In order to avoid any natural ageing effects, the alloys were directly set to artificial ageing, only exposed to a few seconds of RT. The AA procedure was conducted in oil-baths at 170±1 °C. The samples were serially heat treated for a certain amount of time before quickly water quenched to RT. After quenching, Vickers hardness (HV5) and electrical conductivity measurements were made before the samples were set for further AA.

The sought alloy condition is over-aged (OA). In this condition, most precipitates take on more stable forms, exhibiting their largest dimensions. Additionally, there are fewer intermediate phases along the precipitation sequences coexisting. This should allow for a more simplified microstructure characterization based on diffraction techniques. Plotted HV5 measurements indicated the time at which OA condition was obtained. This was reached after 4 h of AA for the MCA alloy, and a total of 64 days for the CL alloy. Figure 3.1 (a) and (b) show the total heat treatment times used in obtaining the OA conditions in both alloys, omitting the intervening property measurements. RT was monitored regularly at 20±2 °C.

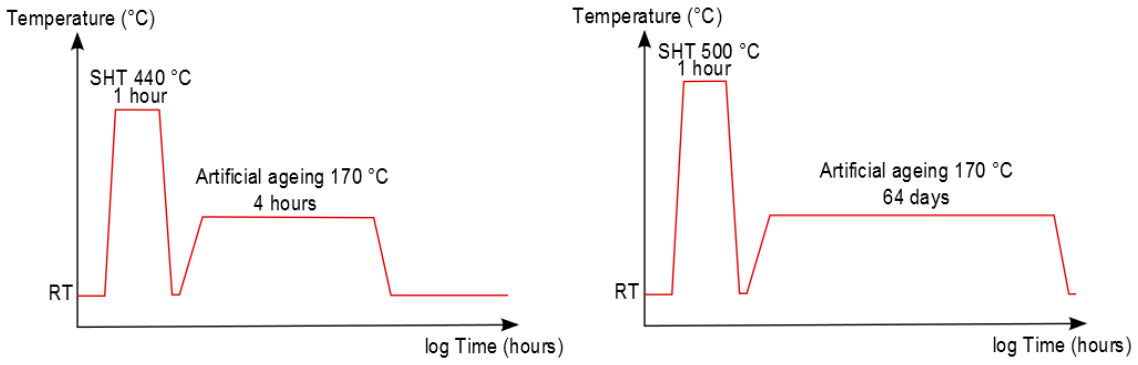

(a) (b)

Figure 3.1: Overview of the heat treatment procedures applied in obtaining OA conditions in alloys MCA (a) and CL (b). The rapid falls in temperature indicate water quenching to RT, and the rapid rises represent the efficient heating of salt- and oil-baths.

3.2 TEM Studies

The main experimental work in this thesis was carried out on a JEOL JEM-2100F (S)TEM microscope, equipped with a ZrO/W field emission gun (FEG), operated at a high tension (HT) of 200 kV. The instrument is shown in figure 3.2. The microscope forms part of the Norwegian Centre for Transmission Electron Microscopy (NORTEM) infrastructure at the TEM Gemini Centre, NTNU, Trondheim. It is the level two microscope (out of three), and allows for a multitude of different complementary techniques with emphasis on: scanning probe techniques (e.g. STEM), precession electron diffraction (PED), tomography and focused probe energy-dispersive X-ray spectroscopy (EDX), all at high spatial resolution ($\approx$ 2 Å).

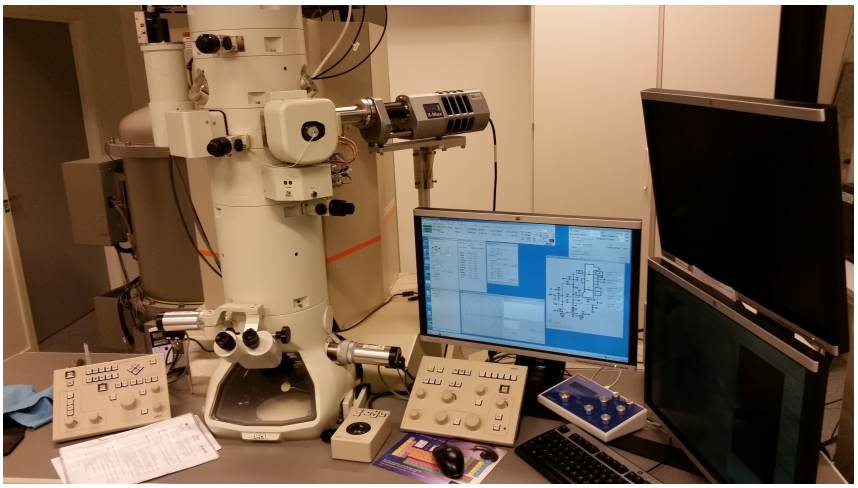

Figure 3.2: The JEOL JEM-2100F FEG (S)TEM at the TEM Gemini Centre, NTNU.

3.2.1 Scanning precession electron diffraction

The precession angle, φ, of the PED-mode, was introduced in an aligned NBD-mode using the set of deflection coils in the stages before the specimen plane. Using an oscillating control signal, the deflected beam was made to precess in circular motion around the optical axis, while maintaining a near constant probe size on the specimen plane. In the subsequent column stages, the lower deflection coils were used to retain a beam running in parallel to the optical axis, see figure 3.3 below.

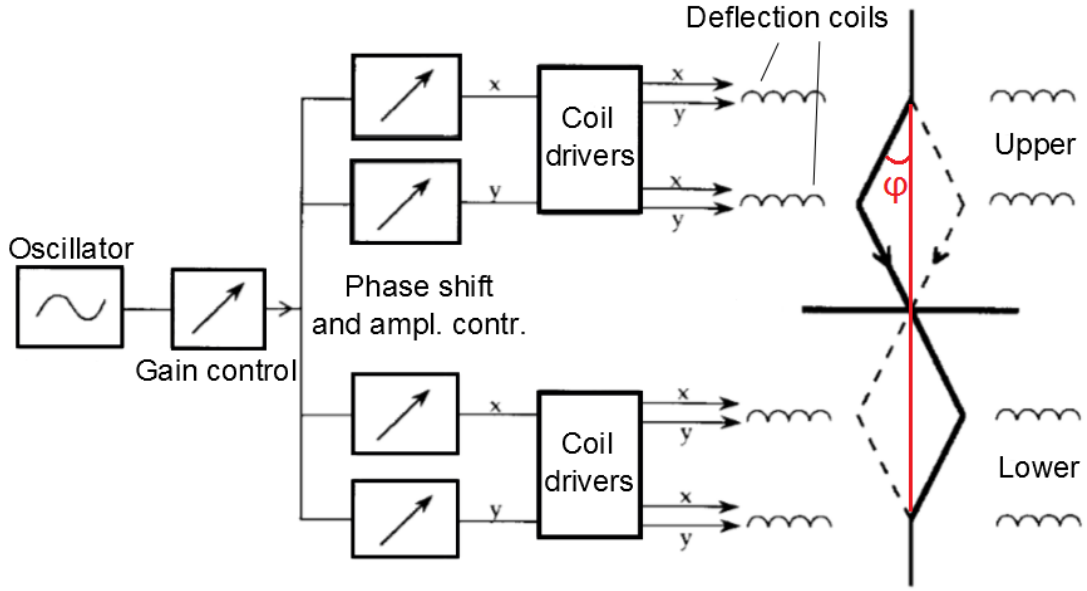

Figure 3.3: Schematic of the beam precession controls and ray paths through the specimen plane in the PED-mode. The precession angle, φ, is highlighted. Figure adapted from [30].

SPED is a serial acquisition technique where the beam is raster scanned across a rectangular area of interest on the specimen, typically a couple of 100s pixels squared, similar to STEM-mode. In each pixel, a PED pattern is recorded while the beam is being precessed around the optical axis for a specified dwell time, t_d. The rocking-, de-rocking motion ensures that integrated diffraction intensities are recorded in the geometry of a conventional electron DP [30]. In total, a 4D data set is obtained comprising a 2D PED pattern at each position in the 2D scan region.

The hardware control setup used a NanoMEGAS DigiSTAR [33] scan generator fitted to the JEOL 2100F as described in [5]. Each PED pattern forming on the fluorescent screen was captured using an external StingRay CCD camera attached to the position of the binoculars. While recording the PED patterns, the fluorescent screen chamber and mounted camera were covered, thus reducing the amount of contaminating photons recorded in each pattern. Furthermore, all external lighting in the room, including PC monitors, were shut off. The screen was further tilted $\approx 30^\circ$ in order for the camera to run perpen-

dicular to the screen.

In order to reduce carbon-contamination levels building up due to the high current in the focused NBD-spot, the specimens were cleansed using an Ar- and O-ion beam in a Fischione Plasma Cleaner (Mod. 2010). This was done prior to TEM studies. Applied plasma cleaning duration ranged from 1-3 min.

Table 3.2: SPED scan parameters, with employed value ranges as obtained in NBD-mode on the JEOL 2100F microscope.

Parameter	Symbol	Employed value range
Spot Size	s	0.5-1 nm
Convergence Angle	α	0.83, 1.00 or 1.24 mrad (instrument α-setting: 3-5)
Dwell Time	t_d	20-60 ms
Precession Angle	φ	0.5-1°
Camera Length	l_c	20-80 cm
Step Length	l_s	0.64-4.5 nm
Precession Frequency	f	100 Hz

3.2.1.1 ZA SPED scans

The different SPED setup parameters, together with applied value ranges, are displayed in table 3.2. Running scans over larger regions in ZA oriented Al grains, NBD-mode was used with a condenser aperture of 10 µm and typically a (unprecessed) spot size of 1 nm. The precession angle, φ, was set to 1°, which was found to give rich details in recorded PED patterns, as well as allowing for sufficiently good system alignments. This is on account of an increased effective spot size, but for ZA scans the employed step sizes exceed this extent.

The NBD-mode convergence angle, α, was normally set to 1.24 mrad (instrument specific α-setting 5), giving the largest diffraction discs obtainable in this mode. The precession frequency was set to 100 Hz, and kept fixed for all experiments. The dwell time used was a multiple of 10 ms, thus ensuring an integer full rotation on each specimen point. The common setting used was a 20 ms dwell time for ZA scans.

The scanned specimen area typically ranged from 576 nm^2 to 1.8 μm^2, using either 300^2 or 400^2 pixels. The used pixel to pixel step size, l_s, was in the range 1.92-4.5 nm, depending on the area size. Each PED pattern was recorded using camera lengths of 30 or 40 cm, which was deemed optimal in regards of recorded diffraction spot intensities. A typical 300^2 pixels scan using a dwell time of 20 ms, takes some 30 min time. Increasing it to 400^2 pixels with equal dwell time being equal, increases it to about 1h 30 min.

3.2.1.2 Dispersoid SPED scans

Also present in the matrix of the 2xxx series Al alloys are Al-Cu-(Mn,Fe) dispersoids (T-particles). The T-particles exist in different morphologies, some of which are rod-shaped, and elongated along the $\langle 001 \rangle_{Al}$ directions. This type has an interesting rotation-twinned substructure exhibiting 10-fold rotation symmetry [34], which is apparent when viewed head-on. The dispersoid area when viewed in this direction is typically < 90 nm in extremal lengths.

Smaller area SPED scans were acquired from these structures in order to; assess whether the SPED technique can confirm their rotation-twinned character, and to push the technique towards its spatial resolution limit. Dispersoid region scans were taken on areas < 300 nm^2, and required careful adjustment and refinement of scan parameters in order to achieve the highest obtainable spatial resolution. For these refined scans, NBD-mode was used with a condenser aperture of 10 µm and a (unprecessed) spot size of 0.5-0.7 nm. φ was set to 0.5-0.7°. The NBD-mode convergence angle was set to 0.83 or 1.00 mrad, (alpha-setting 3 or 4), giving sufficiently resolved diffraction discs for the dense dispersoid reflections. Dwell time used was either kept at 20 ms, or increased to 40 ms. This meant higher accumulated beam exposure, but due to the smaller probe, this was necessary in order to record sufficient intensities.

Scanned dispersoid areas used either 100^2 or 200^2 pixels. The employed step size was in the range 0.64-1.92 nm. Each PED pattern was recorded using camera lengths of 30 or 40 cm.

3.2.2 Conventional imaging techniques

As a means of comparison to the virtual images obtained from the SPED data sets, several conventional techniques for routine precipitate imaging were also used. The different techniques included; HRTEM, BF- and DFTEM, and HAADF- and BF-STEM. They were all taken on the JEOL JEM-2100F FEG microscope using a HT of 200 kV.

Some of the images were taken at the same specimen areas where SPED scans were conducted. However, in acquiring high-quality images providing fair technique comparisons, it was necessary to take some of the images at similar orientations, but at different specimen areas. This was a consequence of the time limitation of a typical TEM session booking. Acquiring good SPED data sets from a specimen area, followed by conventional imaging at identical positioning, requires several hours of work. Due to the difficulty in TEM work with retrieving an imaged area in a following microscope session, high-quality images were usually not taken at the same area. Furthermore, the focused probe and culminated long exposure times in SPED scans, lead to significant levels of carbon-contamination. This further hinders high quality imaging in the area of interest.

3.3 Data Processing

As opposed to CTEM imaging, obtaining images from the SPED scan data is done post-session by data processing of the acquired PED pattern stacks. Furthermore, this is not the only information obtainable, as will be shown. The following sub-sections explain the different data processing procedures applied in working with the obtained SPED data. In processing the large data obtained, it was used a Dell desktop computer, equipped with a 3.40 GHz i7 (3770 mod.) processor (4-cores), with 32 GBs of RAM.

3.3.1 Virtual imaging

The obtained SPED data sets comprised 10 000s of PED patterns, typically ranging from 1-5 GBs of data. Following the development of modern TEM methodologies, subsequent data processing is necessary in order to extract valuable information. In doing data processing, the open source platform HyperSpy [35] was used as described in the following. HyperSpy is a powerful Python [36] library facilitating data processing of multidimensional data sets. The SPED data sets comprise a 4D data set, comprising thousands of 2D PED patterns recorded in each pixel of a 2D specimen area.

Among HyperSpy's basic features, it facilitates the use of a *virtual aperture* (VA), whose size and placement in the PED pattern stack can be adjusted. Each PED pattern is stored as a 144^2 pixels image (fixed software setting), and the VA is positioned at specified (x,y) coordinates in the full pattern stack, using adjustable diameter pixels. The function is similar to TEM operation, where real apertures are inserted into the microscope column. In conventional SAED, this inserted aperture only allows electrons being scattered within the aperture area to pass on through the imaging system, and eventually form the image. All other electrons are blocked by the aperture (or scatter off the column walls). Similarly, HyperSpy integrates the total electron intensity of the PED pattern, falling within the chosen VA, and assigns a colour-scale tone to the DP's corresponding specimen area point. By running a loop over the full PED pattern stack, using the same aperture, and assigning to each pattern's corresponding specimen area a colour-scale tone, one obtains a virtual dark field (VDF) image. Similarly, using VA positionings on the 000-reflection, yields a virtual bright field image (VBF). Figure 3.4 shows the SPED data viewing, VA positioning and resulting VDF image formed.

3.3.2 Machine learning

More sophisticated data analysis included the use of 'machine learning' in order to identify the main 'component patterns' in the PED pattern stack, as well as their spatial localization, referred to as 'loading maps' [37]. The component patterns are repeatedly occurring DP-components in the pattern stack, calculated to originate from an unique phase orientation/area feature/etc. The loading maps are similar in appearance to VDF images, but obtained by an automated and objective approach, requiring little or no prior knowledge

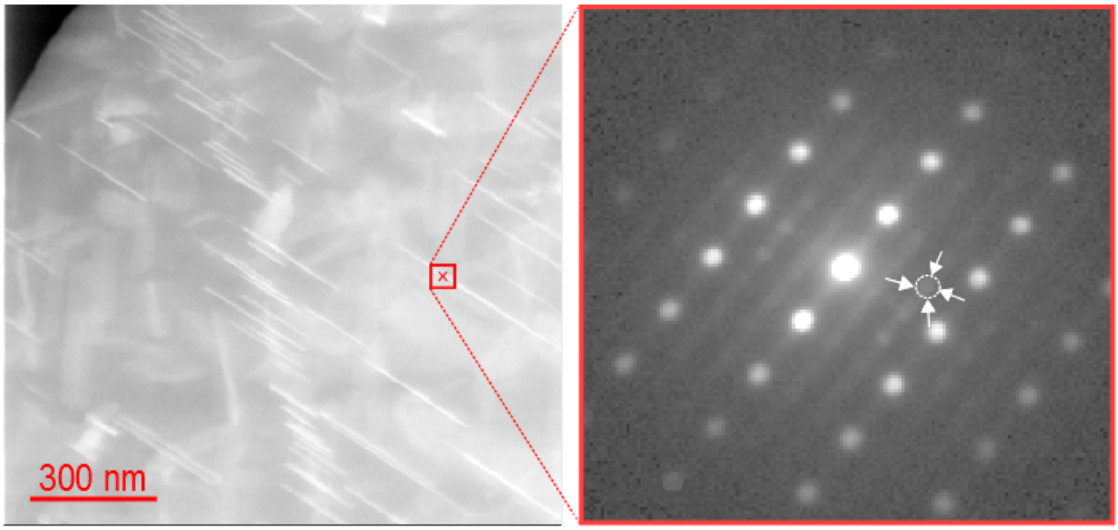

(a)

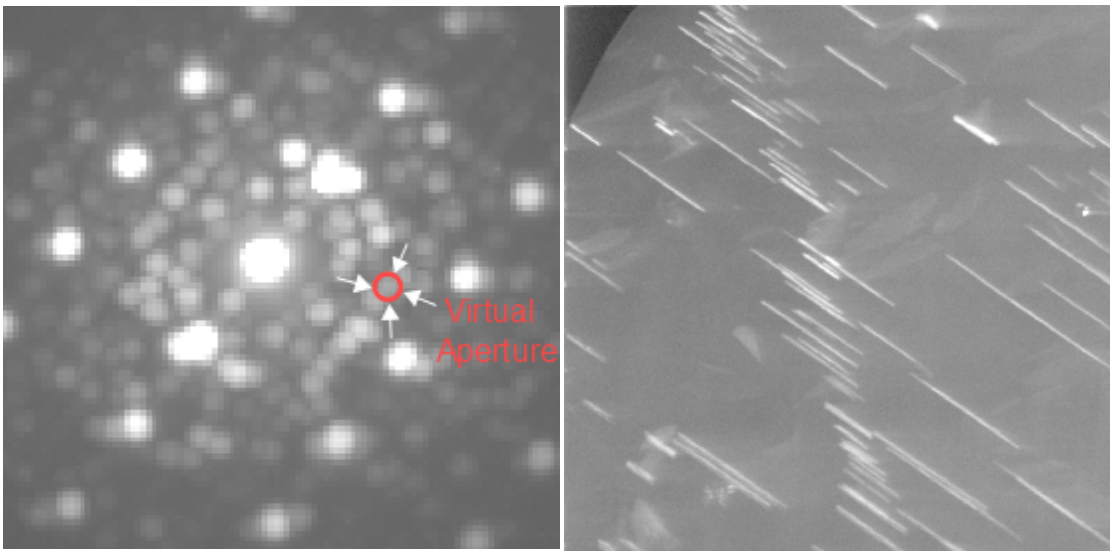

(b) (c)

Figure 3.4: SPED data viewer and VDF image formation procedure. (a) A ZA SPED data set comprising a PED pattern in each out of 300^2 pixels. The pattern from the marked data point is shown to the right with a highlighted reflection associated with the diffracting feature at this pixel point. (b) VA positioning in the summed PED pattern stack. The chosen reflection is associated with the diffracting feature seen marked in the right DP of (a). (c) Resulting VDF image from the VA placement in (b). This SPED data set is acquired from the $[112]_{Al}$ ZA of alloy CL. The scanned area is 1.35 μm^2, using 300^2 pixels.

of specimen microstructures. This opens the possibility of identifying features with unexpected crystallographic structure.

HyperSpy has several built-in component separation algorithms. In running principal component analysis (PCA), or blind source separation (BSS), one obtains a series of component patterns, with associated loading maps. PCA puts emphasis on variations across the data set, whereas BSS looks for repeating features in the data. Therefore, BSS was the main algorithm of choice.

It was found necessary to use cropped data sets prior to running the BSS algorithm, due to its intensive memory usage. The PED pattern stack was cropped as square sections using the area interior to the first Al reflections, see figure 3.5. This gave roughly a x10 reduction in data size.

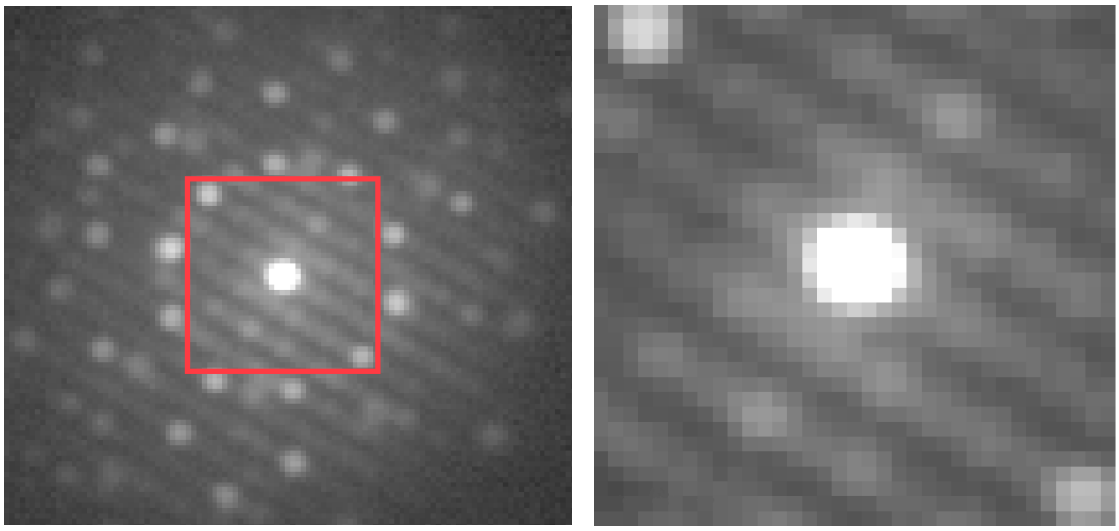

(a) (b)

Figure 3.5: Cropping of PED patterns prior to subsequent BSS and ASTAR indexing. The area interior to the first Al reflections is used. (a) PED pattern prior to cropping. (b) Resulting PED patterns after data cropping, and to be used in BSS and ASTAR indexing. This DP was recorded on an Al-Cu-(Mn,Fe) dispersoid in its high symmetry orientation, showing a very dense set of reflections due to the large unit cell.

3.3.3 ASTAR indexing

The ASTAR Index software [33] is an automated crystallographic indexing and orientation-/phase mapping tool. It obtains phase and orientation identification based on pattern matching between experimental PED patterns and simulated templates, referred to as 'template banks'. The template banks take as input the crystal structure atoms, positionings and space group symmetries, thus fully specifying the crystallographic nature

of the simulated structures. The bank is stored as projected sections of a kinematically simulated reciprocal space, using a specified angular precision. The software enables the formation of orienational maps, showing all orientations present in the scanned specimen area.

The matrix microstructures in the studied Al alloys are very complex, exhibiting numerous structures, often overlapping, with different orientational relationships. Obtaining overview orientational maps from the ZA SPED data was therefore not pursued, as initial results were time consuming and offered little additional insight. The focus was rather shifted towards the Al-Cu-(Mn,Fe) dispersoids (T-particles) present in the matrix, whose rotation-twinned substructures could result in interesting orientational mappings.

In order to map the orientations of the T-particle substructure, one needs to form a template bank taking as input the crystal structure of these particles. The underlying unit cell of the T-particle is large, most commonly reported as $Al_{20}Cu_2Mn_3$, i.e. 25 atoms, with Fe randomly taking the place of Mn-atoms. The complete crystallographic structure of the T-particles are not to be found in the scientific literature. However, [34] summarizes previous reliable findings to four proposed space groups. These all agree on an underlying orthorhombic unit cell. ASTAR indexing was found to give reliable reflection and orientation matching using the space group Bbmm, with $a = 24.1$ Å, $b = 12.5$ Å and $c = 7.8$ Å ($\alpha = \beta = \gamma = 90°$) [38]. With the purpose of identifying scanned area orientations present, the intensity of individual structure reflections are not crucial, and the full unit cell were specified to consist of Al-atoms only, as the individual positions of the different atoms in the unit cell is not known.

Prior to indexing the dispersoid SPED data, the PED pattern stack was cropped in a similar manner to that of BSS data pre-processing, see figure 3.5. Before indexing the cropped pattern stack, the full 'un-cropped' stack was used to correct for image distortions. Distortion correction is necessary as the PED patterns have been recorded using an external camera imaging a tilted fluorescent screen. Slight deviations from perfect perpendicular setups are unavoidable, hence the recorded patterns will be prone to slight distortions. The strong Al reflections were used for the correction procedure provided by the ASTAR Index software. Once the Al reflections were satisfactory matched to the Al template bank, the cropped pattern stack was opened, retaining the image correction parameters. Indexing the cropped dispersoid pattern stacks, which usually amounted to 200-300 MB of data, required some 10-30 min time on the stated computer.

3.3.4 Image processing

Many of the obtained virtual and conventional images presented in this thesis are not presented in their as-obtained form. Most commonly, they are further processed in order to best highlight the features of interest. The image processing was applied using the Digital Micrograph [39] and HyperSpy software. Basic processing involves the adjustments of gamma, brightness and contrast levels.

Each virtual image is obtained using individual VA positions. However, DPs are always symmetrical in nature. Therefore, as a means of signal amplification, individual

images obtained by symmetrically placed VAs were summed using simple Python scripts. Processing beyond the basic options involved filtering. Weak signals were enhanced using linear 'sharpness' and subsequent 'smoothing'-filters. In figure 3.6 it is shown an example of an as-obtained VDF image next to the corresponding processed, as-presented image.

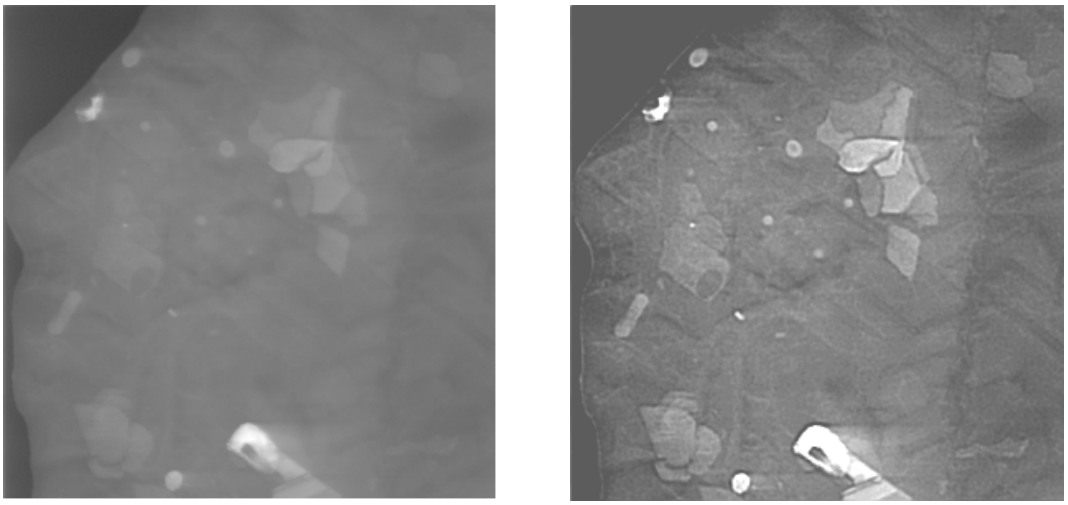

(a) (b)

Figure 3.6: (a) As-obtained VDF image of face-on $(111)_{Al}$ T1-precipitate plates viewed in the $[111]_{Al}$ ZA. (b) The image of (a) after image processing. Gamma, brightness and contrast levels have been adjusted, and a linear 'sharpness' and subsequent 'smoothing'-filter have been applied. These options have been applied by using the Digital Micrograph software.

3.4 DP Simulations

In order to identify the different components of the rich diffraction patterns recorded in the (S)PED data, DP simulations running the CrystalKit software [40] was used. CrystalKit is a crystallographical simulation software. By specifying a crystal structure; including its basis, symmetries, space group etc., the software allows for an interactive 3D view of the structure. One can obtain real space information about the crystal structure, such as interplanar spacings (both real and projected), angles between crystal directions, ZA orientations, etc.

Regarding case in interest, it can also run kinematical diffraction simulations at different HTs and camera lengths. Most importantly, it can simulate matrix-precipitate diffraction by specifying a crystal structure A (e.g. the Al fcc matrix) and a crystal structure B (e.g. the θ'-precipitate). This necessitates the precipitate crystal structures and orientational relationships relative to the surrounding Al matrix to be known. The following figures and tables display the crystal structures used for DP simulations in the 2xxx series Al alloys studied.

Al: Aluminium is a fcc structure with lattice parameters $a = b = c = 4.04$ Å, and unit cell angles $\alpha = \beta = \gamma = 90°$. It is of space group #225 denoted Fm$\bar{3}$m.

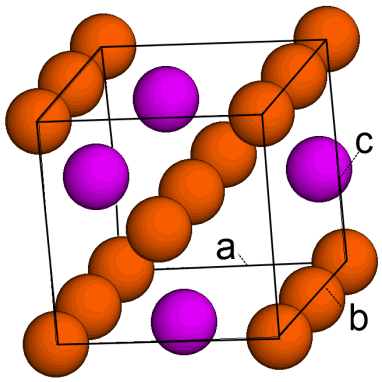

Figure 3.7: The tetragonal unit cell of the θ'-precipitate. **Orange:** Al-atoms. **Purple:** Cu-atoms. The model was created in CrystalKit.

Table 3.3: Atomic basis coordinates in the θ'-precipitate. The coordinates are fractional with respect to a tetragonal unit cell.

Site	x	y	z
Al	0.0	0.0	0.0
Al	0.0	0.0	1/2
Cu	0.0	1/2	1/4

***θ'*:** The θ'-precipitate (Al_2Cu) exhibits the well-established Silcock structure [41]. It is tetragonal with lattice parameters $a = b = 4.04$ Å and $c = 5.80$ Å ($\alpha = \beta = \gamma = 90°$). It is of space group #119 denoted I$\bar{4}$m2. The θ'-precipitate forms as octagonal (sometimes rectangular) plates on $\{001\}_{Al}$ planes. The unit cell is displayed in figure 3.7 and the basis coordinates are shown in table 3.3. The orientational relationship of the θ'-precipitate relative to the Al matrix is specified as $(001)_{\theta'} \| (001)_{Al}$, $\langle 100 \rangle_{\theta'} \| \langle 100 \rangle_{Al}$.

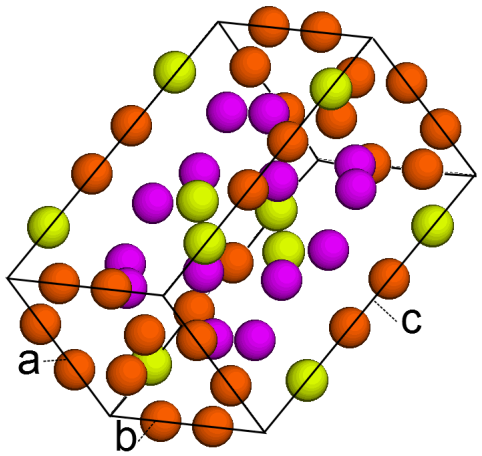

Figure 3.8: The hexagonal unit cell of the T1-precipitate. **Orange:** Al-atoms. **Purple:** Cu-atoms. **Yellow:** Li-atoms. The model was created in CrystalKit.

Table 3.4: Atomic basis coordinates in the T1-precipitate. The coordinates are fractional with respect to a hexagonal unit cell.

Site	x	y	z
Al-c	1/3	0.0	0.0
Al(1)	0.0	0.0	0.4062
Al-Cu(1)	2/3	1/3	0.1612
Al-Cu(2)	1/2	0	0.3237
Li(1)	0.0	0.0	0.1993
Li(2)	1/3	2/3	1/2

T1: The T1-precipitate structure (Al-Cu-Li containing) has for a long time been a challenge to unveil, but [3] seems to be the most promising. The structure is hexagonal with lattice parameters $a = b = 4.96$ Å and $c = 14.18$ Å ($\alpha = \beta = 90°$ and $\gamma = 120°$). It is of space group #191 denoted P6/mmm. The T1-precipitate forms as hexagonal plates on $\{111\}_{\mathrm{Al}}$ planes. The unit cell is displayed in figure 3.8 and the basis coordinates are shown in table 3.4. The orientational relationship of the T1-precipitate relative to the Al matrix is specified as $(001)_{\mathrm{T1}} \| (111)_{\mathrm{Al}}$, $\langle 110 \rangle_{\mathrm{T1}} \| \langle 112 \rangle_{\mathrm{Al}}$.

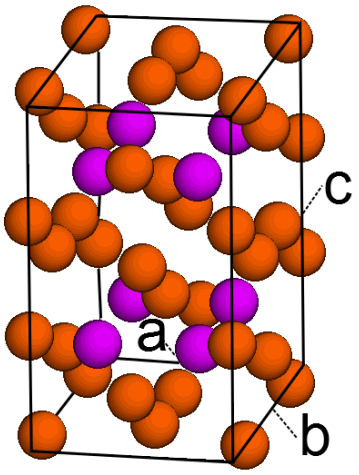

Figure 3.9: The orthorhombic unit cell of the Ω-precipitate. **Orange:** Al-atoms. **Purple:** Cu-atoms. The model was created in CrystalKit.

Table 3.5: Atomic basis coordinates in the Ω-precipitate. The coordinates are fractional with respect to an orthorhombic unit cell.

Site	x	y	z
Al(1)	0.0	1/3	0.0
Al(2)	0.0	0.0	1/6
Cu	1/4	1/4	1/4

Ω : The Ω-precipitate (Al_2Cu) structure has an orthorhombic unit cell with lattice parameters $a = 4.96$ Å , $b = 8.56$ Å and $c = 8.48$ Å ($\alpha = \beta = \gamma = 90°$) [2]. It is of space group #69 denoted Fmmm. The Ω-precipitate forms as hexagonal plates on $\{111\}_{\mathrm{Al}}$ planes. The unit cell is displayed in figure 3.9 and the basis coordinates are shown in table 3.5. The orientational relationship of the Ω-precipitate relative to the Al matrix is specified as $(001)_{\Omega} \| (111)_{\mathrm{Al}}$, $\langle 010 \rangle_{\Omega} \| \langle 110 \rangle_{\mathrm{Al}}$.

S: The S-precipitate structure (Al_2CuMg) has an orthorhombic unit cell with lattice parameters $a = 4.00$ Å , $b = 9.23$ Å and $c = 7.14$ Å ($\alpha = \beta = \gamma = 90°$) [42]. It is of space group #63 denoted Cmcm. The S-precipitate forms as laths elongated along the $\langle 001 \rangle_{\mathrm{Al}}$ directions. The unit cell is displayed in figure 3.10 and the basis coordinates are shown in table 3.6. The orientational relationship of the S-precipitate relative to the Al matrix is specified as $(100)_{\mathrm{S}} \| (001)_{\mathrm{Al}}$, $\langle 010 \rangle_{\mathrm{S}} \| \langle 210 \rangle_{\mathrm{Al}}$.

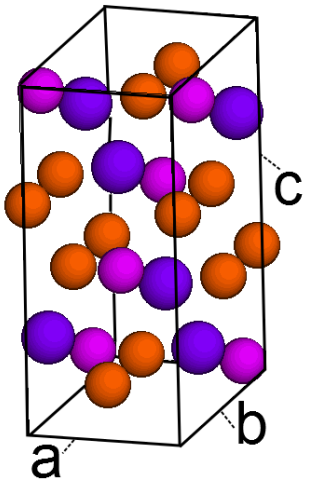

Figure 3.10: The orthorhombic unit cell of the S-precipitate. **Orange:** Al-atoms. **Purple:** Cu-atoms. **Blue:** Mg-atoms. The model was created in CrystalKit.

Table 3.6: Atomic basis coordinates in the S-precipitate. The coordinates are fractional with respect to an orthorhombic unit cell.

Site	x	y	z
Al	0.0	0.356	0.555
Mg	0.0	0.065	0.750
Cu	0.0	0.780	0.750

All DPs were simulated using a HT of 200 kV and a camera length of 150 cm. Depending on the orientational relationship between the Al matrix and the precipitate structure, a different number of unique diffracting orientational relationships will be present in the recorded DPs. As an example this will be discussed for the T1-matrix relation $(001)_{T1} \| (111)_{Al}$, $\langle 110 \rangle_{T1} \| \langle 112 \rangle_{Al}$.

The $(111)_{Al}$-plane exhibits hexagonal symmetry. This is also the case for the $(001)_{T1}$ plane, i.e. the **a**-**b**-plane seen in figure 3.8, in the hexagonal unit cell of the T1-phase. This means that there is one unique symmetry axis, namely the one crossing the center of the **a**-**b**-plane running in parallel to the **c**-axis. The number of possible orientations of this axis, and correspondingly the number of non-equivalent DPs, will most likely coincide with the number of $\{111\}_{Al}$-planes, which is four. The number increases for the Ω-precipitate. It also forms on the $\{111\}_{Al}$-planes, but has an underlying orthorhombic unit cell, which is less symmetric with respect to this plane.

The different possible orientations adhering to the stated orientational relationship were simulated individually in the matrix-precipitate DPs. The procedure was repeated for all the stated 2xxx series Al alloy precipitates for several major ZAs including $[001]_{Al}$, $[111]_{Al}$, $[112]_{Al}$ and $[013]_{Al}$. The individual DPs were subsequently overlaid giving the total DP of all possible orientations in the chosen ZA. Finally, the total individual matrix-precipitate DPs were combined two and two; θ' and T1 as coexisting in the CL alloy, and Ω and S as coexisting in the MCA alloy.

Chapter 4

Results

First presented in this chapter are several simulated DPs of low-order Al ZAs containing the aforementioned T1-, θ'-, Ω- and S-precipitates. These are shown together with the total summed PED pattern stacks recorded near the same ZAs.

For each ZA, it is also shown how the simulated DPs were used to identify the different reflections of the recorded PED patterns, and how the VA positionings used in the subsequent section were chosen.

Then, by the use of these indicated VAs, several virtual images highlighting individual precipitates as inclined relative to the corresponding ZAs are presented. The individual VDF images are then combined in constructed RGB (Red-Green-Blue) images. The obtained results are presented systematically for each ZA of interest separately.

Following, it is shown several TEM images obtained using conventional imaging techniques including HRTEM, DF- and BFTEM, as well as HAADF- and BF-STEM. These are presented together with formed VDF- and VBF images.

The following section presents HRTEM images, orientational mappings and misorientation plots on Al-Cu-(Mn,Fe) dispersoids (T-particles).

The final section of this chapter presents applied 'machine learning' results of blind source separation (BSS) acting on the $[001]_{Al}$ ZA data set of alloy MCA. Here, it is shown loading maps together with their corresponding component patterns, as extracted from the PED pattern stack.

Results from additional ZAs are shown in Appendix A.

4.1 Simulated and Recorded DPs

The structure inputs for diffraction pattern simulations are explained in the experimental methods chapter. In the following, simulated and recorded DPs are shown systematically for each ZA of interest, highlighted in the figure captions. The results are shown first for the CL alloy, followed by the MCA alloy.

Figure 4.1 shows the total matrix-precipitate DP for T1- and θ'-precipitates in the $[001]_{Al}$ ZA (a), as well as the total summed PED pattern stack near the same ZA (b).

Figures 4.2 and 4.3 show the individual matrix-precipitate DPs for T1- and θ'-precipitates

in the $[001]_{Al}$ ZA, including all orientational relationships between the precipitates and the surrounding matrix.

Figures 4.4 and 4.5 show simulated and recorded DPs in the $[111]_{Al}$ ZA in alloy CL, as well as the VA positionings used in the subsequent section.

Figures 4.6 through 4.9 show simulated and recorded DPs in the $[001]_{Al}$ and $[013]_{Al}$ ZAs in alloy MCA, as well as the VA positionings used in the subsequent section. These matrix-precipitate DP simulations include S- and Ω-precipitates as representative of the OA condition in alloy MCA.

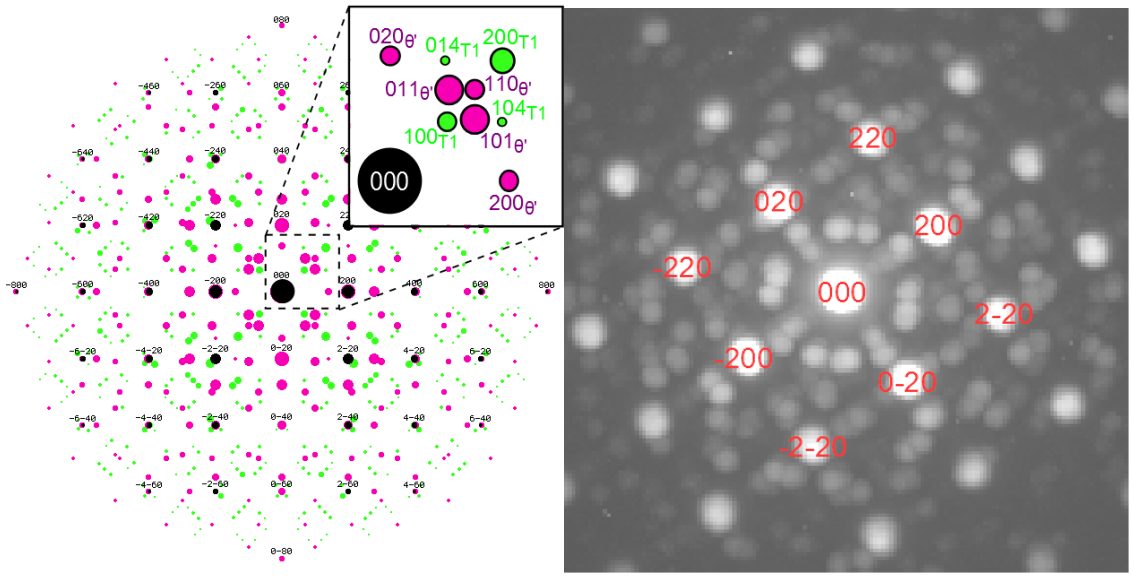

(a) (b)

Figure 4.1: (a) Total kinematically simulated DP in the $[001]_{Al}$ ZA containing θ'- and T1-precipitates. Al-, θ'- and T1-reflections are shown in black, pink and green respectively. The insert shows indexed precipitate reflections of the highlighted DP quadrant. Some reflections overlap, and in this case the colour will correspond to that of the precipitate. (b) Sum of all DPs recorded near the $[001]_{Al}$ ZA in the CL alloy. Inner Al reflections are shown indexed.

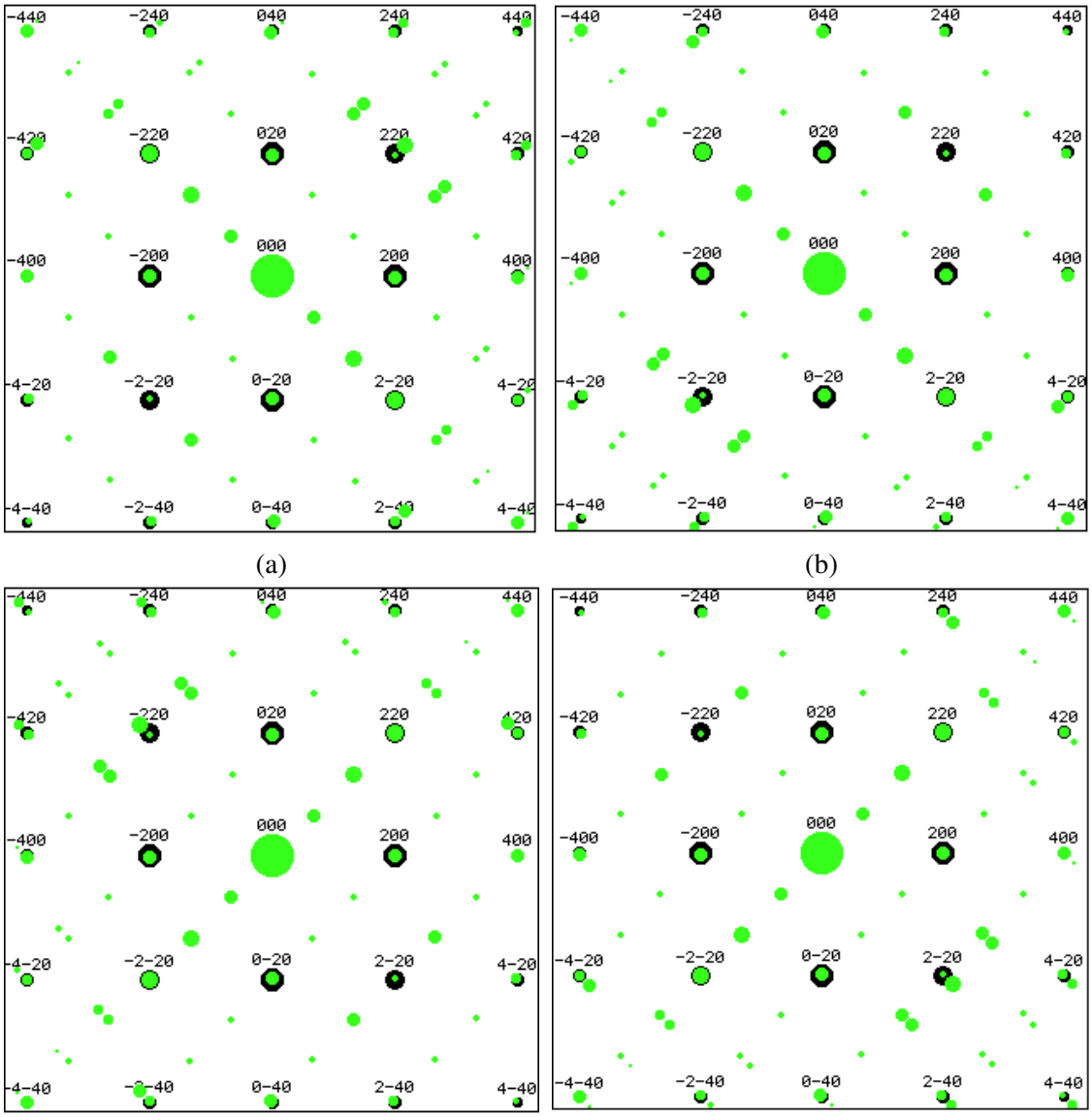

Figure 4.2: (a) through (d): The four unique T1-precipitate kinematical DPs in the $[001]_{Al}$ ZA, as determined by the matrix-precipitate orientational relationship. The main symmetry axis of the T1 hexagonal unit cell is oriented along $[111]_{Al}$, $[11\text{-}1]_{Al}$, $[\text{-}111]_{Al}$ and $[1\text{-}11]_{Al}$ respectively. Al reflections are shown in black with indicies, and the T1-reflections are shown in green.

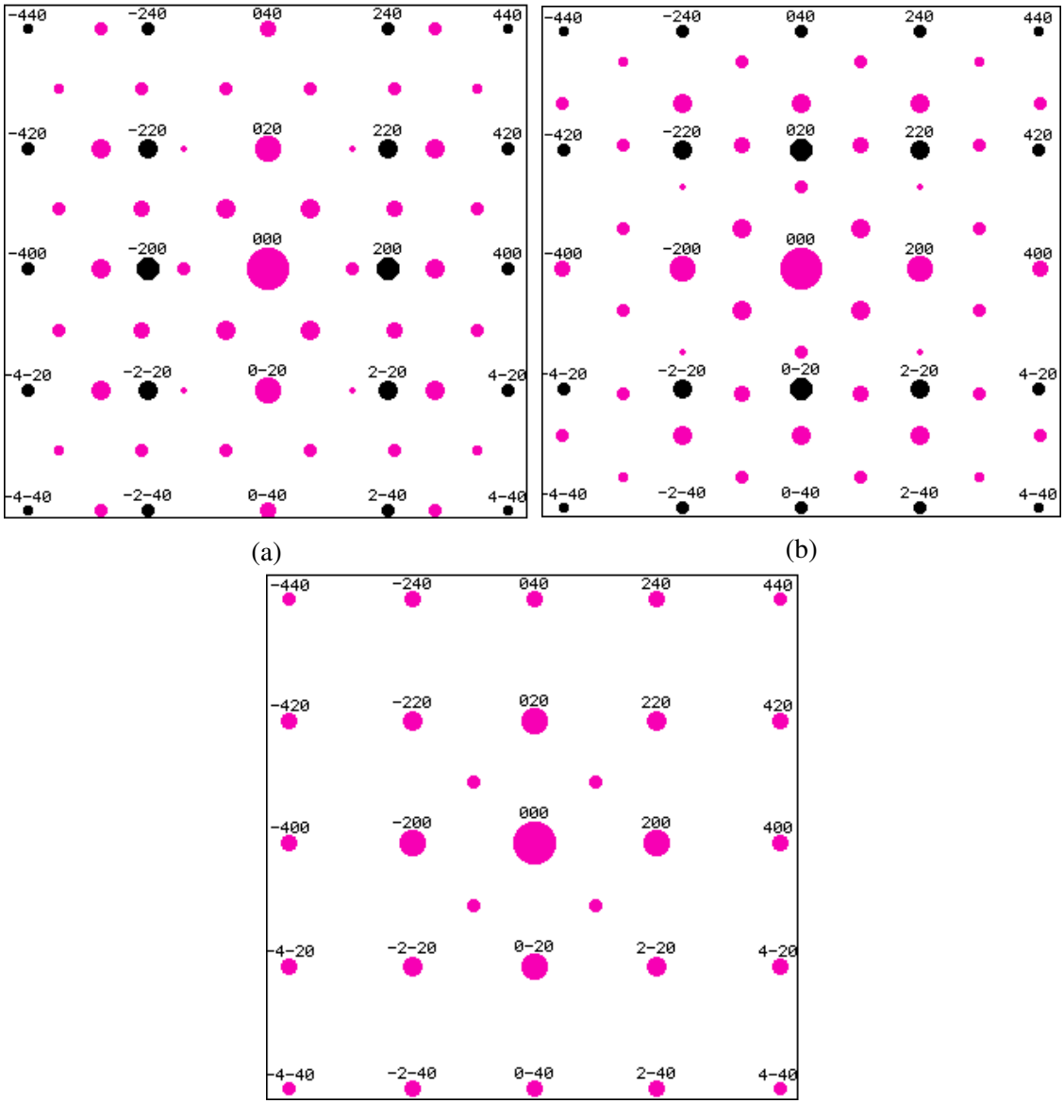

Figure 4.3: (a) through (c): The three unique θ'-precipitate kinematical DPs in the $[001]_{Al}$ ZA, as determined by the matrix-precipitate orientational relationship. The main symmetry axis of the θ' tetragonal unit cell is oriented along $[100]_{Al}$, $[010]_{Al}$ and $[001]_{Al}$ respectively. Al reflections are shown in black with indicies, and the θ'-reflections are shown in pink.

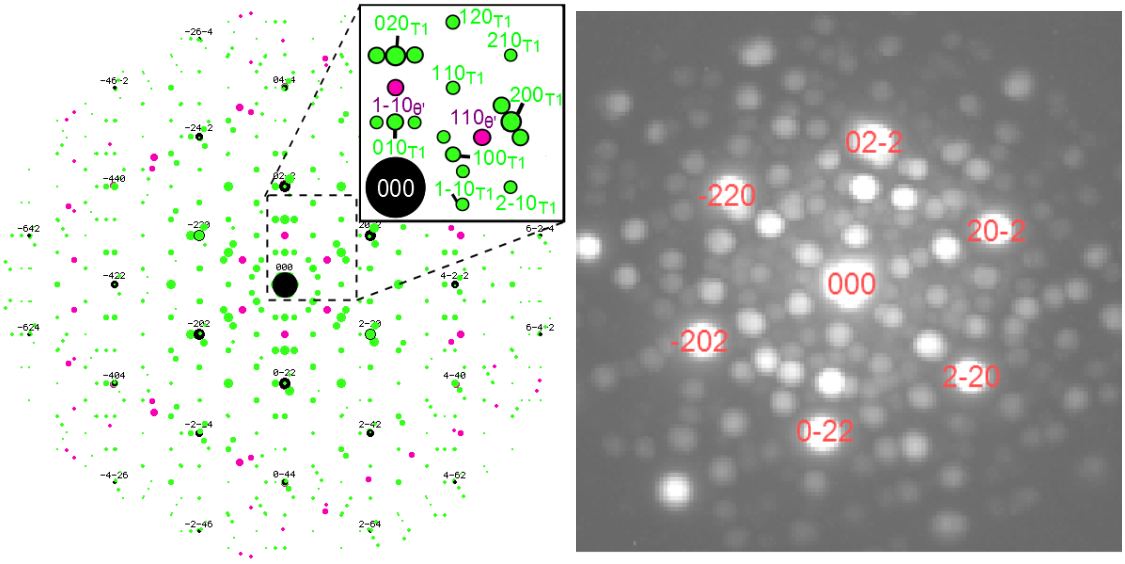

(a) (b)

Figure 4.4: (a) Total kinematic matrix-precipitate DP, with indexed insert, formed using an Al matrix (black reflections), T1- (green) and θ'- (pink) precipitates in the $[111]_{Al}$ ZA. Some reflections overlap, and in this case the colour will correspond to that of the precipitate. (b) Summed PED pattern stack recorded near the $[111]_{Al}$ ZA in alloy CL.

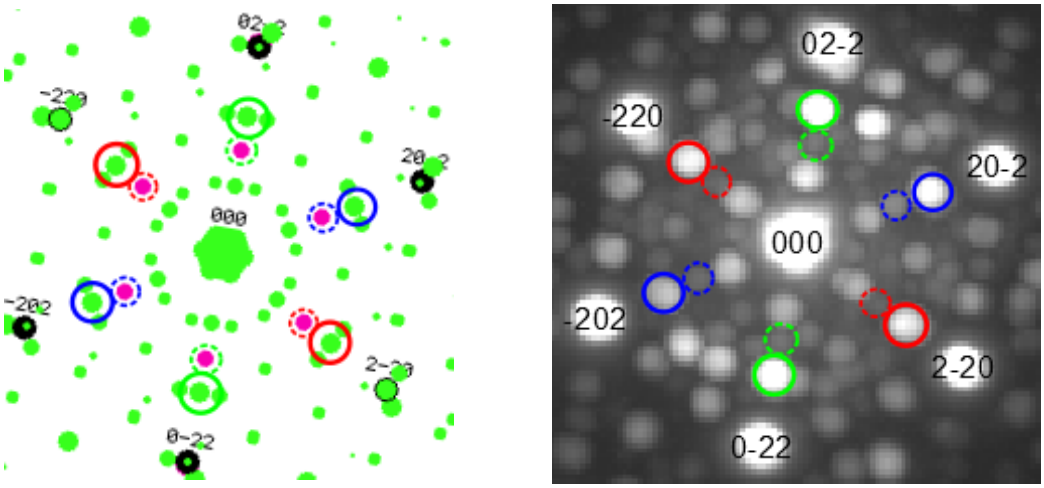

(a) (b)

Figure 4.5: Placement of VAs in the (a) simulated matrix-precipitate DP and (b) summed PED pattern stack of figure 4.4, recorded in the $[111]_{Al}$ ZA, indicated by coloured circles. The RGB colouring scheme corresponds with that of the individual precipitate orientations of figure 4.16 (b) and (c), using the filled and dashed circles respectively.

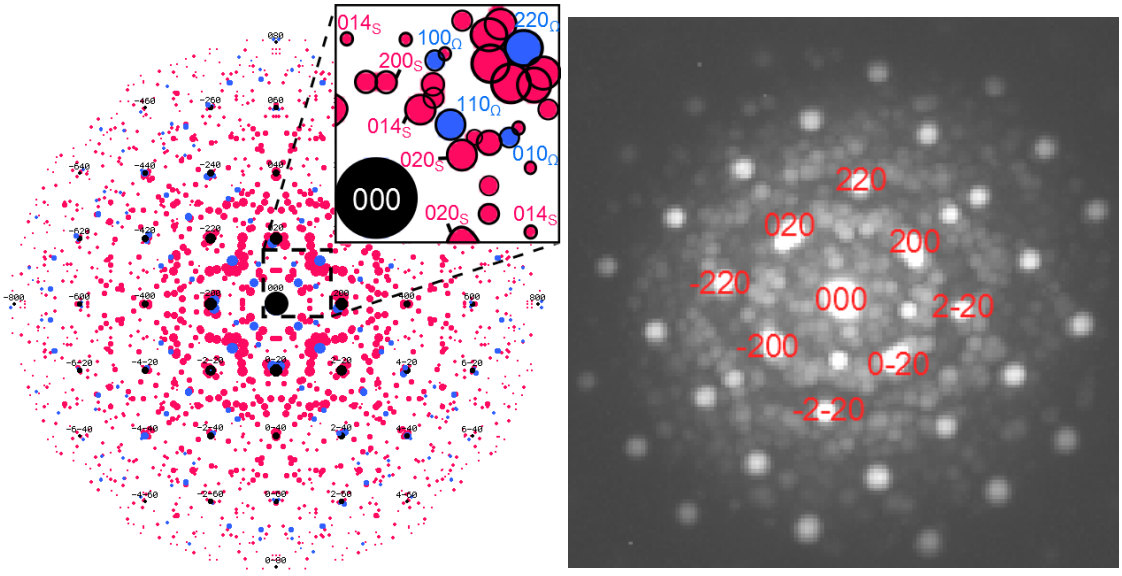

(a) (b)

Figure 4.6: (a) Total kinematic matrix-precipitate DP, with indexed insert, formed using an Al matrix (black reflections), Ω- (blue) and S- (red) precipitates in the $[001]_{Al}$ ZA. Some reflections overlap, and in this case the colour will correspond to that of the precipitate. (b) Summed PED pattern stack recorded near the $[001]_{Al}$ ZA in alloy MCA.

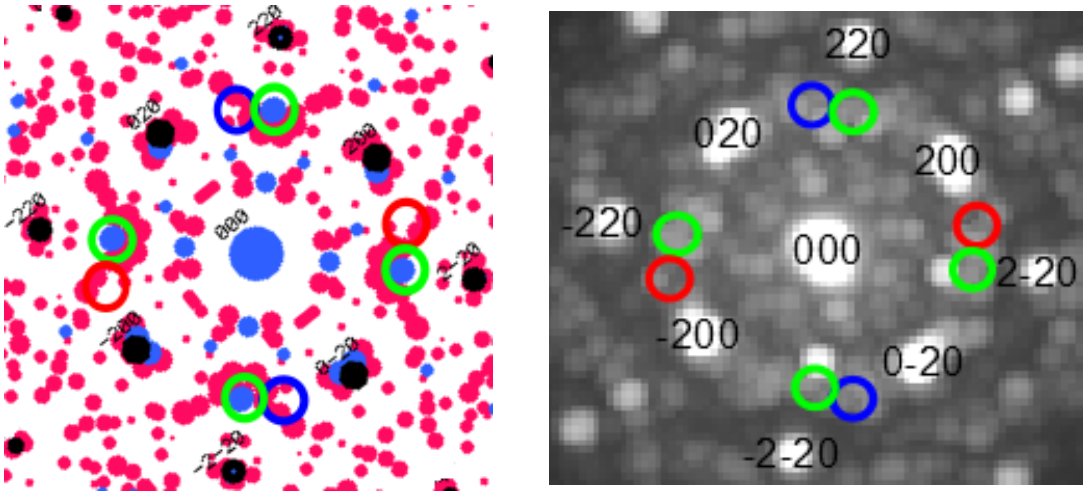

(a) (b)

Figure 4.7: Placement of VAs in the (a) matrix-precipitate DP and (b) summed PED pattern stack of figure 4.6, recorded in the $[001]_{Al}$ ZA, indicated by coloured circles. The RGB colouring scheme corresponds with that of the individual precipitate orientations of figure 4.16 (d).

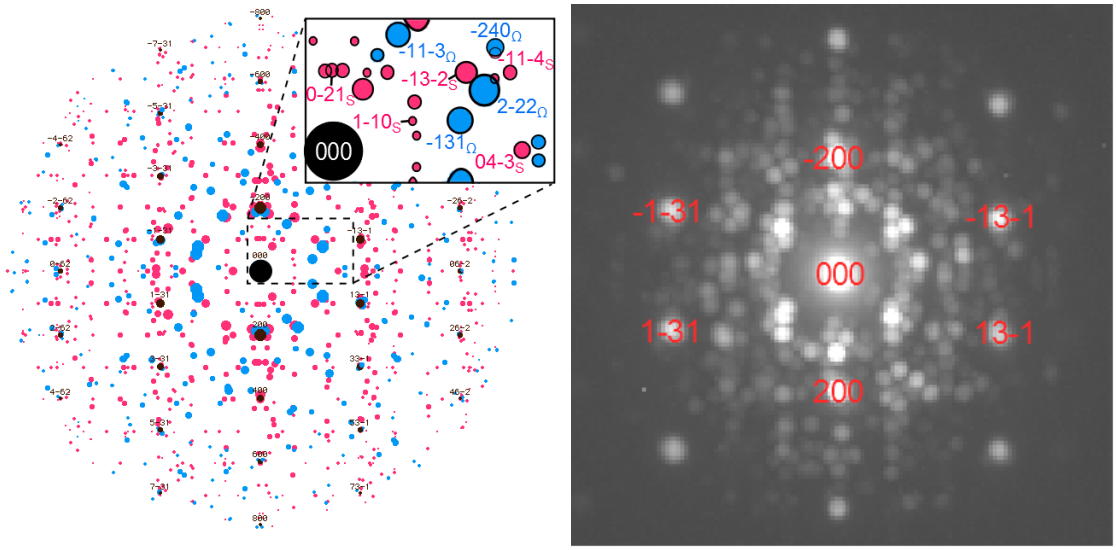

(a) (b)

Figure 4.8: (a) Total kinematic matrix-precipitate DP, with indexed insert, formed using an Al matrix (black reflections), Ω- (blue) and S- (red) precipitates in the $[013]_{Al}$ ZA. Some reflections overlap, and in this case the colour will correspond to that of the precipitate. (b) Summed PED pattern stack recorded near the $[013]_{Al}$ ZA in alloy MCA.

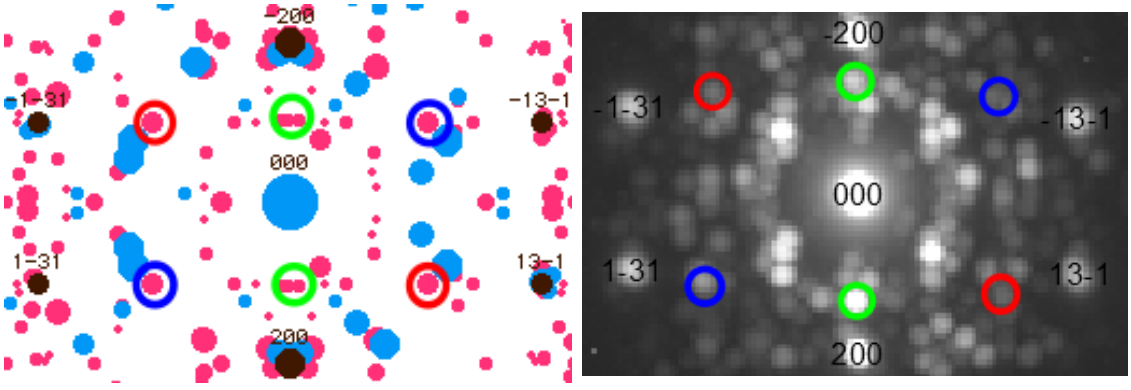

(a) (b)

Figure 4.9: Placement of VAs in the (a) matrix-precipitate DP and (b) summed PED pattern stack of figure 4.8, recorded in the $[013]_{Al}$ ZA, indicated by coloured circles. The RGB colouring scheme corresponds with that of the individual precipitate orientations of figure 4.16 (e).

4.2 Virtual Images

The full data processing for obtaining virtual images of identified reflections, corresponding to specific expected phases present, is shown schematically in figure 4.10. Figures 4.11 through 4.15 show virtual images of the individual main precipitates as inclined relative to the respective Al ZAs highlighted in the figure captions. Figure 4.16 shows constructed RGB images of the preceding VDF images.

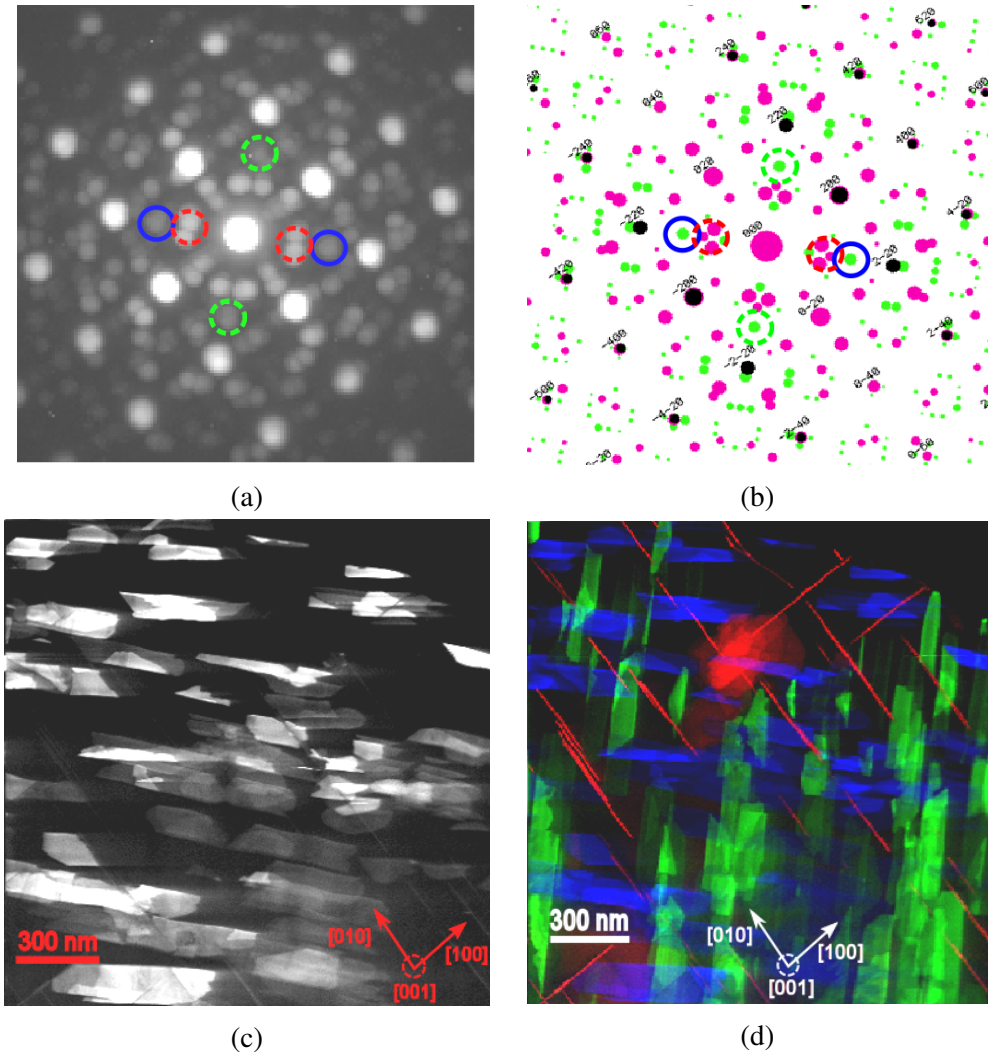

Figure 4.10: (a) Sum of all DPs recorded near the $[001]_{Al}$ ZA in the CL alloy. (b) Simulated matrix-precipitate DP using an Al matrix (black reflections), T1- (green) and θ'- (pink) precipitates in the $[001]_{Al}$ ZA. Coloured circles indicate VAs used in forming VDF images of precipitates of corresponding colouring in (d). (c) VDF image of T1-precipitates oriented horizontally, formed using the blue VAs in (a). (d) RGB image constructed from individual VDF images of the horizontal T1-precipitates (blue), vertical T1-precipitates (green) and θ'-precipitates (red).

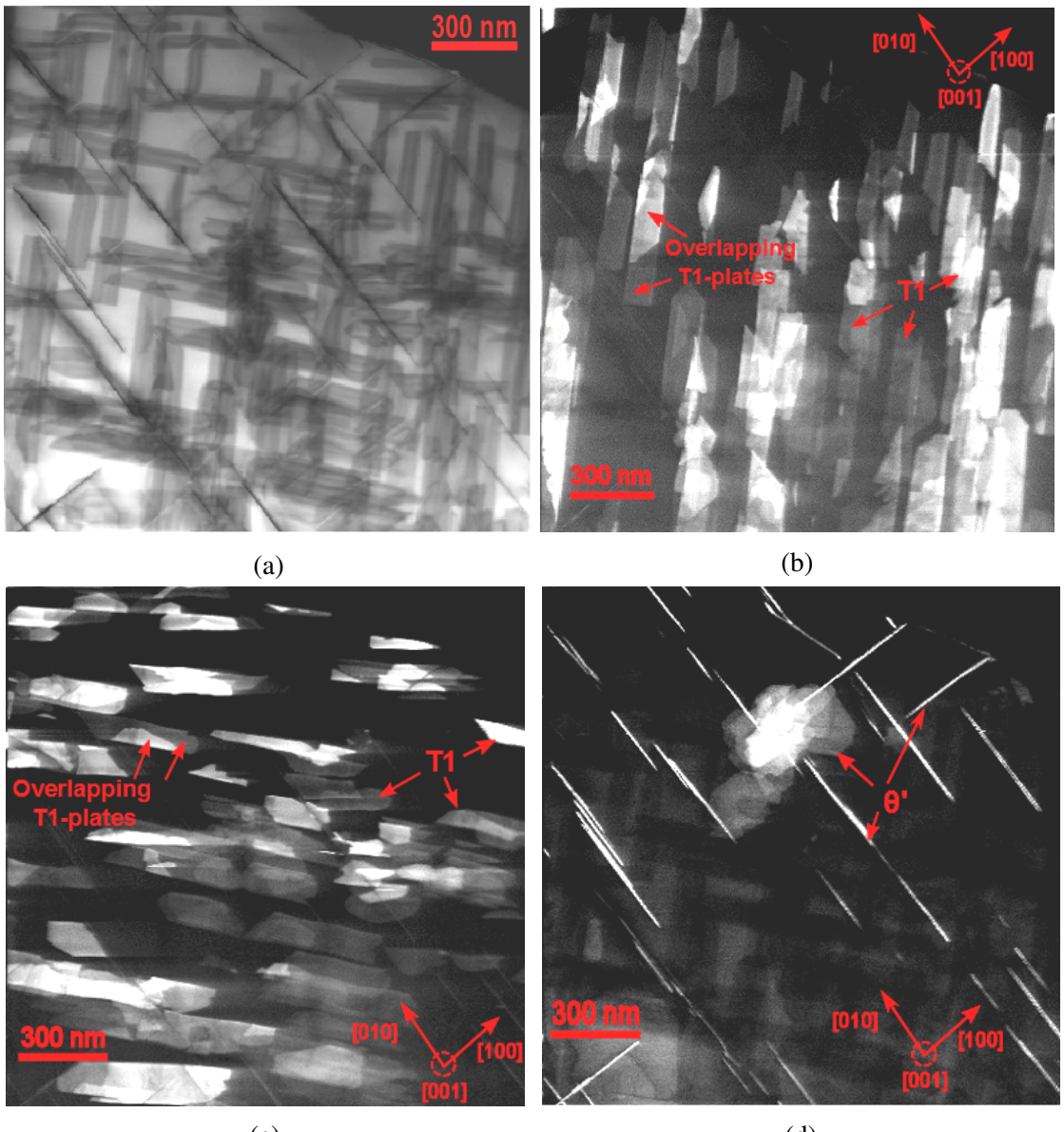

Figure 4.11: VBF (a) and VDF (b-d) images obtained near the $[001]_{Al}$ ZA in the CL alloy, obtained by the procedure of figure 4.10, which shows the same area data set. (a) Scanned specimen area. (b) $(1\text{-}11)_{Al}$ and $(\text{-}111)_{Al}$ T1-precipitate plates. (c) $(111)_{Al}$ and $(11\text{-}1)_{Al}$ T1-precipitate plates. (d) The three different orientations of the θ'-precipitate forming on $\{001\}_{Al}$. The scanned area is 1.80 μm^2, using 400^2 pixels.

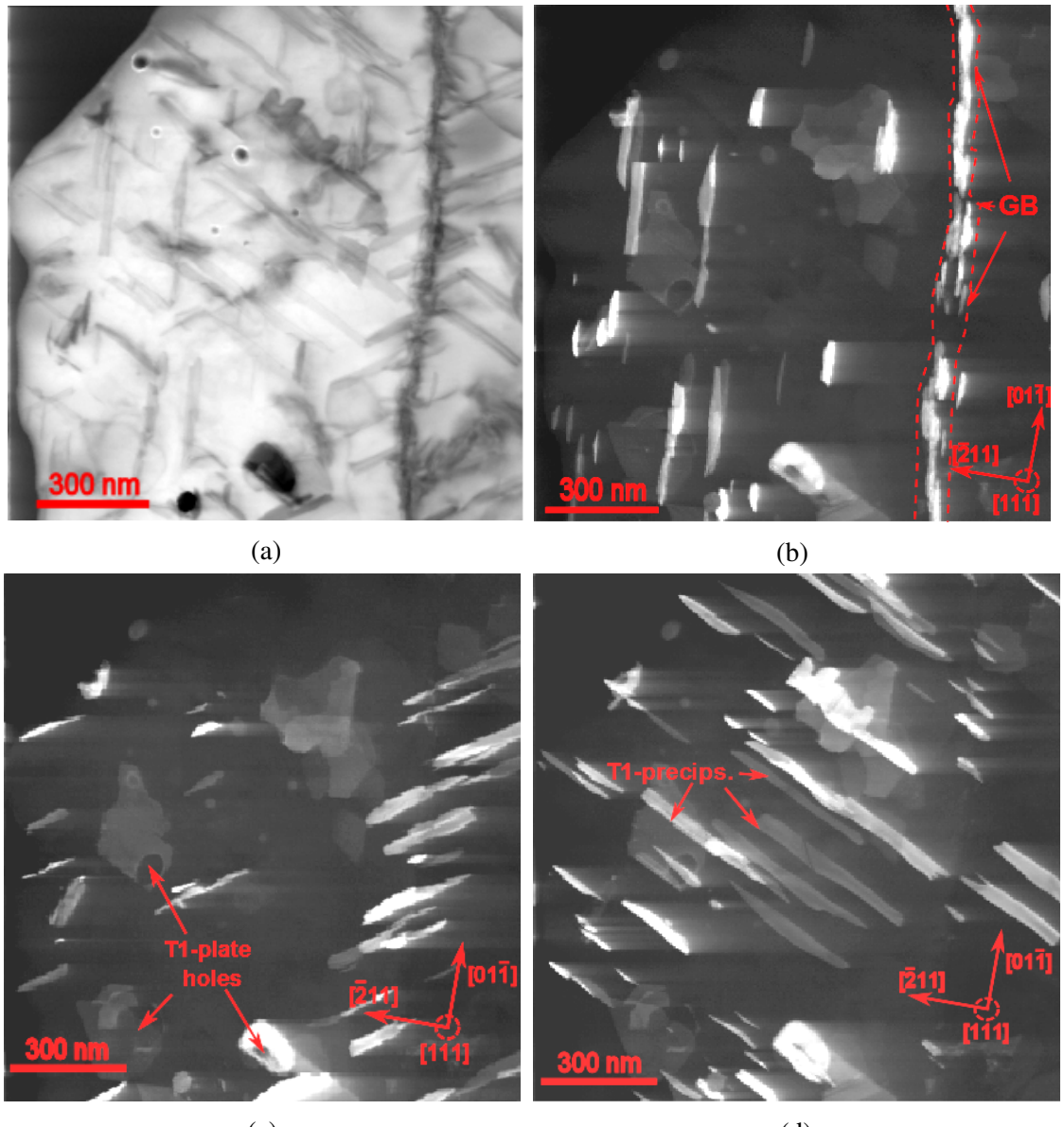

Figure 4.12: VBF (a) and VDF (b-d) images of T1-precipitate plates oriented in three out of four unique directions near the $[111]_{Al}$ ZA in the CL alloy. (a) Scanned specimen area. (b) $(11\text{-}1)_{Al}$ T1-precipitate plates. (c) $(\text{-}111)_{Al}$ T1-precipitate plates. (d) $(1\text{-}11)_{Al}$ T1-precipitate plates. Also visible in (b) through (d): T1-precipitates viewed face-on. The scanned area is 1.35 μm^2, using 300^2 pixels.

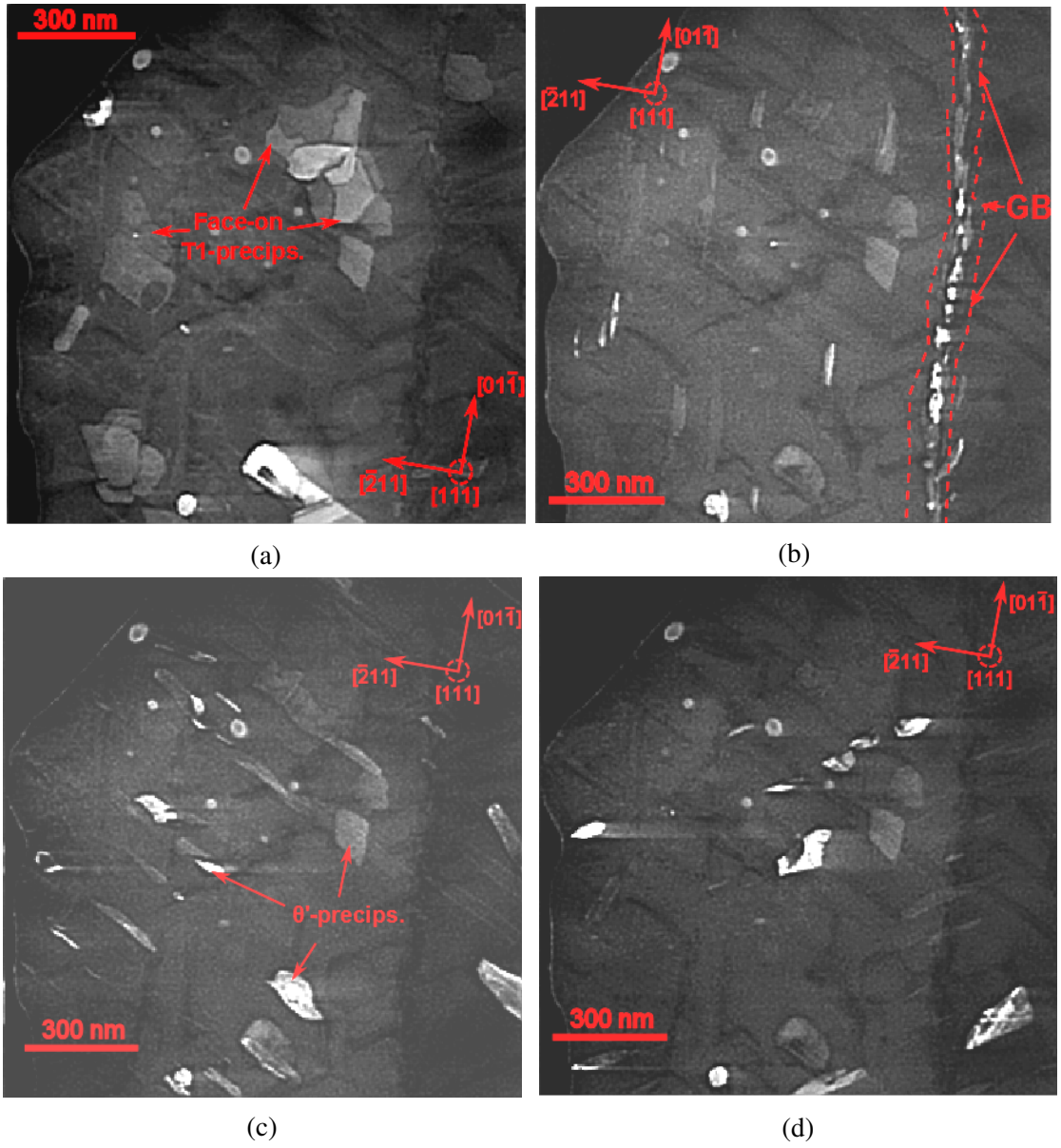

Figure 4.13: VDF images of T1-precipitates viewed face-on, and θ'-precipitate plates oriented in the three unique directions near the $[111]_{Al}$ ZA in alloy CL. (a) $(111)_{Al}$ T1-precipitate plates. (b) $(100)_{Al}$ θ'-precipitate plates. (c) $(010)_{Al}$ θ'-precipitate plates. (d) $(001)_{Al}$ θ'-precipitate plates. The scanned area is equal to that of figure 4.12.

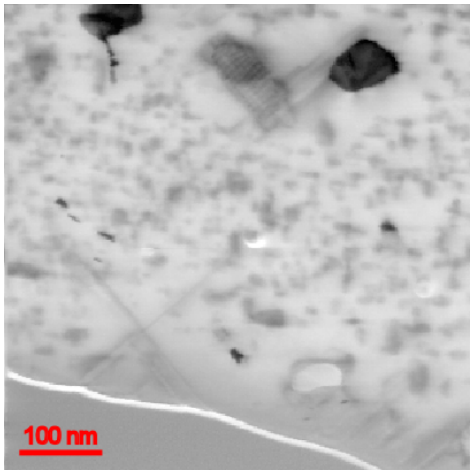

(a)

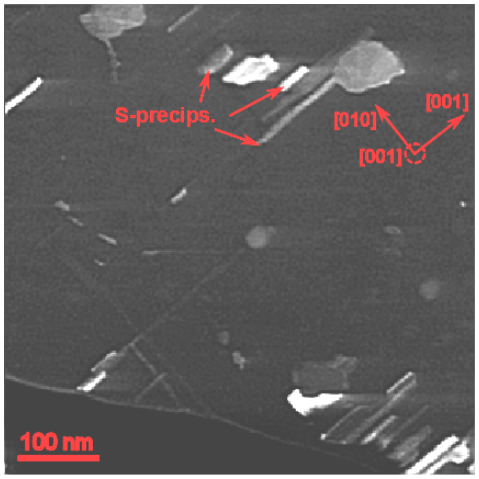

(b)

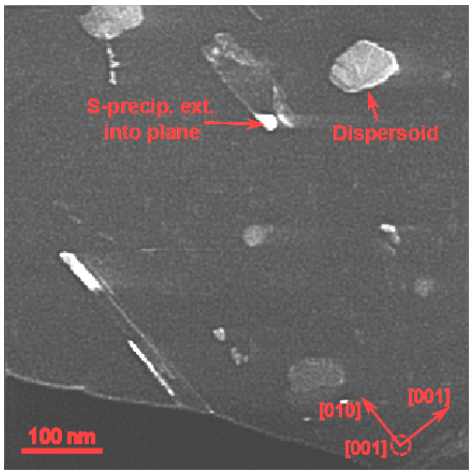

(c)

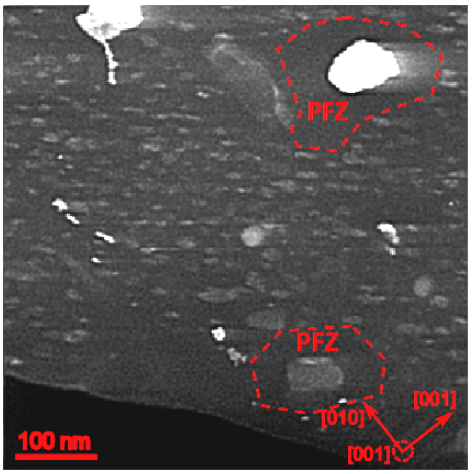

(d)

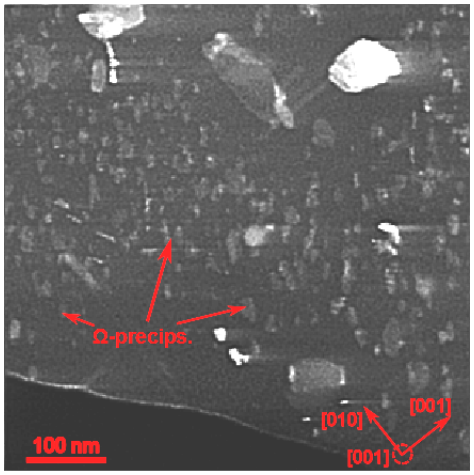

(e)

Figure 4.14: VBF (a) and VDF (b-e) images of S- and Ω-precipitates near the $[001]_{Al}$ ZA in the MCA alloy. (a) Scanned specimen area. (b) Different orientations of S-precipitate laths elongated along $[100]_{Al}$. (c) Different orientations of S-precipitate laths elongated along $[010]_{Al}$. (d) Different orientations of an Ω-precipitate plate set oriented horizontally. (e) Different orientations of an Ω-precipitate plate set oriented vertically. The scanned area is 576 nm^2, using 300^2 pixels.

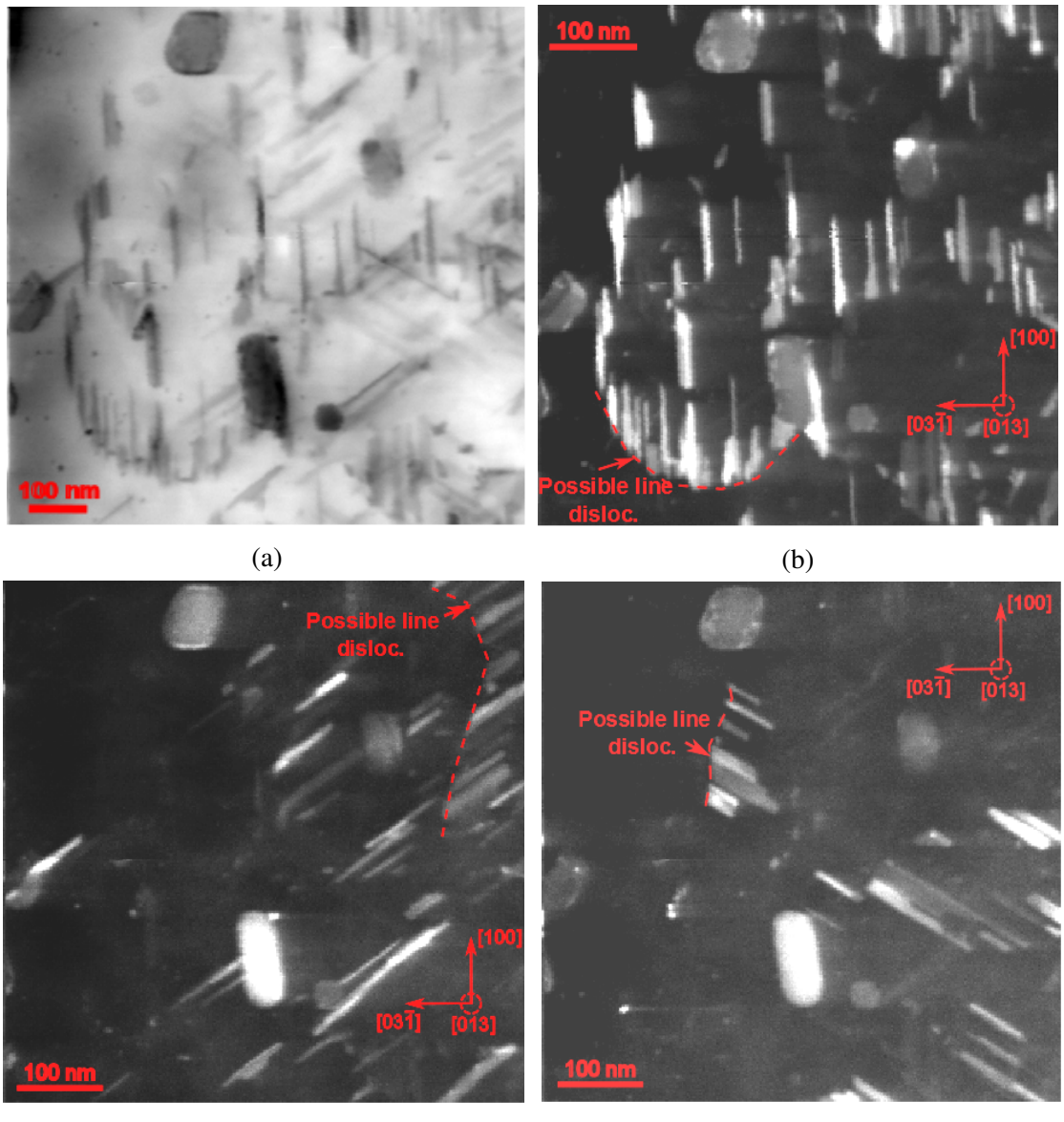

Figure 4.15: VBF (a) and VDF (b-d) images of S-precipitate laths elongated in three unique directions near the $[013]_{Al}$ ZA in the MCA alloy. (a) Scanned specimen area. (b) Different orientations of S-precipitate laths elongated along $[100]_{Al}$. (c) Different orientations of S-precipitate laths elongated along $[010]_{Al}$. (d) Different orientations of S-precipitate laths elongated along $[001]_{Al}$. The scanned area is 576 nm^2, using 300^2 pixels.

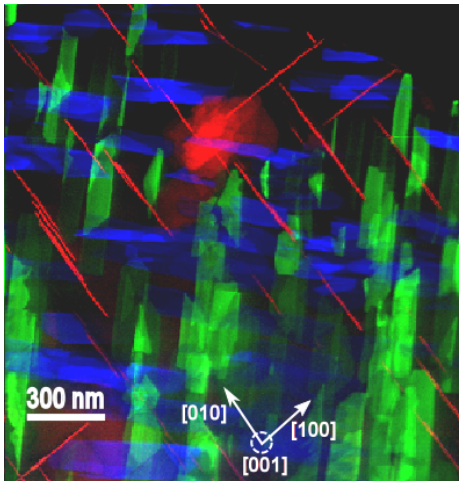

(a)

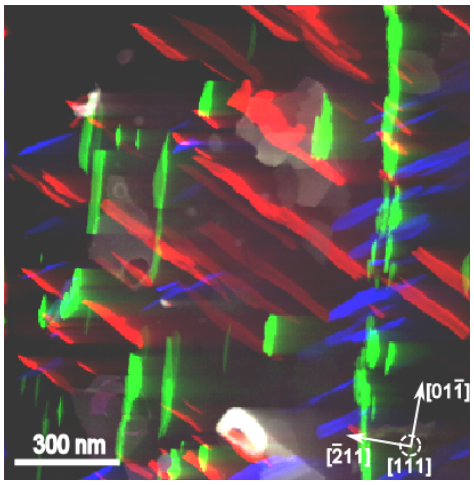

(b)

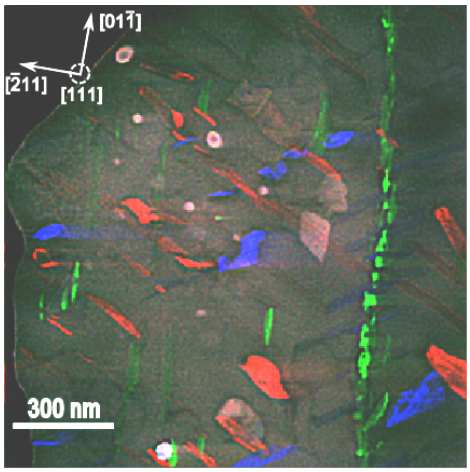

(c)

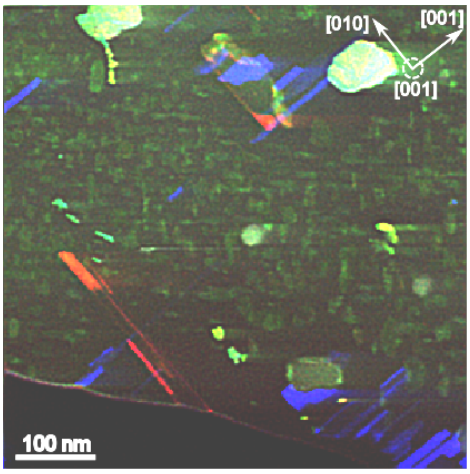

(d)

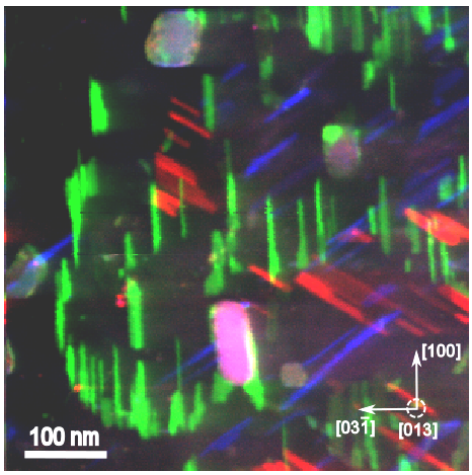

(e)

Figure 4.16: (a) through (e): RGB images highlighting the co-existing precipitates within the Al matrix near the $[001]_{Al}$ and $[111]_{Al}$ ZAs in alloy CL (a-c), and the $[001]_{Al}$ and $[013]_{Al}$ ZAs in alloy MCA (d-e). These are formed using the preceding VDF images, and the corresponding figure captions elaborate on which precipitates are observed. The VA positionings used are indicated in the figures of the preceding section, with VAs of corresponding colouring.

4.3 Virtual- and CTEM Images

This section presents several images taken using conventional imaging techniques, as a means of comparison to the preceding virtual images. The techniques include HRTEM, DF- and BFTEM, as well as HAADF- and BF-STEM. Figure 4.17 shows DFTEM images taken at the same specimen area as figure 4.11, with images (a) and (c) re-given here for convenience.

Figure 4.18 shows a constructed VBF and VDF image together with several conventional imaging techniques taken at the same specimen area.

Figure 4.19 shows a comparison between high-quality VDF and DFTEM images both in the $[111]_{Al}$ ZA but on different grains, providing a technique quality comparison.

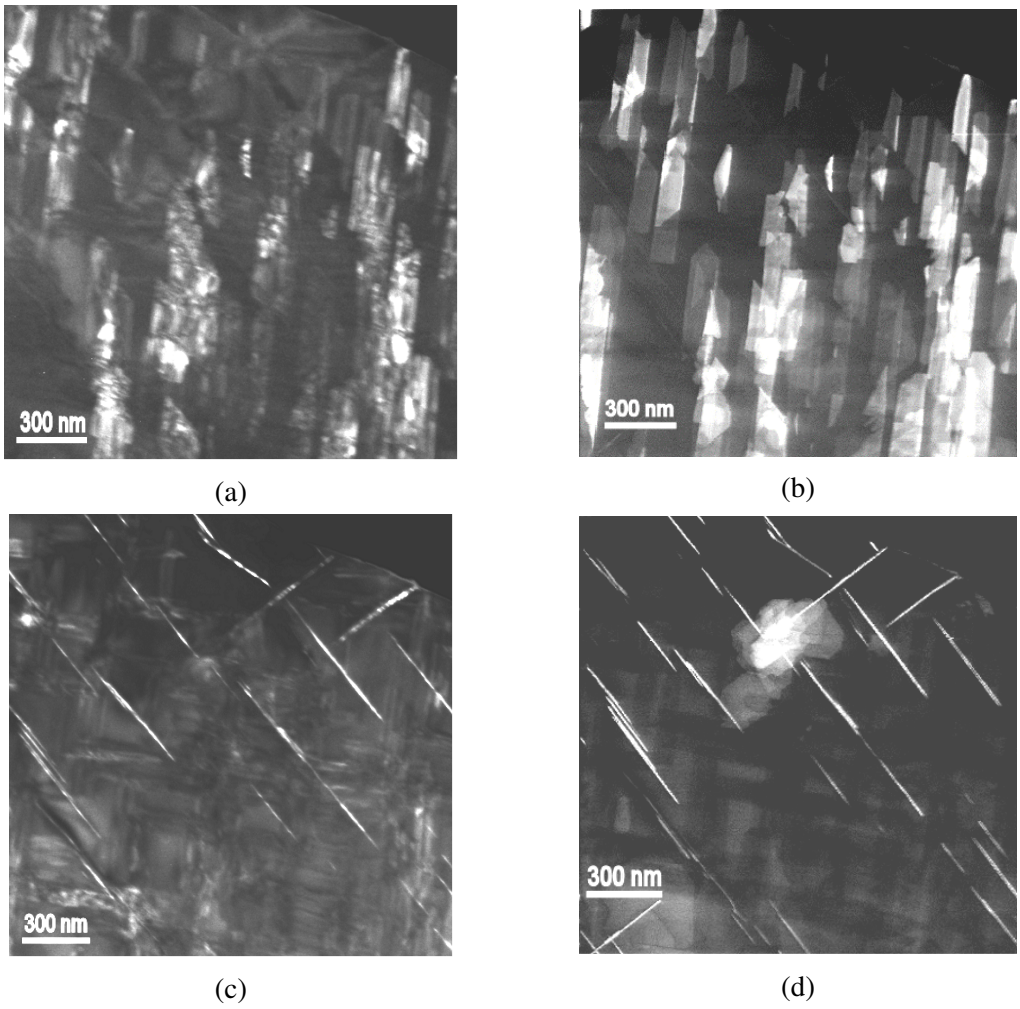

Figure 4.17: DFTEM- and VDF images near the $[001]_{Al}$ ZA of the CL alloy. (a) DFTEM- and (b) VDF image of the vertical T1-precipitate plate set. (c) DFTEM- and (d) VDF image of all three orientations of θ'-precipitate plates.

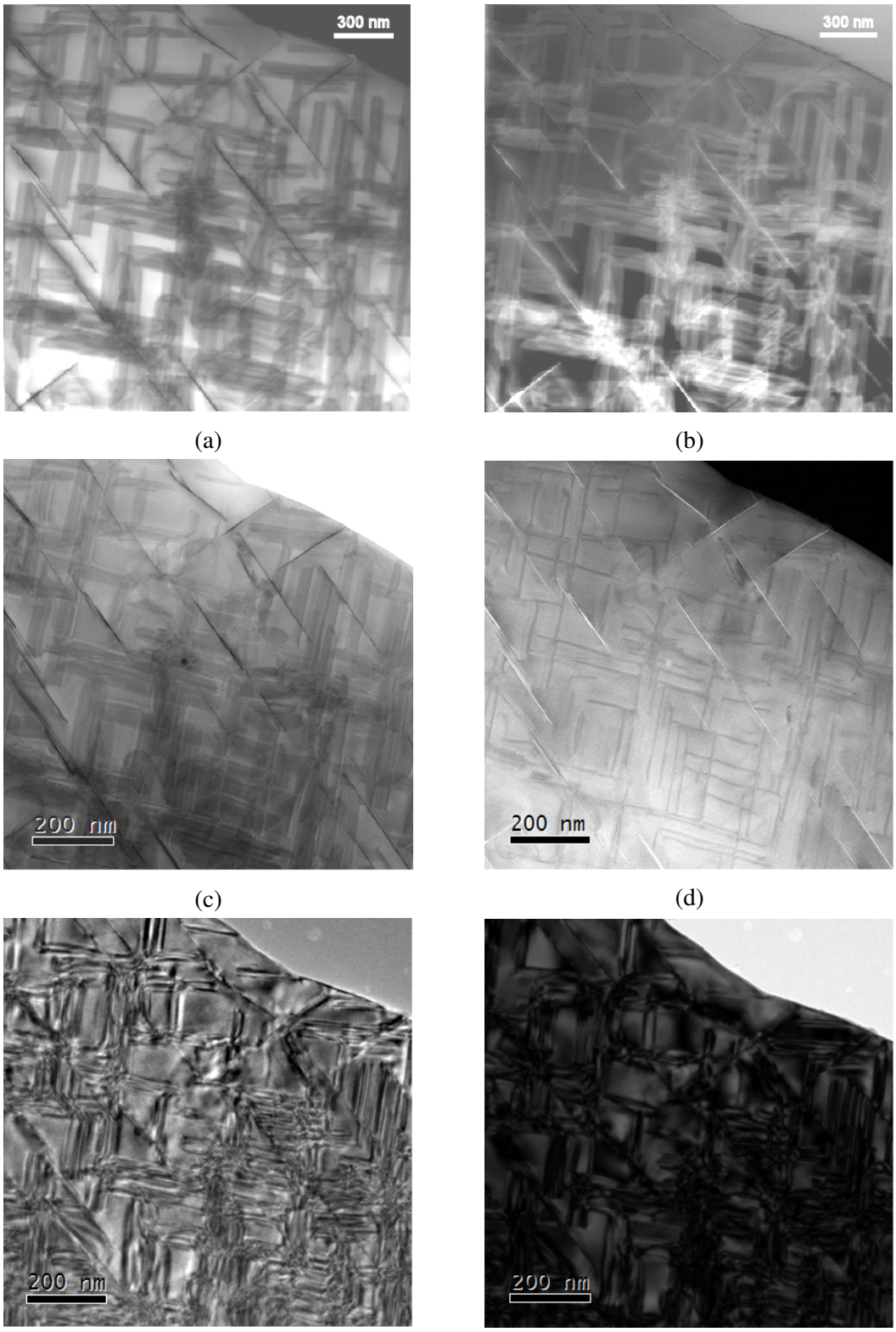

(a) (b)

(c) (d)

(e) (f)

Figure 4.18: (Caption two pages ahead)

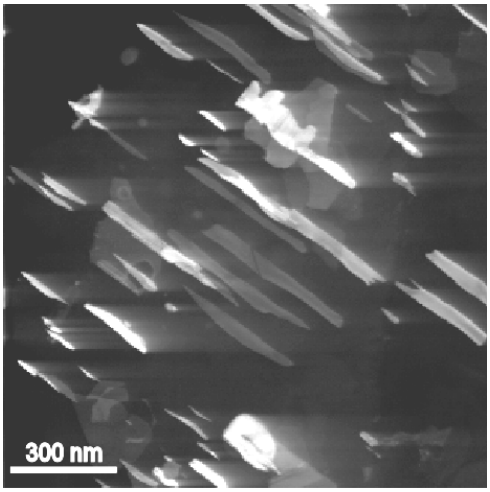

(a)

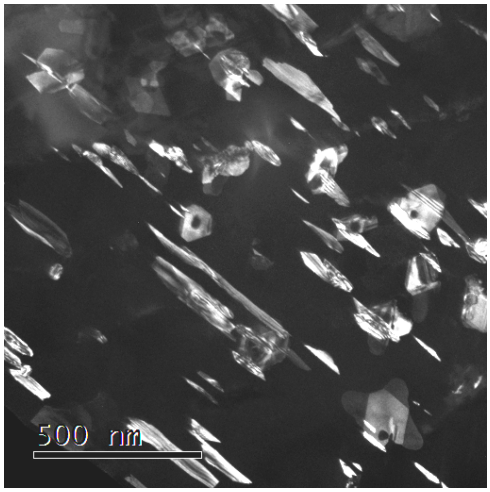

(b)

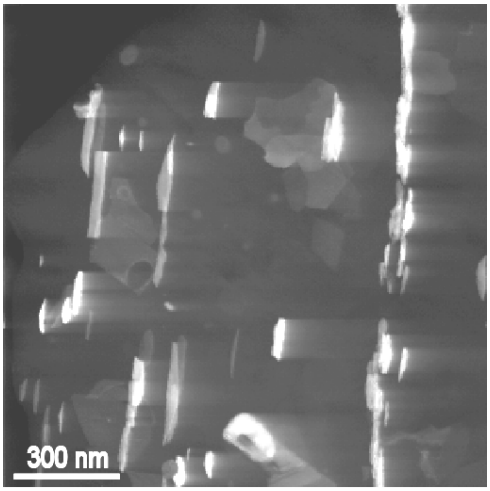

(c)

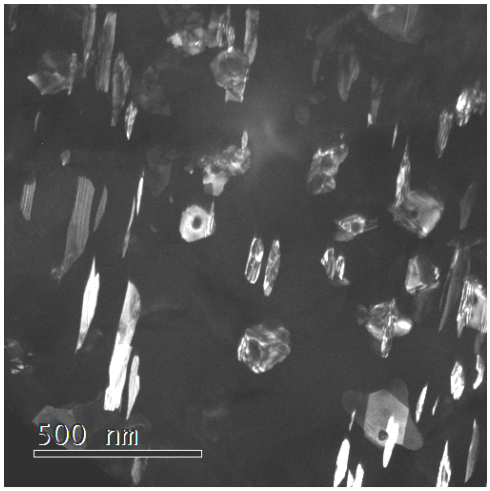

(d)

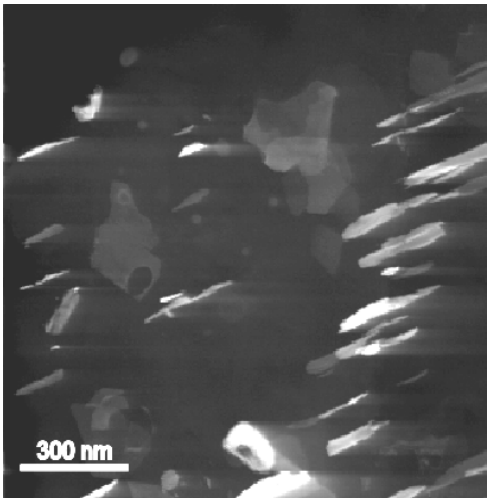

(e)

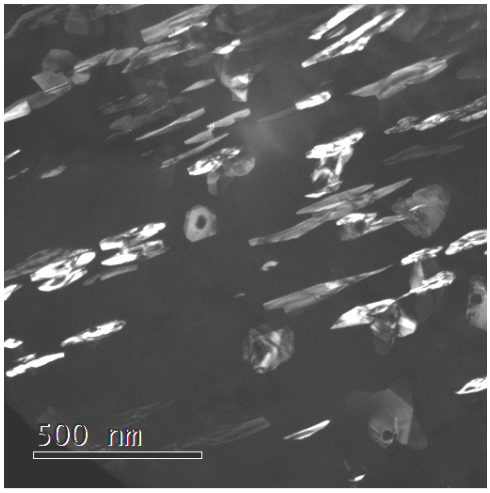

(f)

Figure 4.19: (Caption next page)

Figure 4.18: (Two pages back) Overview virtual- and CTEM images of an Al grain oriented near the $[001]_{Al}$ ZA using the techniques of: (a) VBF (b) VDF (c) BF-STEM (d) HAADF-STEM (e) HRTEM (f) BFTEM.

Figure 4.19: (Previous page) Comparison between VDF- and DFTEM images of three orientations of T1-precipitate plates, taken near the $[111]_{Al}$ ZA in alloy CL, but on different grains. (a) VDF image of $(1\text{-}11)_{Al}$ T1-precipitate plates. (b) DFTEM image of T1-precipitates of equal orientation as (a). (c) VDF image of $(11\text{-}1)_{Al}$ T1-precipitate plates. (d) DFTEM image T1-precipitates of equal orientation as (c). (e) VDF image of $(\text{-}111)_{Al}$ T1-precipitate plates. (f) DFTEM image of T1-precipitates of equal orientation as (e). Also visible in all images (a) through (f) are face-on T1-precipitate plates.

4.4 Al-Cu-(Mn,Fe) Dispersoids

As previously mentioned, there also exists Al-Cu-(Mn,Fe) dispersoids, referred to as T-particles, in the matrix of 2xxx series Al alloys. This section presents high magnification HRTEM images showing the rotation-twinned substructure of these T-particles, shown in figures 4.20 and 4.22. These are followed by their orientational mappings, as obtained through DP indexing of the full PED pattern stack. The maps are shown next to their reliability weighted equivalents, shown in figures 4.21 and 4.23. The section is concluded by showing misorientation plots across the marked lines in the T-particle 'fan'-structure, shown in figure 4.24.

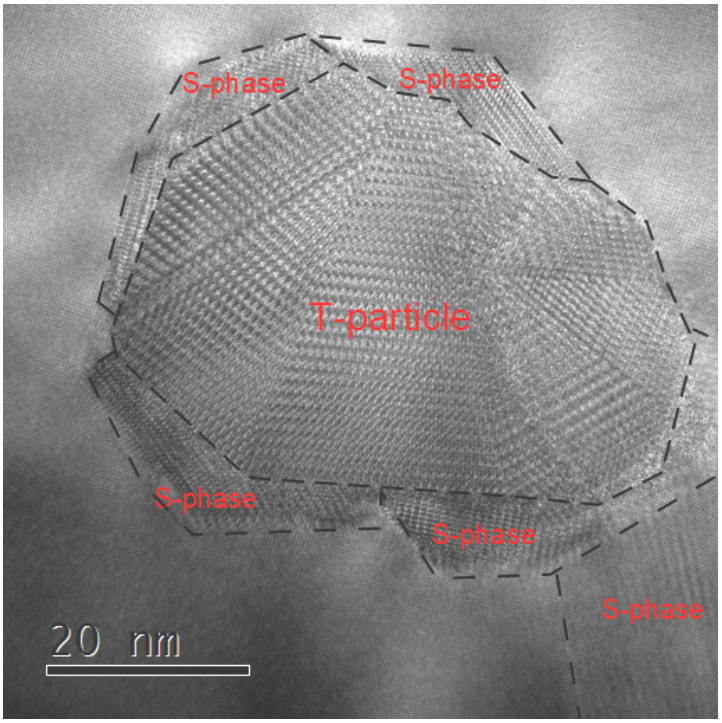

Figure 4.20: High magnification HRTEM image of a T-particle oriented near the $[001]_{Al}$ ZA in alloy MCA. S-phases are seen nucleating on this particle, extending into the plane of observation.

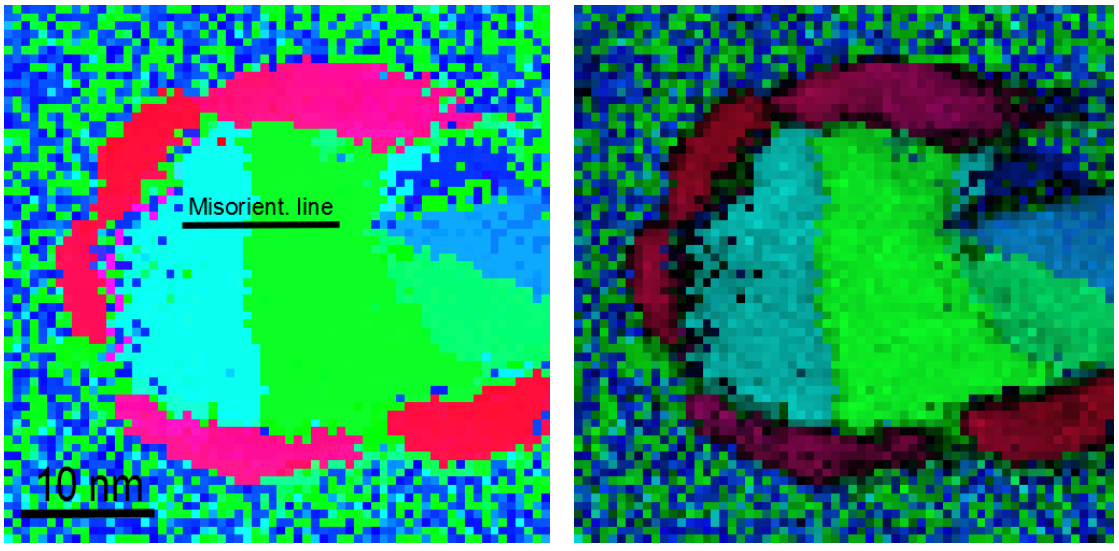

(a) (b)

Figure 4.21: (a) Orientational mapping of the T-particle in figure 4.20. (b) The orientational map of (a) times the reliability value given to each pixel through the indexing. Darker pixels are associated with higher uncertainties in mapping.

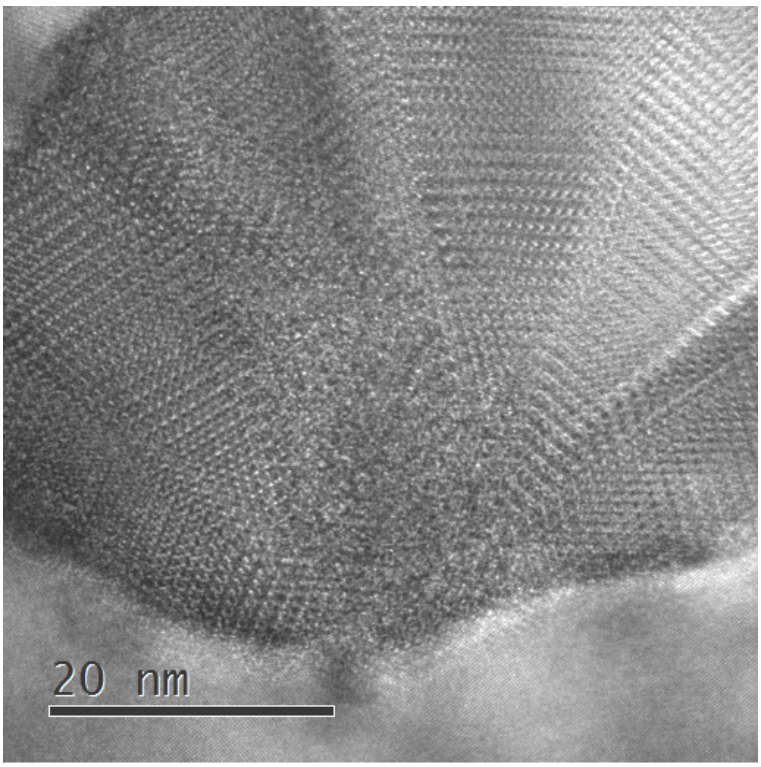

Figure 4.22: High magnification HRTEM image of a T-particle oriented near the $[001]_{Al}$ ZA in alloy MCA. This T-particle is highlighted as 'dispersoid' in figure 4.14 (c).

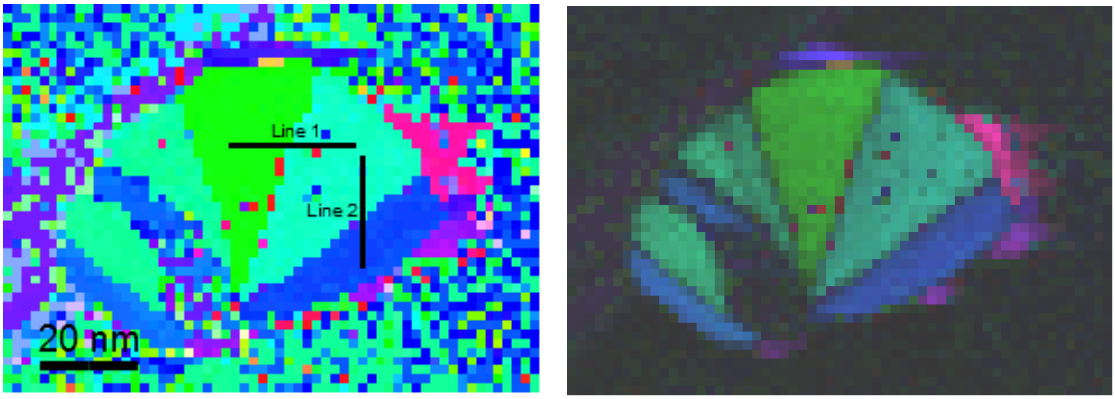

(a) (b)

Figure 4.23: (a) Orientational mapping of the T-particle in figure 4.22 oriented near the $[001]_{Al}$ ZA. (b) The orientational map of (a) times the reliability value given to each pixel through the indexing. Darker pixels are associated with higher uncertainties in mapping.

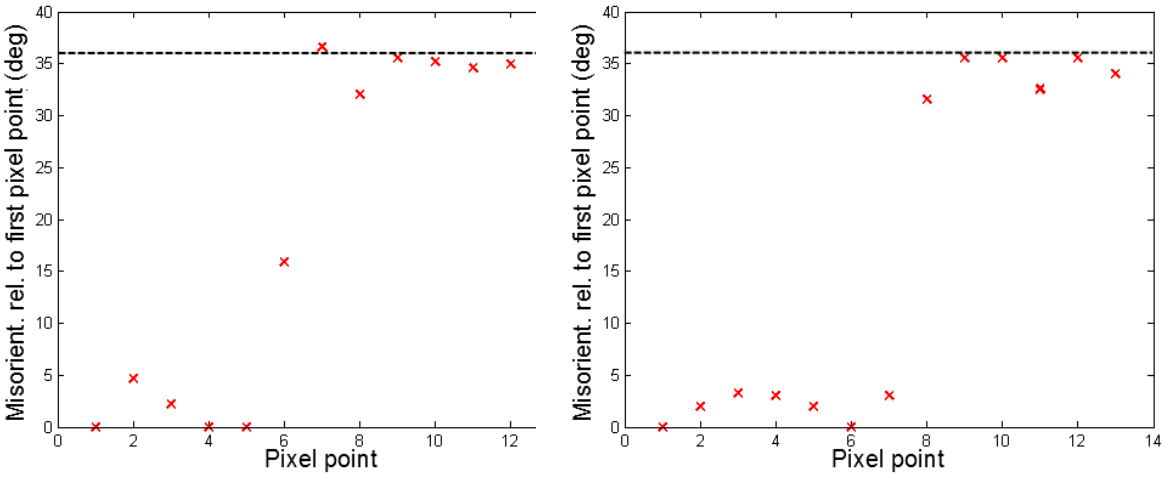

(a)

(b)

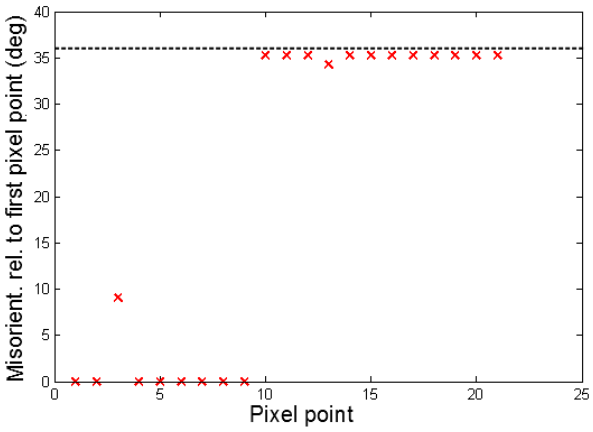

(c)

Figure 4.24: (a) Misorientations across marked line 1 in figure 4.23 (a). (b) Misorientations across marked line 2 in figure 4.23 (b). (c) Misorientations across marked line in figure 4.21. Dashed line indicate 36° rotation relative to the first pixel point.

4.5 SPED Data Decompositions

This section presents component decompositions of SPED data sets acquired in the specimen area of figure 4.25, obtained through blind source separation (BSS). The obtained component patterns are shown together with their associated 'loading maps', highlighting the spatial distribution of the component patterns.

It is only presented a brief selection of the obtained components. First presented is a closer look at the upper right dispersoid, shown in figure 4.26, followed by an examination of S-phase orientations present in this area, see figures 4.27 and 4.28. At the end of the section it is shown further BSS components of interest, highlighting other aspects in this specimen area, see figure 4.29.

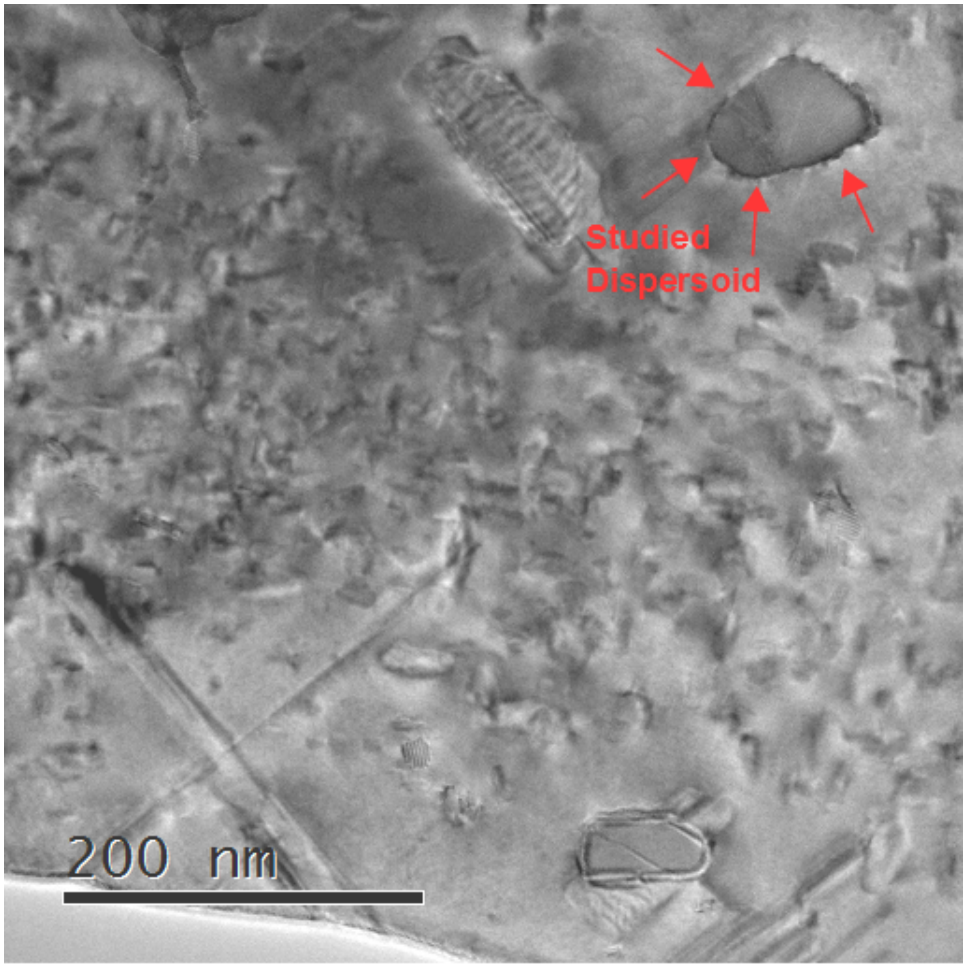

Figure 4.25: TEM image of an Al grain oriented near the $[001]_{Al}$ ZA in alloy MCA. This is the same area as depicted in figure 4.14. The studied dispersoid is highlighted.

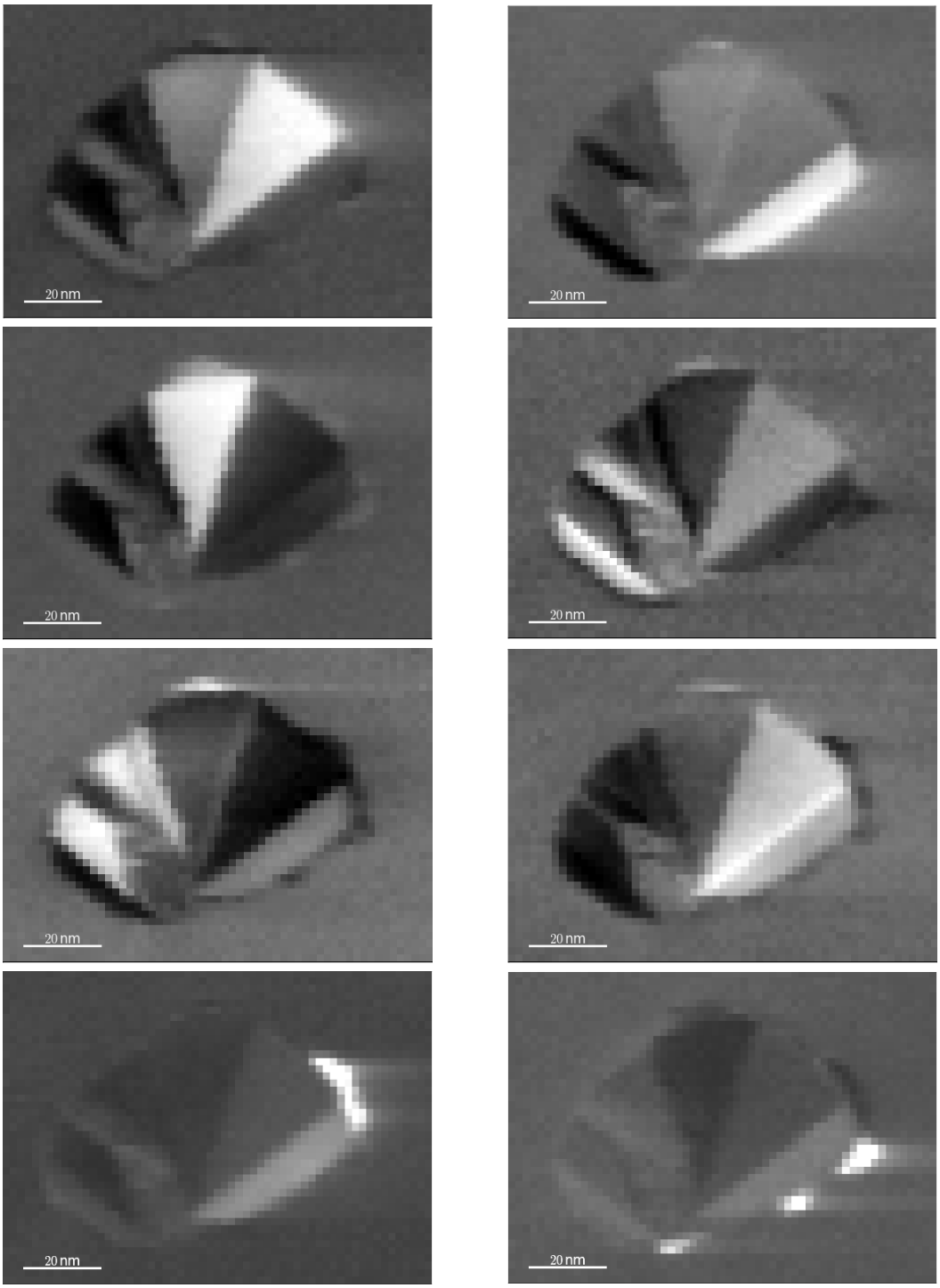

Figure 4.26: (a) through (h): Obtained loading maps from BBS acting on the cropped MCA $[111]_{Al}$ ZA SPED data set in the dispersoid region. Regions of equal orientation are highlighted, which is seen to pick out the dispersoid 'fan-shape' (a-f) as well as nucleating S-phases (g-h).

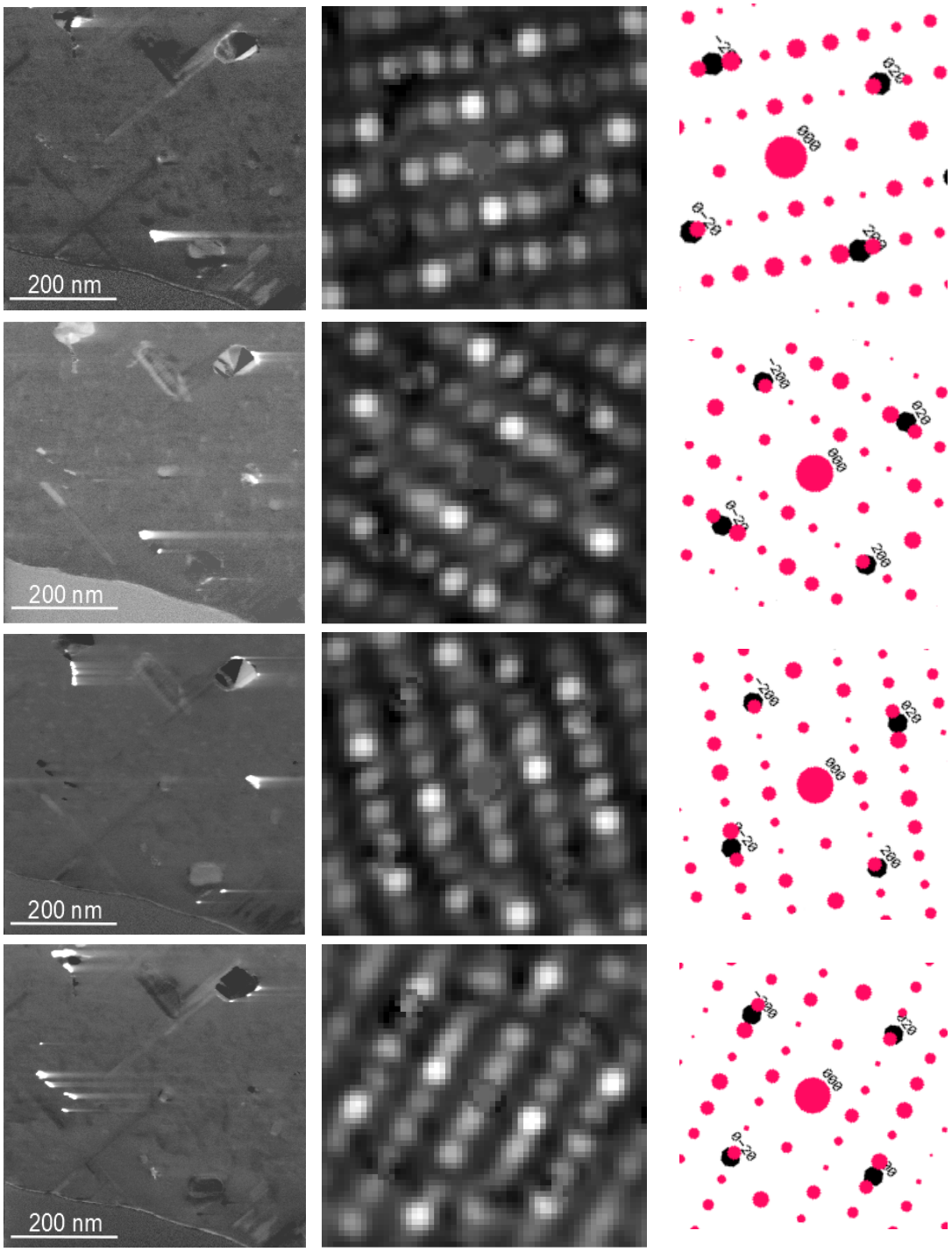

Figure 4.27: (Caption three pages ahead)

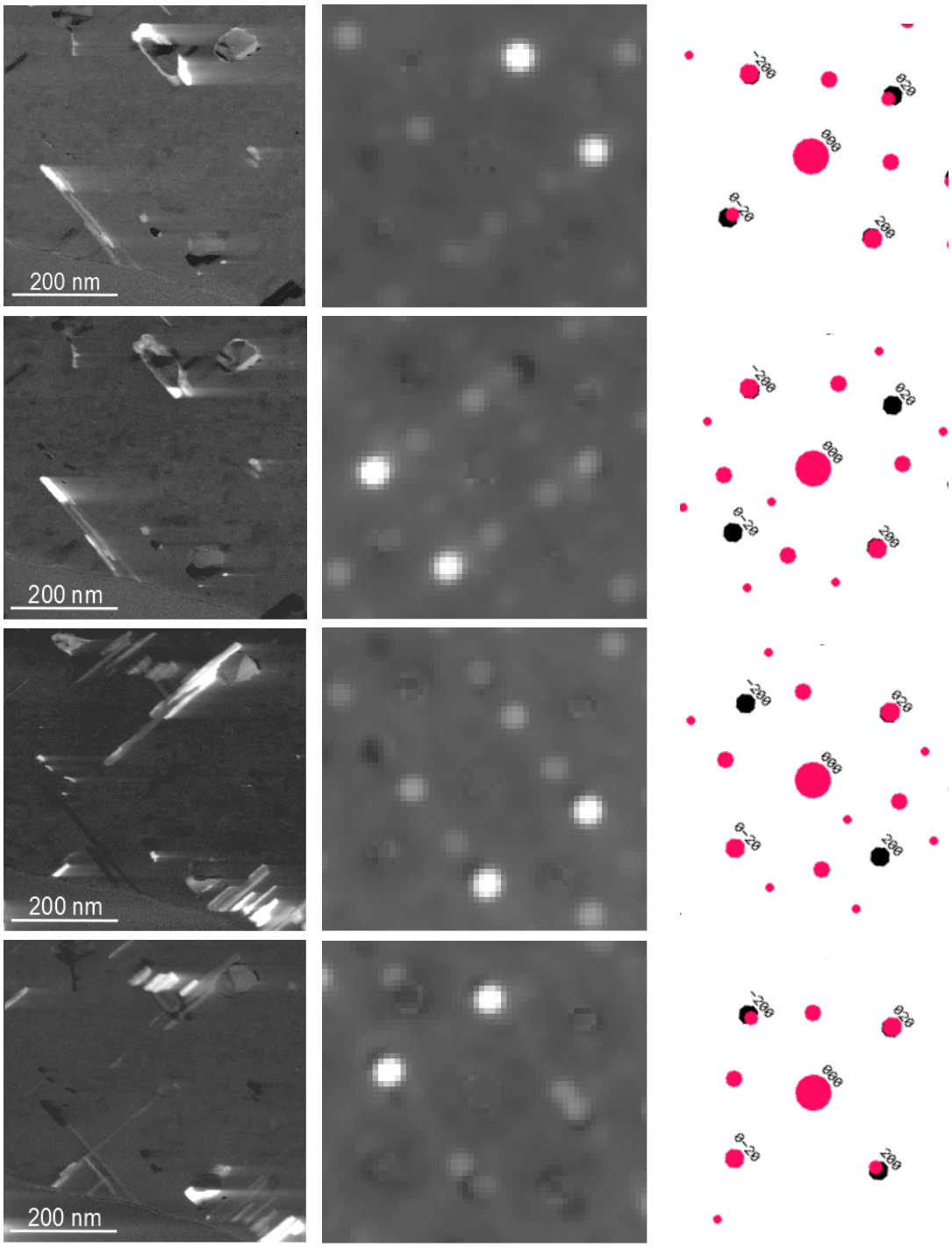

Figure 4.28: (Caption two pages ahead)

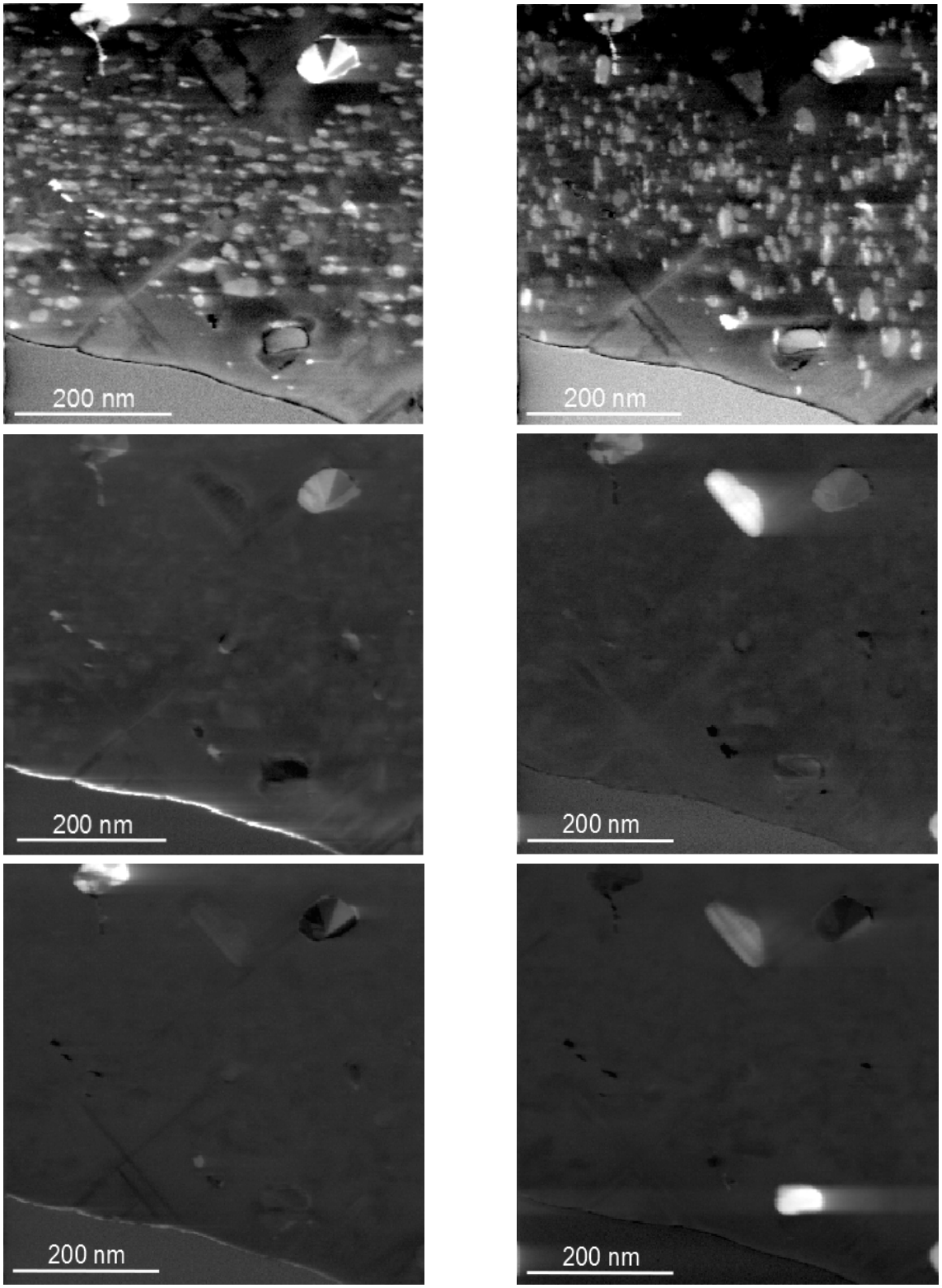

Figure 4.29: (Caption next page)

Figure 4.27: (Three pages back) Four individual S-phase orientations relative to the surrounding Al matrix shown as loading maps in the left column. These are shown next to their corresponding component patterns obtained through BSS, and to the matching simulated matrix-precipitate DP. From top to bottom they are $[010]_S$‖$[2\text{-}10]_{Al}$, $[010]_S$‖$[\text{-}120]_{Al}$, $[010]_S$‖$[120]_{Al}$ and $[010]_S$‖$[210]_{Al}$.

Figure 4.28: (Two pages back) Four individual S-phase orientations relative to the surrounding Al matrix shown as loading maps in the left column. These are shown next to their corresponding component patterns obtained through BSS, and to the matching simulated matrix-precipitate DP. From top to bottom they are $[010]_S$‖$[0\text{-}12]_{Al}$, $[010]_S$‖$[021]_{Al}$, $[010]_S$‖$[20\text{-}1]_{Al}$ and $[010]_S$‖$[102]_{Al}$.

Figure 4.29: (Previous page) Additionally obtained loading maps from the specimen area of figure 4.25. The upper two maps show the horizontal and vertical Ω-orientations. Center left map shows the boundary towards vacuum highlighted. The three remaining maps highlight the three remaining dispersoids in this specimen area.

Chapter 5

Discussion

This chapter elaborates on the obtained results of Ch. 4, starting with the kinematically simulated DPs and the summed PED pattern stacks. This is followed by an evaluation of what information can be extracted from the numerous virtual images presented, as recorded from several different ZA oriented grains in the two Al alloys. The quality of the formed virtual images are then compared to that of images obtained through conventional imaging techniques.

It is then given an extended discussion on both the acquisition of high quality SPED data, as well as the information obtainable through post processing. Hereunder, the presented results on T-particles and the multiple component decompositions in the last section of Ch. 4 are evaluated.

The concluding section of this chapter presents a discussion on the current development and future possibilities of the SPED technique.

An additional possible application of BSS component decomposition is presented separately in Appendix B.

5.1 Simulated and Recorded DPs

A first remark on the summed PED pattern stacks of section 4.1, recorded in the different low-order ZAs, is that the acquired patterns show a rich signal with numerous strong reflections, originating from both the Al matrix and the different phases present. This is in contrast to conventional SAED where it is mainly the Al reflections that show a strong signal, and which renders the weaker embedded phase reflections more difficult to discern, see figure 2.15. This is as expected, and was emphasized as a key motivation in applying the (S)PED-setup.

Due to the finite precession angle, φ, the beam is tilted slightly out of ZA orientation. Further it is rotated around the optical axis, usually for two full rotations. In visualizing the resulting rocking motion of the Ewald-sphere construction, see figure 2.10, one can understand how no single set of reflections, apart from those in proximity of the 000-spot, will be excited for the full Ewald-sphere rotation. If the beam were to impinge onto the specimen at exact ZA orientation, several ZOLZ reflection would be excited at the same

time, which is the case for the figure schematic referred to. With SAED at ZA orientation, these reflections are recorded for the full acquisition time, greatly exceeding the intensity of weaker precipitate reflections. In the (S)PED setup there is an effective averaging across the reciprocal space due to the integration across the Bragg condition. This averaging over the total dwell time, t_d, makes the intensity of weaker precipitate reflections approach those of Al, as seen from the PED patterns.

In comparing the total summed simulated and recorded DPs from each ZA, it is evident that the two main strengthening precipitates present in each alloy account for the majority of all phase reflections present. Again referring to the presented theory in Ch.2, this is to be expected in the over-aged alloy condition, as the precipitates present here approach their equilibrium structures in the precipitation sequences. This was the main reason for studying OA alloys, as the subsequent DP simulations and phase mappings become simplified. They should also yield stronger signals due to the increased dimensions of diffracting phases.

The simulated DPs are based on kinematical calculations, and even though the SPED scan geometry suppresses dynamical effects [29], the strongly interacting electron will still exhibit dynamical diffraction. The derivation of key results from kinematic diffraction theory in Ch.2 showed that this is to be expected for specimen thicknesses exceeding a couple of nm. This is certainly the case for the studied Al specimens, where typical imaged grain thicknesses are in the range 50-140 nm [32]. Therefore, dynamical diffraction spots will also be present in the PED patterns. These additional reflections are often located in proximity of the corresponding kinematical reflections, and adhere to the DP symmetry. This is due to the fact that they often coincide with the locations of kinematically forbidden diffraction spots, arising due to extinction effects.

Due to the multitude of reflections present in the summed DPs, and the extent of the diffraction discs, these added dynamical spots might be difficult to locate. Figure 5.1 highlights a possible set of dynamical diffraction spots present in the $[001]_{Al}$ ZA of alloy CL.

However, even in attributing additional symmetrically placed diffraction spots to dynamical effects, there are also additional reflections in the patterns that need explanation. As previously stated, there are several additional coexisting precipitates and other intermetallic phases present in the Al matrices of both alloys.

In the discussion of the precipitation sequences, there were given several intermediate phases along the evolution line of the main precipitates, which are not accounted for in the simulations. And albeit few in numbers, their reflections will be present. These intermediate phases often have slightly different chemical compositions, and exhibit small deviations in the lattice parameters of their equilibrium structures. Hence, having different fundamental unit cells and thus different underlying crystal symmetries, the DP reflections will be different from that of their equilibrium phases [20].

Among the other most common inter-metallic phases are constituent particles and dispersoids. These phases often greatly exceed the dimensions of the forming precipitates. The constituent particles are uninteresting for SPED studies, as they are very large and

rarely exhibit crystalline character. They are avoided in the SPED data recordings. In case the dispersoids exhibit decisive crystalline structures, these will be strongly diffracting phases present in the matrix. Especially the quasi-symmetrical T-particle studied in this thesis, with its underlying large unit cell, have a rich and dense DP which will contribute to the summed PED pattern stacks. More amorphous inter-metallic phases can contribute with characteristic concentric ring structured DPs. However, all larger phases present in the SPED data exhibit decisive crystalline characteristics in their DPs.

A further observation is that the summed DPs of the CL alloy exhibit far less reflections than those of the MCA alloy. This has two main explanations: first and foremost, the unit cell of the main strengthening precipitates of the MCA alloy (S and Ω) exhibit less symmetries relative to the surrounding Al planes than those of the CL alloy. As mentioned, the T1- and θ'-phase are hexagonal and tetragonal respectively, whereas the S- and Ω-phase are both orthorhombic. Since the phases are forming on similar Al planes, this yields more possible orientational relationships relative to the surrounding Al matrix. In turn, this gives many more unique DPs. The stated orientational relationships of section 3.4, gives 4, 3, 9 and 12 non-equivalent matrix-precipitate DPs for the T1-, θ', Ω- and S-precipitates respectively.

The second reason is due to the presence of the Al-Cu-(Mn,Fe) T-particles in high-symmetry orientations in the MCA SPED data sets. The T-particles are also present in the CL alloy, but were not recorded in the presented SPED data. These large, rod-shaped

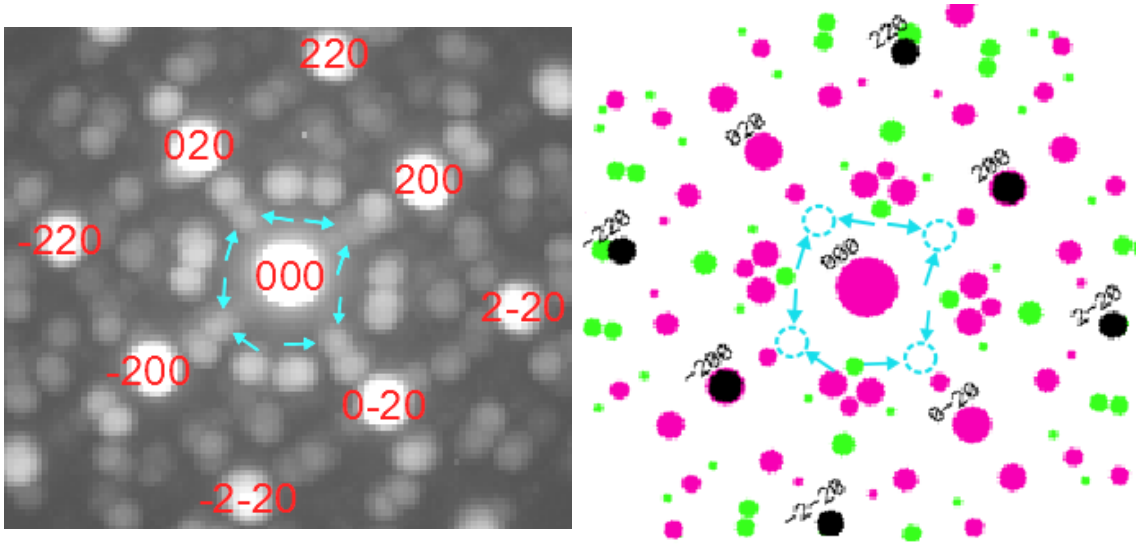

(a) (b)

Figure 5.1: (a) Summed PED pattern stack from the $[001]_{Al}$ ZA in alloy CL. (b) Simulated DP in the $[001]_{Al}$ ZA in alloy CL. In both images it is highlighted a possible set of dynamical diffraction spots associated with the θ'-phase (pink reflections). This figure is a slight modification of figure 4.1 (b) of section 4.1.

particles extend through the full matrix thickness. This claim is verified by looking at the dispersoid PED patterns, e.g. figure 3.5 used in explaining the data-cropping procedure. This PED pattern was taken on a dispersoid 'fan' (see figure 4.22), and is seen to contain no Al reflections. This particular dispersoid exhibited its orientation of highest symmetry relative to a $[001]_{Al}$ ZA. The well-known 4-fold symmetry of the $[001]_{Al}$ ZA (indexed reflections of figure 5.1 (a)) is seen to be fully absent, and hence the T-particle must extend through the full lattice. Furthermore, they are seen to exhibit a highly crystalline character with large unit cells. This combined, results in the presence of a dense set of strong reflections in the PED pattern sums of the MCA alloy.

The origin of additional reflection spots in the (S)PED data, whether occurring due to dynamical effects or the presence of phases different than the main strengthening ones, can be inferred from concepts previously introduced. In order to limit the discussion, while still going somewhat into depth on this topic, the focus will be with the CL alloy $[001]_{Al}$ ZA DP and the determination of the character of the highlighted reflections not accounted for in figure 5.1.

In order to determine the nature of the additional DP spots seen in this figure, the possible explanations will be tested one by one. In this particular data set, the possibilities are further narrowed because as observed in the virtual images of figure 4.11, there are no constituent particles or dispersoids present in this specimen area. This is also seen from the CTEM images of figure 4.18 (b) through (d). The reflections are therefore due to either the related precipitate structures as shown in the sequence 2.5 of section 2.3 Ch.2, or, as hypothesized, dynamical effects.

The preceding phase of θ', i.e. θ'' (sometimes referred to as GP-II zones), has the chemical composition Al_3Cu. The underlying unit cell is tetragonal, and perfectly coherent with the Al matrix in the a and b directions, but not along c. Commonly accepted values are $a = b = 4.04$ Å and $c = 7.90$ Å [43]. Being coherent in the a and b directions means that the resulting DP reflections will coincide with the Al reflections, and hence do not account for the additional reflections of figure 5.1, which are along the reciprocal a and b directions. These are parallel to the real space directions in the tetragonal system.

The equilibrium θ-phase has the chemical composition Al_2Cu (same as θ') with $a = b = 0.6067$ nm and $c = 0.4877$ nm. These extended a and b dimensions would lead to reduced reciprocal distances, and hence could coincide with the undetermined reflections sought. However, the θ-phase exhibits the I4/mcm space group [44], and is incoherent with the surrounding Al matrix, exhibiting at least 22 different orientational relationships [45]. Therefore, nor is θ the likely candidate for these added reflections.

This leads to the conclusion that these are a consequence of dynamical diffraction. This claim is verified by the simulations of [20] (p. 14, fig. 23 (c)), which show that they are in fact due to double-diffraction. This is a special type of multiple elastic scattering where a diffracted beam traveling through the crystal is re-diffracted.

5.2 Virtual Images

There is a wealth of information that can be extracted from the SPED data sets by forming virtual images of selected VA positionings. The presented VDF images are mainly focused with the distributions of the main strengthening precipitates present in the matrix. There are however additional important aspects that can be highlighted by this procedure, and which will be briefly mentioned in a later section.

In first doing a rough overview of figures 4.11 through 4.15, an initial remark is that the VDF images exhibit sharp and consistent contrasts between precipitate phases and the surrounding Al matrix. Furthermore, despite the rich DPs formed (see the preceding section of Ch. 4) and the extent of the DP discs, it is observed that the VDF images are able to satisfactory extract individual precipitate orientations, with low background signals recorded, as verified by the signal-to-noise-(S/N) ratios of the VDF image pixel read-outs. Even more importantly, this S/N ratio remains nearly constant all over the constructed image. The signal from an individual precipitate also remains fairly constant all across its dimensions, which yields an especially impressive contrast between precipitate boundaries and the surrounding matrix.

5.2.1 Alloy CL

The CL alloy data set recorded near the $[001]_{Al}$ ZA, see figure 4.11, will be presented first. Image (a) of this figure shows a VBF image of the scanned specimen region, which highlights the large (projected) area occupied by the embedded precipitates. The extremal lengths of the forming phases are in the range 0.2-1.1 μm. These large dimensions are a consequence of the long AA time (64 days) used in obtaining the OA condition in this alloy, combined with the high solute additions. Smaller phases in the matrix have mostly been completely 'absorbed' by the larger ones during age hardening.

In (b) and (c) the hexagonally shaped, T1-precipitate plates forming on $\{111\}_{Al}$ are seen inclined 54.75° relative to the ZA. In (b) one can observe the 'vertically' oriented pair of T1 plate-sets forming on $(\text{-}111)_{Al}$ and $(1\text{-}11)_{Al}$, oriented 70.53° relative to each other, as calculated using equation 2.3. Correspondingly, (c) shows the 'horizontally' oriented $(111)_{Al}$ and $(11\text{-}1)_{Al}$ pair of T1 plate-sets. Image (d) shows the octagonally (sometimes rectangular) shaped, θ'-precipitate plates forming on $\{001\}_{Al}$, seen edge-on in two directions and face-on in the last.

The thin T1-precipitate plates, nearly constant at 1.39 nm thickness [3], are seen to exhibit a strong signal and good contrast, which importantly renders the plate boundaries clear. This reveals the growth direction of the T1-plates. Looking closely at the plate boundaries, it is seen that the hexagon corners are oriented along $\langle 001 \rangle_{Al}$ directions. The two straight edge segments run perpendicular to $\langle 110 \rangle_{Al}$. Most impressively, it is seen that even overlapping plates can clearly be discerned and visualized, some of which are highlighted in the figures.

This impressive feat shows one of the strengths in applying this technique. The T1-plate thickness relative to the total area specimen thickness (typically 70-100 nm, some 100s of nm from the sample edge) is slightly above 1 %, but still this phase yields strong DP reflections as seen in figure 4.4 (b). This is due to the technique's effective integration across the Bragg condition, as well as the precession angle out of ZA orientation, making the precipitate reflections relatively stronger in intensity. In a typical ZA SAED pattern, the Al reflections strongly dominate in intensity, and their background often completely covers the weaker precipitate reflections in close proximity. Furthermore, the technique also effectively averages over specimen surface buckling and deviations. This is confirmed by the good contrast consistency over the full plate extent, which sometimes exceed 1 μm, and hence extending over a varying surface profile.

A similar discussion holds for the θ'-precipitate plates shown in image (d). Edge-on orientations are seen as sharp needles, revealing their plate-like character, typically 3-10 nm in thickness. The face-on precipitates are similarly to the T1-plates seen with good contrast, and discernible when stacked above one another. Interestingly in this area, the θ'-precipitates are seen to exhibit a clear tendency of clustering, in the upper centre of the image. This might be due to nucleation on a line defect present in this region. Albeit few in presence, the face-on θ'-plates further show the plate growth directions. Tracing out the octagon edges, it is seen that these grow as four $\langle 001 \rangle_{\mathrm{Al}}$ segments combined with four $\langle 111 \rangle_{\mathrm{Al}}$ cut corners.

It is known [32] that for the over-aged condition, the T1-precipitates are largest in number densities, and do not seem to exhibit clustering, but are more or less homogeneously dispersed around the Al matrix, although often nucleating at GBs. The θ'-precipitates were found to be more scarcely populated in this condition, and more abundant in some directions than others. This is seen to be the case for the specimen area of 4.11 as well.

Figure 4.12 is recorded near the $[111]_{\mathrm{Al}}$ ZA of alloy CL. Image (a) shows a VBF image of the scanned specimen area. Images (b) through (d) show three out of four unique orientations of T1-precipitates as observed near the $[111]_{\mathrm{Al}}$ ZA. They are inclined 70.53° relative to the ZA, and 109.47° relative to each other.

Of added interest in these images is the presence of a GB, seen highlighted to the right in the images. It is observed that a larger discontinuity in the matrix, such as this GB, is seen to strongly nucleate precipitates along its full extent. GBs often result as constant matrix misfits, maintaining constant atomic plane stacking relations along large segments of their lengths. This Al grain misfit acts as a strong driver for heterogeneous nucleation, as explained in the theory section. Furthermore, the specific atomic plane misfit along this GB favors certain precipitates and growth directions to others [17]. This is supported by the observation of predominantly $(11\text{-}1)_{\mathrm{Al}}$ T1-plates (b) forming along the GB. Also, the $(11\text{-}1)_{\mathrm{Al}}$ T1-plates (c) are seen to have a strong presence on the GB. The $(1\text{-}11)_{\mathrm{Al}}$ plates (d) along the GB however, are seen to be very few and exhibit small dimensions, thus not having a favorable orientation relative to the Al grain misfit in this area.

Another case of interest are the large observed 'holes', some 10s of nm in diameter, in the T1-precipitate plates, highlighted in (c). This is also seen in the DFTEM images of figure 4.19, taken on a different Al grain in a similar orientation. Having obtained a SPED scan over the specimen area, one can reliably confirm that they are indeed holes, and not a different coexisting phase on which the T1-plate has nucleated. By studying the PED patterns acquired from the 'hole' region, it is observed that there are no additional DP reflections to those of Al in the $[111]_{Al}$ ZA. As the technique has proved highly sensitive to diffraction from phases of small dimensions, e.g. the case for T1-plates, this is taken to be reliable evidence for the absence of a phase in this region. In combination with high-resolution EDS-mapping, this would be a decisive proof.

It is not probable that these holes have resulted from precipitate nucleation on a phase which has subsequently dissolved during heat treatment. This is due to the fact that apart from the main forming precipitates, the dispersoids and other inter-metallic phases in these Al alloys are usually much more thermodynamically stable, and show little evolution exposed to typical AA temperatures.

A likely explanation is that they are artifacts of the TEM specimen preparation procedure. The strong nitric acid (HNO_3)/methanol (CH_2OH) mix applied in the electropolishing procedure has previously been observed to produce similar effects at the author's TEM group. It can lead to a local etching in these large phases, which would explain the resulting holes observed.

Figure 4.13 shows the (a) face-on $(111)_{Al}$ T1-plates, as well as the different orientations of θ'-precipitates as inclined 54.75° relative to the $[111]_{Al}$ ZA, in the same specimen area as figure 4.12. Image (a) shows an impressive signal from these very thin plates, making it discernible when the plates are stack above one another. Furthermore, the plates are seen with a consistent contrast, giving clearly visible boundaries.

It is further observed that only the $(100)_{Al}$ θ'-plates are nucleating along the GB. Similarly to the $(11\text{-}1)_{Al}$ T1-plates along the GB, these grow small in dimensions as compared to their 'bulk' orientations.

The two figures 4.12 and 4.13 combined, account for all orientations of the two main strengthening precipitates present in the $[111]_{Al}$ ZA. The images are all seen to extract the precipitates of interest to a satisfactory extent. These are the main features of interest in the specimen, however, there is additional complementary information obtainable through the formation of virtual images/loading maps, as will be mentioned in a later section.

5.2.1.1 Thickness measurements from the T1-precipitate plates

The 64 days long AA time of the CL alloy, combined with the high solute content of this alloy, should indicate that the precipitates have grown to extend through the whole thickness of the TEM specimen. This claim is supported by the observation of reduced T1-precipitate plate dimensions in closer proximity of the specimen edge. It is seen that plates of similar distance to edge correspondingly exhibit similar widths, for both the horizontal and vertical plate-set, indicating that they have grown to their maximum obtainable widths by extending through the full matrix thickness, see figure 4.11 (b) and (c).

Knowing the plate orientations relative to the ZA, the T1-plate widths should allow for a reasonable estimate of the specimen thickness in this specimen region. One can estimate the average thickness, $\langle t \rangle$, as

$$\langle t \rangle = \langle l \rangle \cdot \sin \Phi,$$

where $\langle l \rangle$ is the average measured plate length in the $[110]_{\mathrm{Al}}$ direction, and Φ is the angle between the plate and the ZA (54.74° in this case), see figure 5.2. Averaging over a few of the center plates gives an estimated thickness of $\approx$ 100 nm in the center of this specimen area. Moreover, it is estimated as $\approx$ 150 nm farthest from the edge, and as $\approx$ 50 nm some 100 nm from the edge, hence exhibiting a fairly linear height profile. These are reasonable estimates, as compared to the log-ratio thickness measurements of [32].

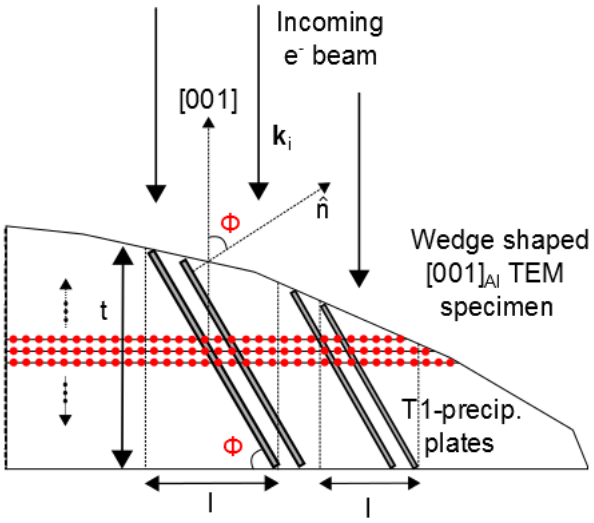

Figure 5.2: Thickness estimation geometry of a wedge-shaped TEM specimen having T1-plates extending through the full matrix thickness. The crystal is oriented in the $[001]_{\mathrm{Al}}$ ZA. Notations are explained in the text.

5.2.2 Alloy MCA

Figure 4.14 (a) through (e) shows several of the possible 12 and 9 orientations of S- and Ω precipitates respectively, as observed near the $[001]_{\mathrm{Al}}$ ZA in the MCA alloy. The VBF image of (a) shows the presence of several smaller phases in high densities, as well as four larger dispersoids particles.

The S-precipitates, seen in images (b) and (c), form as laths on $\{001\}_{\mathrm{Al}}$, and are seen in the ZA showing their maximum lengths, i.e. along the $\langle 001 \rangle_{\mathrm{Al}}$ directions. Also highlighted are S-phases extending into the plane of observation. The images indicate that the S-phases are sparsely distributed, often nucleating in close proximity to larger dispersoid particles in the Al matrix, as clearly seen from figure 4.20. They are inhomogeneously

distributed, often forming near larger matrix imperfections.

The small, hexagonally shaped Ω-precipitate plates forming on $\{111\}_{Al}$ are seen faintly visible, inclined 54.75° relative to the ZA in images (d) and (e). The Ω-precipitates exhibit small dimensions, rarely exceeding 30 nm in their extremal dimensions. Furthermore, they are seen in high number densities, homogeneously distributed around the matrix.

Around the imaged dispersoids, it is seen to exist a precipitation free zone (PFZ) of some tens of nm radius.

Figure 4.15 shows the S-phase laths inclined relative to the $[013]_{Al}$ ZA. The observed large clustering of S-precipitates indicates that the specimen area is prone to many line defects, some possible of which are highlighted. This further indicates the tendency of S-phases to nucleate on matrix imperfections.

The RGB images of figure 4.16 combine many of the preceding individual VDF images. These images (a) through (e) further highlight the complex interplay of precipitates and dispersoids present throughout the Al matrix. These images display the great control in extracting individual component distributions in these multiphase alloys. These are combined to give clear images allowing one to understand the nature of these alloys, without the complex additions of strain fields, phase contrasts, and so forth.

5.3 Comparing Virtual- and CTEM Images

The CTEM imaging techniques corresponding to the virtual techniques of VDF and VBF, is DFTEM and BFTEM respectively. As previously explained, in these CTEM techniques, a real aperture is inserted into the TEM column, thus allowing only electrons scattered to certain angles to pass on to form the final image on the fluorescent screen/CCD camera. In figure 4.17 (a) and (c), DFTEM images taken at the same specimen area and similar magnification as that of figure 4.11 (b) and (d) are presented, and whom are re-given in figure 4.17 in (b) and (d) for clarity.

Placing a real aperture over weak precipitate reflections accurately in SAED is challenging, as the reflections are often too weak for observation on the fluorescent screen. The procedure is conducted by using a long exposure diffraction pattern (or possibly a simulated DP) as guidance, while placing the smallest aperture obtainable at the sought position. Some TEMs are equipped with motorized apertures, which can be of help.

As can be seen from these DFTEM images, the placements have not been ideal, and therefore the obtained images does not fully capture the precipitate specific electrons scattered. In addition they are seen to have significant background intensities, which from pixel read-outs are sometimes equal in intensity to the boundaries of highlighted precipitates. This challenge is greatly simplified in forming VDF images. The full image formation procedure is conducted post-session. VAs of chosen size (diameter pixels) are maneuvered over the SPED data set, which shows clearly visible precipitate reflections. These are much closer in intensity to the Al reflections, which is attributed to the effect of precession.

The obtained image quality is seen to be strongly in favor of the VDF images. In these DFTEM images, important information about the precipitate distributions and morphologies is lost due to non-ideal aperture placements.

Taking great care with aperture positionings, as well as using long exposure times, DFTEM images of higher quality, as seen in figure 4.19 can be recorded. Acquiring these DFTEM images took many attempts, due to the difficulty in selecting the individual sought reflection in the weak DP. Acquiring these three DFTEM images required about the same time as a normal 300^2 pixel, 20 ms dwell time scan ($\approx$ 40 min). Due to the time limitations of a typical TEM session booking, and the difficulty with retrieving a specific specimen area in subsequent sessions, these DFTEM images were not recorded at the same SPED scan site. However, they are taken using the same reflections and at similar orientation and magnification. In this figure, the image qualities are seen to approach one another, and each technique's stronghold becomes apparent.

In favor of VDF are:

- Contrast consistency: the VDF images are seen to exhibit an even intensity across the full precipitate extent, including boundaries. This is attributed to the effect of beam precession during recording. The DFTEM image contrast is seen to vary considerably over each precipitate, often rendering precipitate boundaries hard to discern. Furthermore, the contrast inconsistency with DFTEM can make e.g. precipitate counting difficult, as certain features located on a larger phase exhibiting strong signals might be interpreted as an individual diffracting phase. Large differences in contrast with VDF images are almost unconditionally associated with a different diffracting phase.

- Low background signals: image pixel read-outs outside the precipitate areas show little to no variation all over the formed VDF images. This is due to the great simplicity in VA positioning on strong precipitate reflections, using apertures selected from a broad range of sizes. Even high-quality DFTEM images exhibit background signals approaching precipitate boundary intensities at certain image points.

In favor of DFTEM are:

- Spatial resolution: SPED resolution is affected by a range of parameters to be elaborated in the next section. The most important parameters however, is the precessed beam's effective spot size on the specimen, the specimen thickness, and the step size employed in the scan recording. Zooming in on the VDF images shows pixelated precipitate boundaries, due to the relatively large step size used (4.5 nm in the CL scans). Increasing the number of pixels used makes the scan time exponentially increase.

- Technique simplicity: DFTEM imaging is a routine CTEM imaging technique requiring a minimum of experience and time to conduct. However, obtaining images of similar quality as the VDF images of these precipitates required care and multiple attempts.

Figure 4.18 shows VBF and VDF overview images as compared to CTEM imaging techniques taken at the same specimen area and similar magnification. It is seen that the virtual techniques improve on capturing the precipitate distributions throughout the matrix. The virtual images show an impressive sensitivity to precipitate scattering from these very thin phases, providing images reminiscent of more familiar 'X-ray absorption images' of e.g. human tissue and bones. Images (e) and (f), obtained using HRTEM and BFTEM respectively, are difficult to interpret due to the sensitivity towards strain fields, phase- and diffraction contrasts, etc. The techniques fail to capture the information on precipitate distributions and morphologies that we seek.

The STEM images are less prone to these effects, and are seen to provide clear images requiring less interpretational efforts. The HAADF-STEM image of (d), is however seen to fail in capturing the extent of the T1-plates. This may have several explanations, possibly including contrasts due to electron channeling effects in the beam propagation through the precipitates, which are inclined relative to the Al matrix. In addition, the poor scattering strength of Li-atoms in these precipitates might have an effect on recorded intensities. The best CTEM imaging technique is seen to be BF-STEM, seen in (c). Here the T1-plate extent is better captured than in the DF equivalent. This might support the idea of an increase in channeling effects relative to Z-contrast. An increased electron density could experience channeling, which would increase the amount of electrons in the forward direction. These would fail to be captured by the annular detector, but would increase the effect of mass-thickness contrast, which is captured by the BF-STEM detector.

It is interesting that unlike the STEM techniques, both the VBF and VDF capture the full extent of precipitate widths. The contrasts of VBF and VDF are both seen to surpass that of BF-STEM. Both STEM and virtual imaging are scanning techniques using narrow probes, although with different convergence angles. With the complex addition of a rocking motion introduced by the precession, it becomes a difficult topic to explain the differences seen with these imaging techniques. It could be that the angular spread caused by the precessing motion mitigates the effect of channeling, thus retaining strong diffraction contrast. The averaging over surface buckling with the PED technique could also be of importance in explaining the observed differences. This discussion is will not be pursued further, but is noted as an interesting aspect of the different techniques applied in this thesis.

5.4 Data Acquisition and Processing

Acquiring high quality SPED data puts strict requirements on the utilized hardware and its controls, applied scan parameters, the specimen material and the alignment procedure. This is especially the case when running SPED scans on very small specimen areas, thus pushing the setup to its spatial resolution limits. In serving as a future reference on SPED work, as is one of this thesis' main goals, the following presents a brief discussion on ideal parameters and acquisition techniques. Table 3.2 summarizes the main acquisition

parameters adjusted in the SPED setup.

The subsequent data processing used for obtaining the orientational maps of the T-particles, as well as the component decompositions in the subsequent section of Ch. 4, put an important requirement on the obtained SPED data. It was found that running ASTAR Index and HyperSpy's BSS algorithm yielded best results when using cropped data sets from the DP region interior to, and just including, the first Al reflections for the two procedures respectively. As the T-particle unit cell has large lattice parameters, the DP is rich within this cropped DP region, see figure 3.5. It therefore allowed for reliable phase and orientational identifications even when only using about 10% of the DP pixels.

In applying the memory intensive BSS algorithm, the cropping is merely used as a means to provide data sets of more manageable size. It was found that the sets should not exceed 300 MB, as this pushed the RAM usage to $\approx$ 95% of the 32 GB at the applied computer's disposal. Furthermore, the i7 (mod. 3770) 3.43 GHz processor with 4-cores was pushed to a stable $\approx$ 70% of total capacity for a typical duration of 30 min.

The ASTAR indexing and BSS data processing procedures put the SPED scan quality focus with the DP region around, and interior to, the first Al reflections. Hence, the inner DP region, see figure 3.5 (b), should ideally contain (just) separable reflections with sufficient intensity. Some overlap is not a significant problem as long as the individual reflections can be discerned. All parameters listed in table 3.2 affected this in different ways.

In acquiring scans from small specimen regions (< 200 nm^2), it is in the following list briefly described the optimally employed scan parameters, followed by a note on the acquisition procedure:

- Spot Size (s): in order to achieve the highest resolution, one should use the smallest NBD-mode spot size obtainable. The JEOL JEM 2100F FEG (S)TEM allows for a 0.5 nm spot size. This necessarily reduces the recorded intensity in each pixel, as a smaller specimen area is illuminated at each scan pixel. The applied dwell time, t_d, should therefore be increased.

- Convergence Angle (α): the ideal α should allow individual reflections to be identified while maintaining high intensities. A lower α gives a smaller beam current with spot size kept constant. α = 0.83 or 1.0 mrad (instrument specific setting α = 3 or 4) was found to be optimal for the dense T-particle reflections.

- Dwell Time (t_d): working with Al alloys at a HT of 200 kV, the applied dwell time, t_d, needs to be reasonably high in order to achieve sufficient intensity, but while keeping the C-contamination not to severe. 40 ms allowed a sufficient reflection intensity for reliable orientation identification. For a 200^2 pixel scan this required some 40 min scanning time. The culminated dwell time was observed to give significant contamination levels, meaning that additional scans from the same specimen area were deteriorated.

- Precession Angle (φ): should ideally be as small as possible while recording a significant amount of reflections maintaining strong intensities. It was found that

a φ below 0.5° lost many of the precipitate reflections required for high reliability indexing.

- Camera Length (l_c): only needing the inner DP region for full orientation identification should render the ideal l_c as large as possible, thus giving the maximum of information within this region. However, it was found that the SPED scan setup lost electrons through the projector lens system with $l_c > 50$ cm. Using $l_c = 30$ cm gave sufficent intensity while retaining a bare minimum of DP pixels yielding reliable orientational mappings.

- Step Length (l_s): should be chosen as small as possible, set in conjunction with the obtained/estimated spot size. 0.64 nm is the smallest obtainable (software limit), and adjustments are made in integer multiples of this minimum step size.

- Precession Frequency (f): was kept fixed at 100 Hz. Could possibly be set to a integer multiple of known noise frequencies if these are present, e.g. scan noise, magnetic fields or external lighting which cannot be removed.

One should be very thorough in the SPED setup alignment procedure, particularly with height adjustments. It was found that a focus shift of ≈ 1 μm occurs when a 1° precession is switched on. With precession, the specimen image becomes a blur, and therefore one cannot use this in order to adjust the height back into focus. It is suggested to rather shift the height using a focused probe in image mode recorded on the external CCD camera, aiming to converge the spot to a disc as small as possible. In the case of running SPED scans on a very small specimen area, such as the scan of figure 4.21, one should do the height adjustment on a nearby area, not exposing the sought scan region. Al is highly sensitive to the high current in the focused probe in the NBD-mode, and ideally the exposure on the scan region should be due to the scan run only. Repeating scans on such small regions was found to give C-contaminated data sets of little value.

5.4.1 T-particle results

The rotation-twinned substructure of these dispersoids exhibits a quasi-crystalline, 10-fold symmetry. The morphologies of the dispersoids are rods, extending along the $\langle 001 \rangle_{\mathrm{Al}}$ directions. They are important for the control of Al grain sizes, exhibiting high thermal stabilities. These particles have higher melting points than the surrounding material, and will therefore always be coexisting with precipitates in Al alloys in normal operation temperatures.

The orientational maps of figures 4.21 and 4.23 are seen to achieve good results, as verified by looking at the HRTEM images and the reliability multiplied mappings. The misorientation plots of figure 4.24 show excellent agreement with the expected 36 ° misorientation of the 10-fold, fan-shaped structure in the T-particles [34]. The mapping of 4.21 (b) has a high reliability, as confirmed by the misorientation plot 4.24 (c), showing

near equal orientation angles, pixel by pixel over the full indicated line. The slight underestimate of $\approx 0.5^\circ$ is assumed to be only due to the precision of the T-particle template bank used in ASTAR Index. A higher template bank precision would most likely give an even more accurate determination, at the cost of added processing time (some 30 min was needed in this indexing). Obtaining this accuracy on a ≈ 50 nm dispersoid is an impressive and valuable achievement.

It is seen from figure 4.26 that the BSS component decomposition acting on the dispersoid data sets achieve reliable component patterns, picking out individual orientations indicated by the map of figure 4.23 (b). The highlighted regions of these component patterns correspond with regions of equal orientation seen in the orientational map.

This was achieved using a cropped PED pattern stack seen in figure 3.5. Both efficiency and reliability are increased by cropping out the inner DP region as compared to using the full 144^2 pixels DPs. This is due to the high intensity of Al reflections in the recorded DPs. The ASTAR Index software will put high priority in fitting the specified pattern banks to these reflections. This yields a poorer reliability in precipitate phase indexing. Therefore, removing these reflections from the PED patterns was deemed necessary. The method achieves high reliabilities due to the dense DP formed by the large unit cell of these dispersoids interior to these reflections. However, pre-processing the pattern stack by masking out the Al reflections was found to give reasonably reliable mappings of small regions of T1- and θ'-phases as well. For these phases, the bulk of reflections are placed outside of the inner Al reflections spots, and hence reliable indexing needs to take into account reflections from a larger PED pattern area.

Cropping out the region interior to the Al reflections necessarily means that the Al matrix orientation is not indexed. This is the reason as to why the orientational mappings of figures 4.21 and 4.23 show a non-systematical tiling of blue and green pixels in the regions exterior to the dispersoids (i.e. the surrounding Al matrix). The software tries to match the PED patterns from the Al matrix to those of S-precipitates and T-particles, which yields inconclusive matching, seen as this seemingly random tiling.

5.4.1.1 Qualitative discussion on dispersoid scan resolution

The orientational mapping of the ≈ 50 nm dispersoid seen in figure 4.21 is verifed to achieve sufficient resolution for reliable determination of the S-phase and T-particle 'fan-structure' orientations. This scan was acquired using: $s = 0.5$ nm, $\varphi = 0.5^\circ$, $\alpha = 0.83$ mrad, $l_\mathrm{s} = 0.64$ nm and 200^2 pixels were used to sample the area. By running a scan using an unprecessed spot size of 0.5 nm, and an applied step size of 0.64 nm, one is presumably using a step size that is smaller than the effective precessed (and transmitted) probe extent. This would lead to a certain degree of oversampling. It would be of interest to, at least qualitatively, estimate what the approximate resolution regime is. This will be guided by the system sketch of figure 5.3.

There are several factors that affect the achieved resolution. The full procedure for estimating important factors such as the obtained probe size as a function of different α and φ angles, requires a thorough analysis which was beyond the scope of this thesis.

The following discussion will therefore merely use qualitative estimates such as simple geometric relations, and be based on reports on similar systems having dealt with these matters.

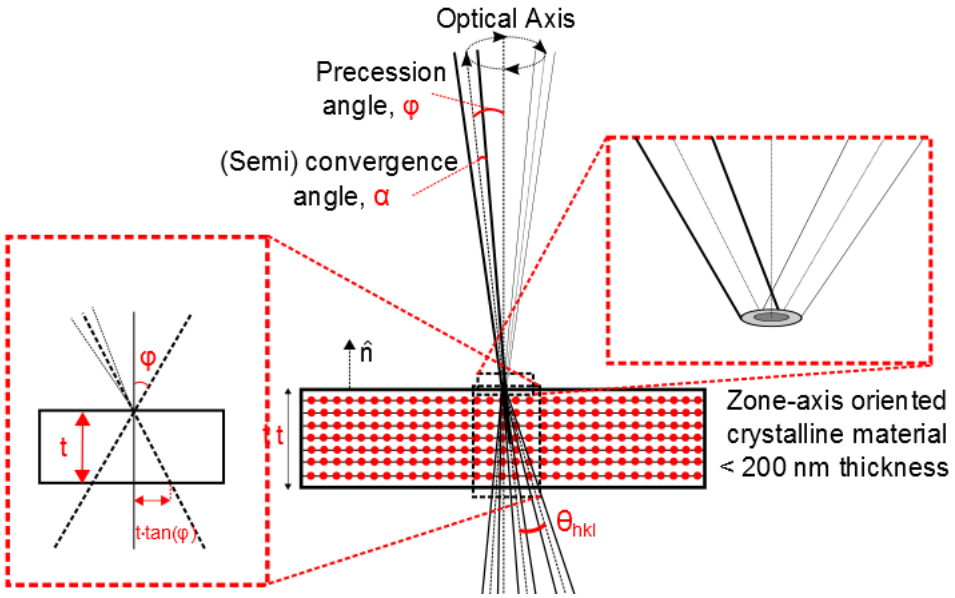

Figure 5.3: Sketch of the probe estimation geometry in the PED-setup. Right insert: increased probe disc as a result of the precessing motion on the specimen plane. Dark grey disc indicates un-precessed spot size. Left insert: probe expansion through the specimen thickness. Angles have been exaggerated for clarity.

Firstly, the NBD-probe impinging onto the specimen top plane is ≈ 0.5 nm in diameter, i.e. the diameter of the full width at half maximum (FWHM) probe intensity distribution. As indicated by the right insert of figure 5.3, by introducing a finite φ, the obtained effective probe size incident on the specimen will necessarily increase in size, indicated by the light grey disc relative to the (un-precessed) dark grey one. This is due to imperfections in the system setup such as lens aberrations, hardware synchronization, etc. In addition, the effective spot size radius as determined by α, will also affect this expansion. In order to determine this increase, one should systematically adjust the two angles and subsequently record the resulting spot size on a CCD camera, with no specimen in the beam path.

How localized the electron probe is when propagating through the crystal is a complex quantum mechanical problem. The probe samples the crystal potential $V(\mathbf{r})$, and especially for ZA orientations, the probe amplitude distribution, $|\psi(\mathbf{r})|^2$, is highest on the s-orbitals of the atoms along the column in the beam direction, described through the channeling effect [46]. This effect is mentioned here, because the PED-setup φ-angle makes the beam deviate from ZA orientation, hence meaning that channeling effects are somewhat reduced. This further means that the probe is less localized, and effectively samples a larger specimen volume. Furthermore, the effect depends on the ZA in ques-

tion, i.e. it differs for the $[001]_{Al}$ and $[111]_{Al}$ ZA. For example, in fcc-materials such as Al, the channeling effect is most pronounced for the $[011]_{Al}$ axis, followed by $[112]_{Al}$, $[001]_{Al}$ and $[111]_{Al}$, which shows the weakest effect [47]. The precession angles are typically < 1°, so the effect should not exceed the Å-regime.

With a parallel beam incident on the specimen plane, the sampled volume traces out a cylinder (neglecting diffracted beams). Using a precessing probe, the traced volume becomes a hollow cone. As the left insert of figure 5.3 shows, with the beam precession triangle vertex at the top of the specimen plane, the probe will trace out a cone with a diameter $2t \cdot \tan\varphi$, when propagating through the specimen of thickness t. Using the stated φ, and approximating the specimen thickness as 70 nm, one obtains a scanned probe cone with a diameter of $\approx$ 1.22 nm. This serves as a lowest estimate of the probe increase within the specimen due to the PED setup. Including a crude $2t \cdot \tan\alpha$ dependence, it increases to $\approx$ 1.34 nm. How this expanding hollow cone probe diameter during specimen propagation ultimately affects the obtained spatial resolution of the obtained dispersoid orientational mapping, is a more difficult problem however. It is however safe to state that if the specimen area was in fact this thick (it has not been measured), then the obtained spatial resolution will be poorer than the applied step size of 0.64 nm.

In studying strains at the nm-level in semiconductors, [48] have measured resulting spot sizes at different φ, after propagation through a Si specimen. The cited paper reports an obtained probe size of 1.8 nm with $\varphi = 0.25°$ and $\alpha = 2.4$ mrad after specimen propagation, using a FEI Titan Ultimate double aberration corrected TEM. This was measured by taking the FWHM diameter of the imaged probe after specimen propagation.

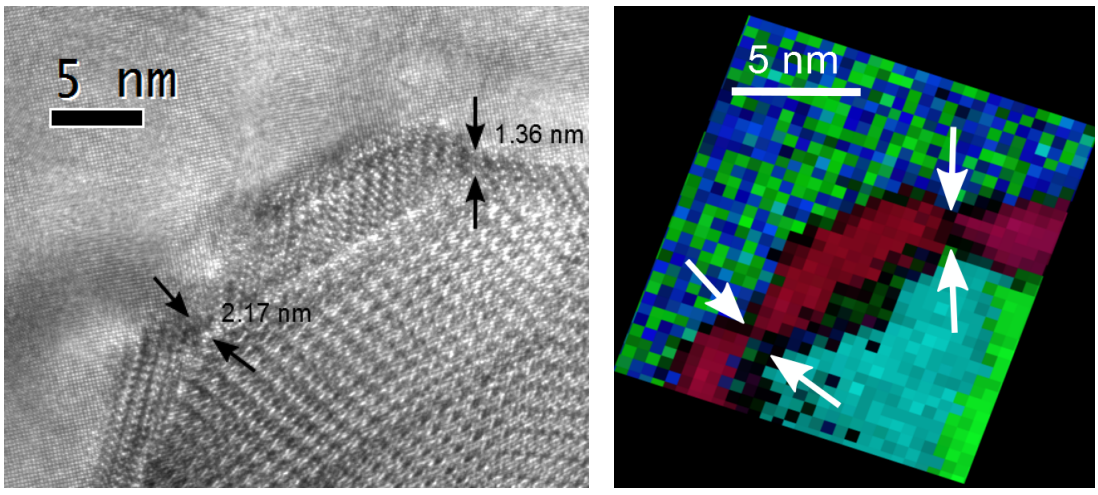

(a) (b)

Figure 5.4: (a) and (b): Marked and cropped versions of figures 4.20 and 4.21 (b) respectively. The narrow 'channels' between the S-phases nucleating on this T-particle are highlighted in each image. These narrow regions indicate the spatial resolution regime obtained in this mapping.

In [5] it was used a JEOL JEM 2200FS equipped with a FEG and an in-column Ω-filter. Here it was studied a fine-grained Palladium sample. In this paper they have also used a 10 μm CA and a spot size of 0.5 nm in a modified NBD-mode setup. They applied a $\varphi = 0.9°$. In their recorded data, they infer a maximal spatial resolution of 1 nm, or suggest a 'more readily discernible' spatial resolution of 2-3 nm.

Looking at the narrow 'channels' between nucleating S-phases in figure 5.4 (a) and (b), it is hard to argue against the observation that the orientational mapping has seemingly successfully mapped these narrow regions. It was also looked at the BSS components of the relevant T-particle 'fan', the surrounding Al matrix and the different S-phases in these regions. The loading maps showed some overlap, but further indicated that these narrow channels are in fact resolved.

Taking the previous discussion and examples into account, as well as taking a closer look on the narrow boundaries between the nucleating S-phases in figure 5.4 (a) and (b), it is inferred a maximum resolution of ≈ 1 nm in the obtained data set.

5.4.2 Evaluation of component decompositions

The last section of Ch. 4 presents several component patterns obtained through automatic BSS component decomposition of the data set acquired in the area of figure 4.25. Figures 4.27 and 4.28 show the identification of 8 out of 12 possible different orientations of the S-phase relative to the Al matrix. This is confirmed by comparing the obtained component patterns to kinematic CrystalKit matrix-precipitate DPs, using the S-phase structure embedded in an Al matrix. The patterns show a decisive agreement, only differing in additions of symmetrically placed reflections in the BSS component patterns. These added reflections adhering to the DP symmetry, are not thought to be falsely included from a different precipitate's reflections, but rather due to dynamical effects, and most likely double-diffractions.

This result, i.e. to achieve reliable matrix-precipitate orientations of phases even < 5 nm in extent, from larger overview scans (here 575 nm^2), is an impressive feat which has no CTEM technique equivalent. This provides valuable information which one must usually apply high magnification HAADF-STEM with aberration corrected instruments, or repeated use of high-magnification SAED on individual phases, to achieve. This could allow identification of interesting orientational relationships occurring throughout the material. It might for instance reveal that there are only certain allowed orientational relationships between T-particles and S-phases, and revealing this in a scan taken from an area as large as the full Al grain size. This is achieved in the identification of the different S-phase orientations nucleating on the upper right dispersoid in the components of figure 4.27, seen up-close in figure 4.26.

This also opens for acquiring refined precipitate statistics. The technique can differentiate between precipitates approximately ≥ 4 nm in size from areas as large as 1 μm^2. This 'precipitate-to-area-size relation' can obviously be adjusted, if one seeks information from larger or smaller precipitates. Lateral dimensions below 2 nm is seen as an approximate lower limit. This can contribute to acquire statistics from precipitates which

are hard to differentiate from overview images, e.g. the case for several coexisting 6xxx series (Al-Mg-Si) needle-shaped precipitates.

This adds to the library of valuable information obtainable from a single SPED data set. Furthermore, this information is obtained through a semi-automated procedure, only requiring a 'cherry-picking' of the components deemed most reliable, or 'physically meaningful', in the component pattern stack.

An adverse effect apparent in these loading maps, which is also present in the presented VDF images, is the significant after-glow due to the slow reset of the fluorescent screen. The intensity appears to be smeared out in the scan direction. The effect becomes more pronounced the stronger the imaged phase diffracts. This is seen to be the case for the S-phases and dispersoids, both extending into the plane, throughout the full matrix thickness. This effect can be reduced by acquiring fluorescent plates specialized in fast resetting times.

The additional BSS loading maps presented in figure 4.29 show further aspects of interest obtained from the BSS component pattern stack. The upper two components show even more impressive Ω-precipitate images than those of figure 4.14 (c) and (d), exhibiting much better signal-to-noise ratios. Some of these precipitates are as small as 3-5 nm, yet extracted as clear features in these images.

The center left loading map of figure 4.29, showing the specimen boundary towards vacuum, highlights an additional important aspect in microstructure analysis of materials. The associated component pattern has picked out an Al reflection significantly displaced relative to its bulk, 'relaxed' position. This is due to an associated strong strain in this area. This is common for boundaries towards vacuum, which tend to significantly bend the Al matrix. The use of PED in measurements of strain maps, obtained in a manner similar to the presented orientational maps of T-particles, is of high value in the development of novel materials, e.g. in the semiconductor industry [49]. Strain is also of high interest in Al alloys [50]. This case of interest was however not pursued further in this thesis, mainly due to the observed, adverse impact of strong after-glow in the SPED data. It was obtained many more loading maps highlighting strongly strained regions in this specimen area.

The remaining three loading maps of figure 4.29 sucessfully pick out the remaining three dispersoids of this specimen area, each having different orientations relative to the surrounding matrix. Combined with the preceding loading maps and component patterns of this section, this yields an impressive feat of component identification through a reliable, semi-automatic procedure. In total this has identified every major phase present in the area of figure 4.25. Furthermore, all this data was obtained from a single SPED scan run taking $\approx$ 30 min time.

The other ZA SPED scans acquired in the experimental work of this thesis are of similar quality, and have all yielded equally impressive component decompositions, orientational mappings, and virtual images. The large amount of obtained data is however not presented in its full extent in order to keep the thesis within reasonable bounds.

5.5 Future Outlook of SPED

The range of presented results, whose quality have been discussed in the preceding sections, show that SPED has been successfully applied in studying the multiphase nature of Al alloys. It has also been shown that although SPED is a time intensive data recording technique, the power of extracting numerous virtual images, orientational mappings and data decompositions by post-analysis significantly shifts the time efficiency back in favor of SPED. In some sense, one is running an extended TEM session with doing 'imaging' and finding DPs of interest ex post facto .

With the advent of more powerful TEM hardware; including improved detectors, faster cameras, etc., the amount of data obtainable in future TEM work is inevitably going to increase exponentially. As is very recently being applied; SPED can be combined with the addition of a tilt-series to form scanning precession electron tomography (SPET) [37], or combined with the recording of EDX data at each probe position. This introduces additional dimensionality in SPED data, which further requires improved computer hardware to process, and better software to extract increased information in these added dimensionalities. Powerful open-source software such as HyperSpy is following alongside this development, and will become increasingly important in the future of TEM development.

All of these aspects are highly intriguing. It could be possible to obtain detailed 3D real- and reciprocal space information, with the addition of a 1-to-1 correspondence in EDS mappings and PED pixels, at each point of the of the ZA SPE(T/D) scan. If one further is able to process and extract this information efficiently, one would obtain very detailed and unique information on the microstructure of studied specimens. Applying these techniques in studying Al, could provide the key to the future development of this widely applied material.

Chapter 6

Conclusion

The technique of SPED has been proved highly valuable in studying the multiphase nature of 2xxx series Al alloys. The technique yielded high quality data sets from several low-order ZAs in the two alloys studied throughout this thesis. As presented, subsequent data processing of the acquired large amounts of data enabled:

- Formation of high quality virtual images
- Detailed specimen area phase mappings obtained semi-automatically
- High spatial resolution orientational mappings of T-particles

Data processing of multidimensional data sets is conveniently facilitated by the open-source Python library HyperSpy. Its virtual aperture functionality allowed easy navigation in the large PED pattern stacks. This enabled formation of virtual images highlighting all separate orientations of individual main strengthening precipitates in the two Al alloys studied. This encompassed the different orientations of θ'- and T1-phases present in alloy CL, and correspondingly for the Ω- and S-phases in alloy MCA. In many aspects, these obtained images are of higher quality as compared to corresponding CTEM techniques. Their main improvement is to exhibit sharper, more consistent contrast, as well as a higher signal-to-noise ratio.

Applied 'machine learning' results obtained through the BSS algorithm, identified eight different matrix-precipitate orientations of S-phases. It was also obtained additional valuable loading maps, providing a detailed phase mapping of a $[001]_{Al}$ ZA oriented grain in alloy MCA. These results were obtained by a semi-automatic method, which only manual procedure step involved a component picking of the loading maps deemed most physically meaningful. Microstructural features as small as 2-3 nm in extent are reliably indentified in 576 nm^2 area scans, which has taken some 30 min to acquire.

Furthermore, ASTAR indexing of pre-processed data sets achieved high spatial resolution orientational mappings of T-particles, showing high reliability indices. This enabled the experimental confirmation of the 10-fold rotation-twinned substructure of these Al-Cu-(Mn,Fe) dispersoids. The obtained mappings show indication of a spatial resolution approaching 1 nm.

Chapter 7

Further Work

Several GBs of high quality SPED data have been acquired in the experimental work of this thesis. Most processing of this data required a minimum of 85% reduction in data sizes. This either meant that one had to narrow the focus to certain areas of the scan, or that a large discarding of PED pattern data had to be made. With the advent of more powerful computer hardware, the same procedures applied throughout this thesis can be used on a larger amount of the data recorded. Being able to process larger amounts of this data will result in much improved component decompositions, and orientational mappings being obtainable over a larger scanned area extent.

Being of high importance in industrial Al alloys, pursuing the possibility of obtaining strain maps in the acquired SPED data would be very interesting. In principle, obtaining strain maps should be somewhat similar to the computation of orientational maps. It requires the comparison of a high quality DP stack acquired in an area of interest with a bulk, 'relaxed' reference DP of the same phase, e.g. the Al matrix. The obtained strain map quality might however be somewhat deteriorated due to the observed adverse effect of strong after-glow in the SPED data.

Furthermore, it would be of interest to attempt scanning precession electron tomography (SPET), by acquiring SPED data in a tilt-series using a dedicated tomography holder, which is available at the author's research group. This technique has been applied very recently on a Ni-based super-alloy [37], giving a detailed 3D reconstruction in both real- and reciprocal space. This could for instance highlight new aspects in precipitates existing in important industrial Al alloys. Atomic scale 3D information on Al alloys is mainly being obtained by the use of atom-probe tomography (APT). This is a destructive technique, which gives high spatial resolution information on atomic distributions, e.g. on PFZs and early stage precipitation. SPET on the other hand is non-destructive, and its 3D real- and reciprocal space information could provide complementary information on precipitates, e.g. on morphologies and interplanar misfits to the surrounding Al matrix.

Bibliography

[1] S. J. Kang et al. Determination of interfacial atomic structure, misfits and energetics of Ω phase in Al-Cu-Mg-Ag alloy. *Acta Materialia*, 81:501–511, 2014.

[2] K. Knowles and W. Stobbs. The structure of {111} age-hardening precipitates in Al-Cu-Mg-Ag alloys. *Acta Crystallography*, 44:207, 1988.

[3] C. Dwyer et al. Combined electron beam imaging and ab initio modeling of T1 precipitates in Al–Li–Cu alloys. *Applied Physics Letters*, 98, 2011. id:201909.

[4] H. W. Zandbergen et al. Structure determination of Mg_5Si_6 particles in Al by dynamic electron diffraction studies. *Science*, 277:1221–1225, 1997.

[5] P. Moeck et al. High spatial reolution semi-automatic crystallite orientation and phase mapping of nanocrystals in transmission electron microscopes. *Cryst. Res. Technol.*, 46:589–606, 2011.

[6] Royal Society of Chemistry - Periodic Table - Aluminium. http://www.rsc.org/periodic-table/element/13/aluminium. [Accessed: 01.11.2015].

[7] Aluminium Design - Properties of Aluminium. http://www.aluminiumdesign.net/why-aluminium/properties-of-aluminium/. [Accessed: 01.12.2015].

[8] Aluminium Leader - Aluminium History. http://www.aluminiumleader.com/history/industry_history/. [Accessed: 20.11.2015].

[9] ACS - Production of Aluminium - The Hall-Héroult process. http://www.acs.org/content/acs/en/education/whatischemistry/landmarks/aluminumprocess.html. [Accessed: 25.11.2015].

[10] Hydro - Aluminium life cycle. http://www.hydro.com/en/About-aluminium/Aluminium-life-cycle/. [Accessed: 25.10.2015].

[11] Aluminium Matter - Aluminium v Steel - Stress-Strain behaviour. http://aluminium.matter.org.uk/content/html/eng/default.asp?catid=217&pageid=2144417131. [Accessed: 28.11.2015].

[12] ESABNA - Understanding the Aluminium Alloy designation system. http://www.esabna.com/us/en/education/blog/understanding-the-aluminum-alloy-designationsystem.cfm. [Accessed: 28.11.2015].

[13] Constellium - Aluminium Properties and Applications. http://www.constellium.com/technology-center/aluminium-alloy-properties. [Accessed: 05.11.2015].

[14] E.J. Samuelsen. *Materials physics: Structure, Diffaction, Imaging and Spectroscopy*. NTNU-trykk, 2nd edition, 2006.

[15] P. C. Hemmer. *Faste Stoffers Fysikk*. Tapir Akademisk Forlag, 2nd edition, 1987.

[16] C. Kittel. *Introduction to Solid State Physics*. John Wiley & Sons, 8th edition, 1975.

[17] J.D. Verhoeven. *Fundamentals of Physical Metallurgy*. John Wiley & Sons, 2nd edition, 1975.

[18] S. Wenner. *Transmission Electron Microscopy and Muon spin relaxation studies of precipitation in Al-Mg-Si alloys*. NTNU-trykk, 2014. Doctoral thesis, NTNU, Trondheim, Norway.

[19] J.T. Staley. Proc. 3rd Int. Conf. on Aluminium alloys (ICAA3), (ed. L. Arnberg, O. Lohne, E. Nes and N. Ryum). pages 107–143, 1992.

[20] S.C. Wang and M. J. Starink. Precipitates and intermetallic phases in precipitation hardening Al-Cu-Mg-(Li) based alloys. *Int. Mater. Rev.*, 50:193–215, 2005.

[21] E. A. Starke and J.T. Staley. Application of modern aluminum alloys to aircraft. *Prog. Aerospace Sci.*, 32:131–172, 1996.

[22] J. A. Taylor, B. A. Parker, and I. J. Polmear. Precipitation in Al-Cu-Mg-Ag casting alloy. *Met. Sci.*, 12:478–482, 1978.

[23] L. Bourgeois et al. Structure and energetics of the coherent interface between the θ‘ precipitate phase and aluminium in Al-Cu. *Acta Materialia*, 59:7043–7050, 2011.

[24] C. J. Humphreys. The scattering of fast electrons by crystals. *Reports on Progress in Physics*, 42:1825–1887, 1979.

[25] D.B. Williams and C.B. Carter. *Transmission Electron Microscopy: A textbook for materials science. Part 1: Basics*. Springer, 2009.

[26] L. Reimer and H. Kohl. *Transmission Electron Microscopy: Physics of Image Formation*. Springer, 2008.

[27] D.B. Williams and C.B. Carter. *Transmission Electron Microscopy: A textbook for materials science. Part 2: Diffraction*. Springer, 2009.

[28] R. Erni. *Aberration-corrected imaging in transmission electron microscopy*. Imperial College Press, 2010.

[29] P.A. Midgley and A.S. Eggeman. Precession electron diffraction - a topical review. *IUCr*, 2:126–136, 2014.

[30] R. Vincent and P.A. Midgley. Double conical beam-rocking system for measurement of integrated electron diffraction intensities. *Ultramicroscopy*, 53(3):271 – 282, 1994.

[31] American Elements. https://www.americanelements.com/al.html. [Accessed: 29.11.2015].

[32] J. K. Sunde. *Precipitation of Several Coexisting Strengthening Phases in Aluminium Alloys*. 2015. Project Work, NTNU, Trondheim, Norway.

[33] NanoMEGAS. http://www.nanomegas.com/ [Accessed: 18.01.2016].

[34] Z. Q. Feng et al. Crystal substructures of the rotation-twinned T ($Al_{20}Cu_2Mn_3$) phase in 2024 aluminium alloy. *J. of Alloys and Comp.*, 583:445–451, 2014.

[35] F. de la Peña et al. Hyperspy - 0.8.4, 2016. http://hyperspy.org/ [Accessed: 20.03.2016].

[36] Python Software Foundation. Python - 3.5.1, 2016. https://www.python.org/ [Accessed: 10.01.2016].

[37] A. S. Eggeman et al. Scanning precession electron tomography for three-dimensional nanoscale orientation imaging and crystallographic analysis. *Nat. Commun.*, 6:7267, 2015.

[38] S.C. Wang, C.Z. Li, and W.M. Bian. The microstructure determination of the dispersoid phases in 2024 aluminium alloys. *Chin. J. Mech.*, 26:16–19, 1990.

[39] Gatan. http://www.gatan.com/ [Accessed: 02.10.2015].

[40] CrystalKit. http://www.totalresolution.com/CrystalKit.html [Accessed: 19.01.2016].

[41] J.M. Silcock, T.J. Heal, and H.K. Hardy. Structural ageing characteristics of binary aluminium-copper alloys. *J. Inst. Met.*, 82:239, 1953.

[42] H. Perlitz and A. Westgren. The crystal structure of Al_2CuMg. *Arkiv for Kemi, Mineralogi och Geologi*, 16B:13, 1943.

[43] A. Guinier. Le mécanisme de la précipitation dans un cristal de solution solide métallique. - cas des systèmes aluminium-cuivre et aluminium-argent. *J. Phys. Radium*, 8:124–136, 1942.

[44] A. Meetsma, J.L. deBoer, and S. van Smaalen. Refinement of the crystal-structure of tetragonal Al_2Cu. *J. Solid State Chem.*, 83:370–372, 1989.

[45] R. Bonnet. Disorientation between any two lattices. *Acta Crystallography*, 36A:116–122, 1980.

[46] S. J. Pennycook. Structure determination through Z-contrast microscopy. *Adv. in Imaging and Electron Physics*, 123:173–206, 2002.

[47] J.L. Whitton. Channeling in Gold. *Canadian Journ. of Phys.*, 45:67–149, 1967.

[48] D. Cooper, N. Bernier, and J.L. Rouvière. Combining 2 nm Spatial Resolution and 0.02% Precision for Deformation Mapping of Semiconductor Specimens in a Transmission Electron Microscope by Precession Electron Diffraction. *Nano Letters*, 15:5289–5294, 2015.

[49] J. L. Rouviere et al. Improved strain pecision with high spatial resolution using nanobeam precession electron diffraction. *Applied Physics Letters*, 103:445–451, 2013.

[50] S. Wenner and R. Holmestad. Accurately measured precipitate-matrix misfit in an Al-Mg-Si alloy by electron microscopy. *Scripta Materialia*, 118:5–8, 2016.

Appendix A

Additional SPED Data Sets

This appendix contains additional SPED data recorded in other ZAs of interest in the two alloys CL and MCA. First presented in this appendix are several simulated DPs of ZA oriented Al matrices containing the aforementioned T1-, θ'-, Ω- and S-precipitates. These are succeeded by the total summed PED pattern stacks in the SPED data sets recorded near the same ZAs.

Then, using the simulated DPs to identify the components of these summed PED pattern stacks, several VDF images highlighting individual precipitates as inclined relative to the corresponding ZAs are presented. The individual VDF images are then combined in constructed RGB images highlighting the multi-component nature of these Al alloys. The obtained results are presented systematically for each ZA of interest separately.

Figures A.1 through A.6 shows simulated total, and total individual, DPs from the $[112]_{Al}$ and $[013]_{Al}$ ZAs in alloy CL and the $[111]_{Al}$ ZA in alloy MCA.

Figure A.7 shows the total summed PED pattern stacks acquired from these three Al ZAs. Following, figures A.8 through A.11 show a combination of BSS loading maps and formed VDF images of the main forming precipitates in these three ZAs sequentially.

Lastly, figure A.12 shows total RGB images formed using the preceding loading maps and VDF images.

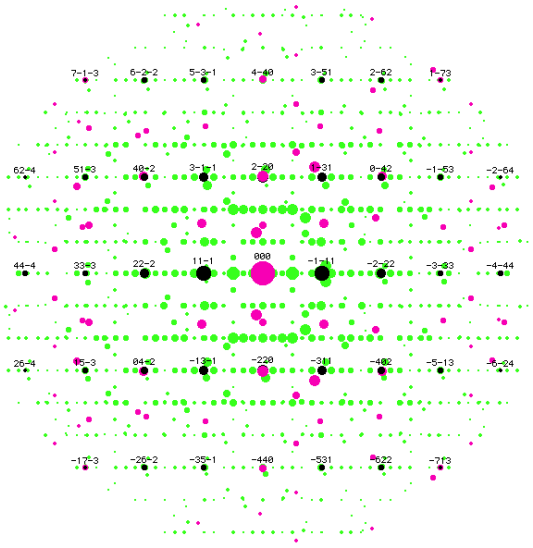

Figure A.1: Total kinematical simulated DP in the $[112]_{Al}$ ZA containing θ'- and T1-precipitates. Al reflections are shown in black with indicies, and θ'- and T1-reflections are shown in pink and green respectively. Some reflections overlap, and in this case the colour will correspond to that of the precipitate.

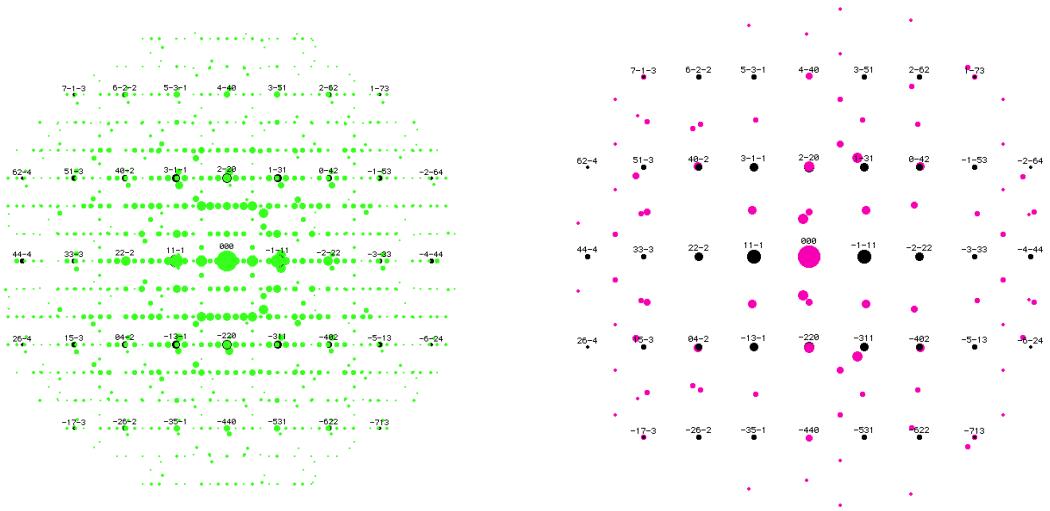

(a) (b)

Figure A.2: (a) and (b) show the total individual kinematical DP sums, including all non-equivalent matrix-precipitate orientations of T1- and θ'-precipitates relative to the surrounding Al matrix, respectively. They are both simulated in the $[112]_{Al}$ ZA. Al reflections are shown in black and indexed.

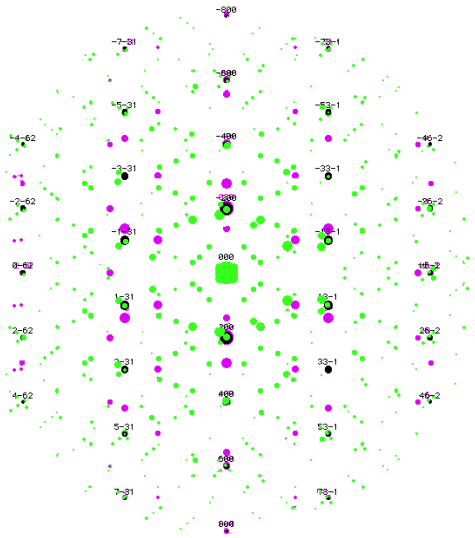

Figure A.3: Total kinematically simulated DP in the $[013]_{Al}$ ZA containing θ'- and T1-precipitates. Al reflections are shown in black with indicies, and θ'- and T1-reflections are shown in purple and green respectively. Some reflections overlap, and in this case the colour will correspond to that of the precipitate.

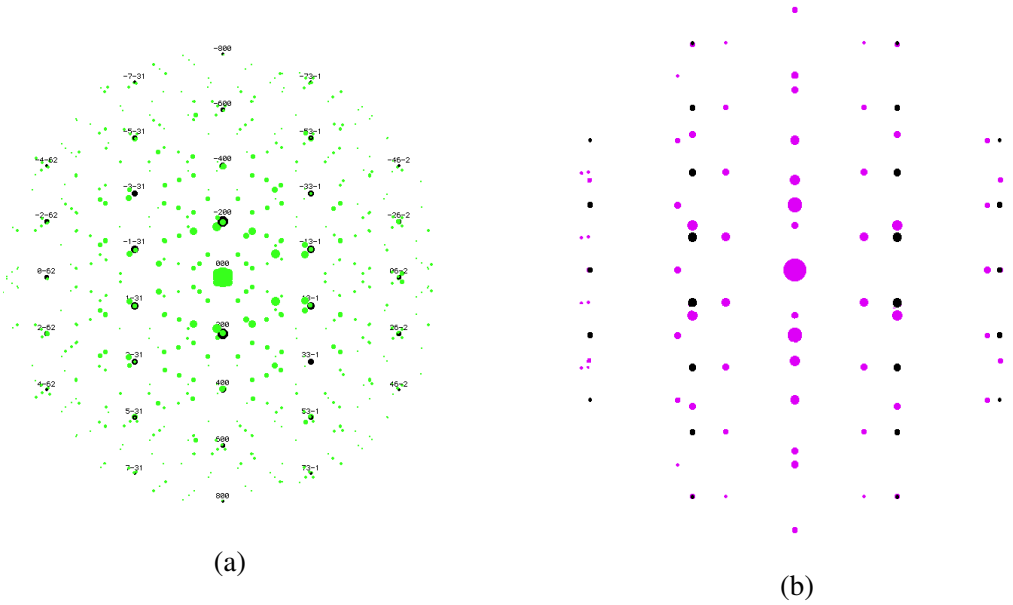

(a) (b)

Figure A.4: (a) and (b) show the total individual kinematical DP sums, including all non-equivalent matrix-precipitate orientations of T1- and θ'-precipitates relative to the surrounding Al matrix, respectively. They are both simulated in the $[013]_{Al}$ ZA. Al reflections are shown in black (and with indices in (a)).

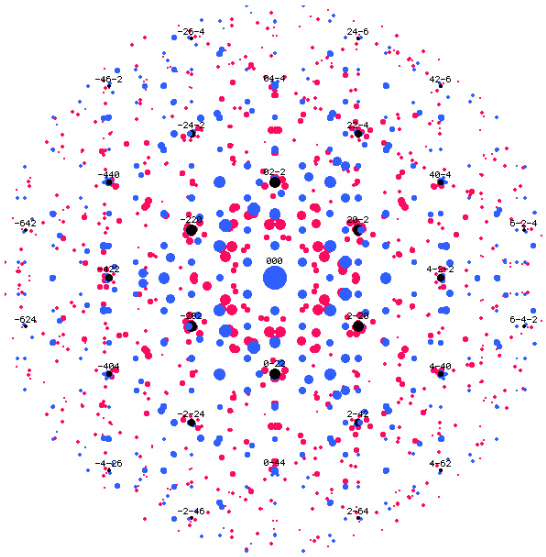

Figure A.5: Total kinematically simulated DP in the $[111]_{Al}$ ZA containing Ω- and S-precipitates. Al reflections are shown in black with indicies, and Ω- and S-reflections are shown in blue and red respectively. Some reflections overlap, and in this case the colour will correspond to that of the precipitate.

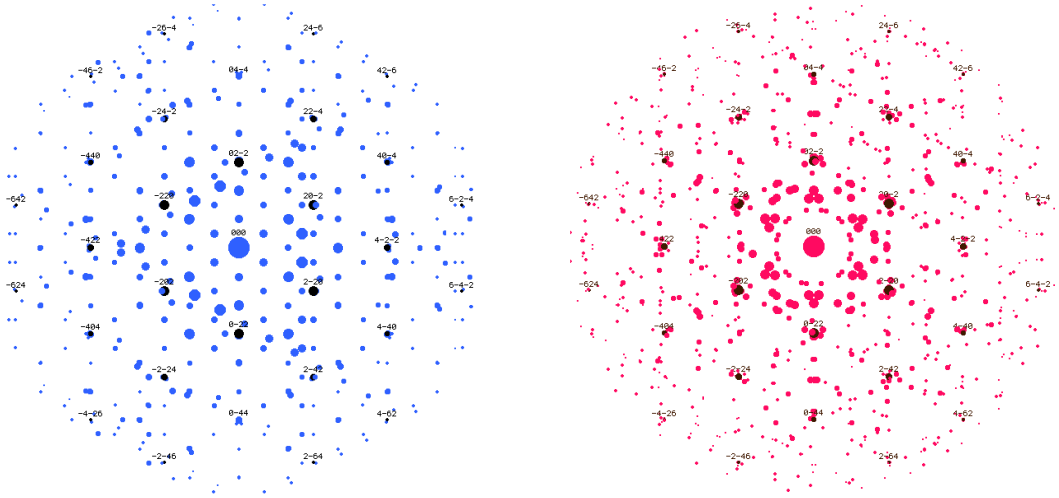

(a) (b)

Figure A.6: (a) and (b) show the total individual kinematical DP sums, including all non-equivalent matrix-precipitate orientations of Ω- and S-precipitates relative to the surrounding Al matrix, respectively. They are both simulated in the $[111]_{Al}$ ZA. Al reflections are shown in black and indexed.

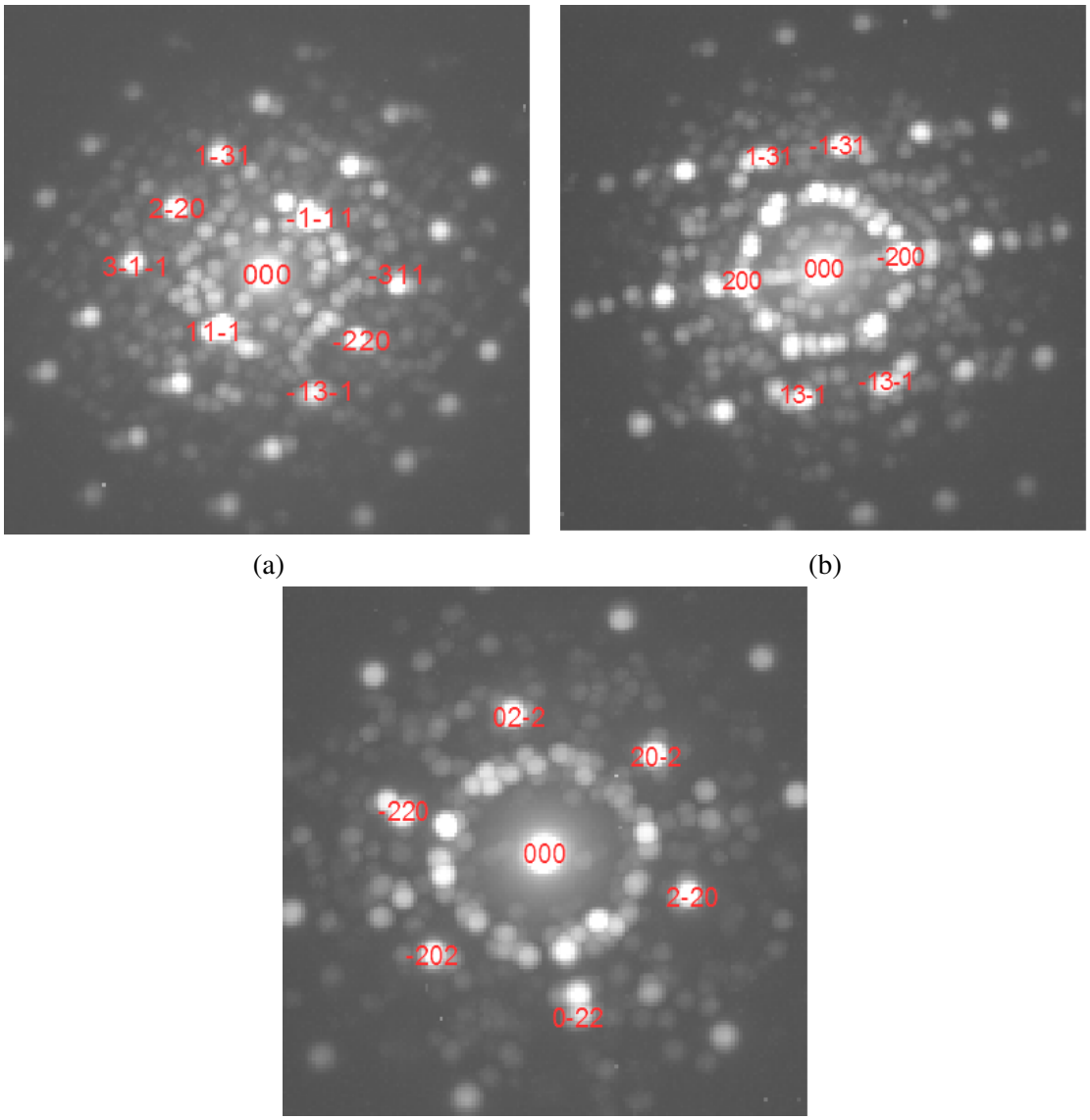

Figure A.7: (a) through (c): Total sum of all PED patterns in each SPED data set recorded near the $[112]_{Al}$ and $[013]_{Al}$ ZAs in alloy CL, and the $[111]_{Al}$ ZA in alloy MCA respectively.

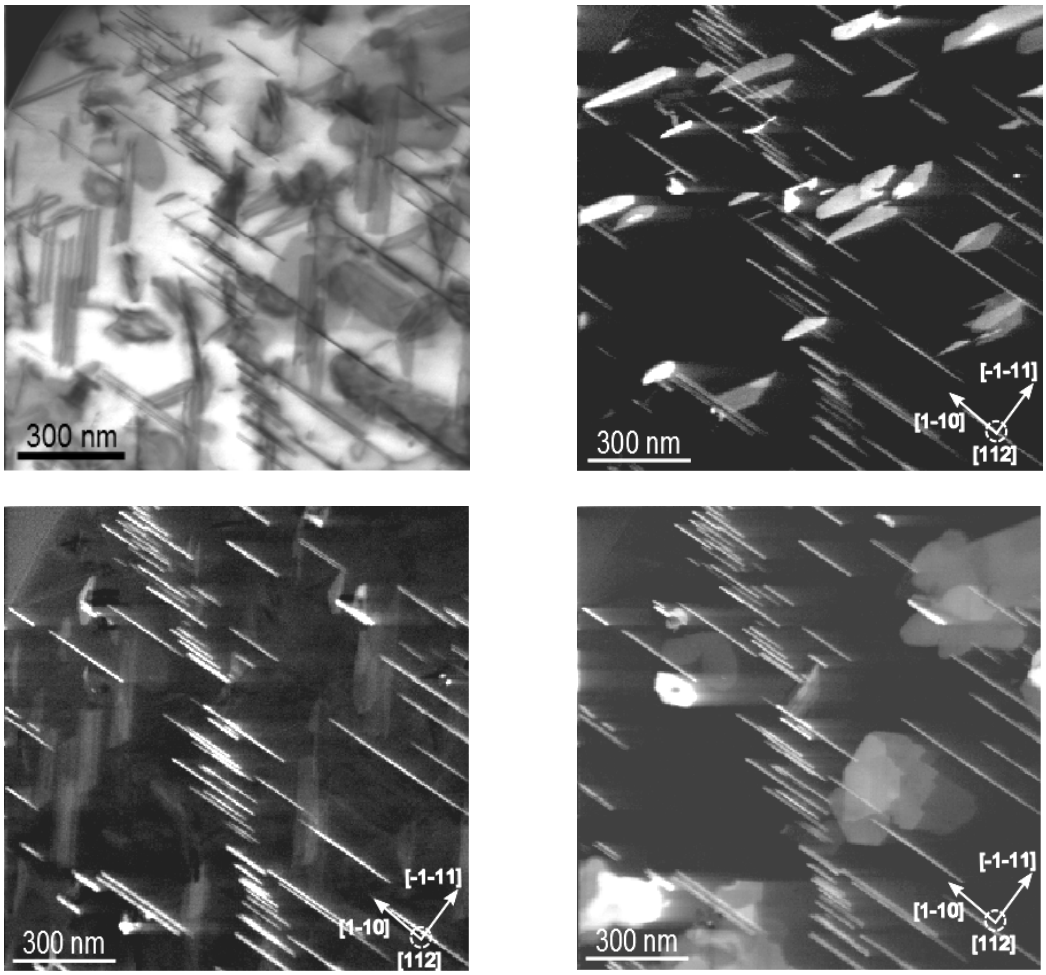

Figure A.8: VBF (a) and BSS loading maps of (b-d) T1- and (e) θ'-precipitates near the $[112]_{Al}$ ZA in the CL alloy. (a) Scanned specimen area. (b) $(111)_{Al}$ T1 precipitate plates viewed edge-on and $(-111)_{Al}$ plates. (c) $(111)_{Al}$ T1 precipitate plates viewed edge-on and $(1-11)_{Al}$ plates. (d) $(111)_{Al}$ T1 precipitate plates viewed edge-on and $(11-1)_{Al}$ plates. (e) θ'-precipitate plates forming on $\{001\}_{Al}$. The scanned area is 1.35 μm^2, using 300^2 pixels.

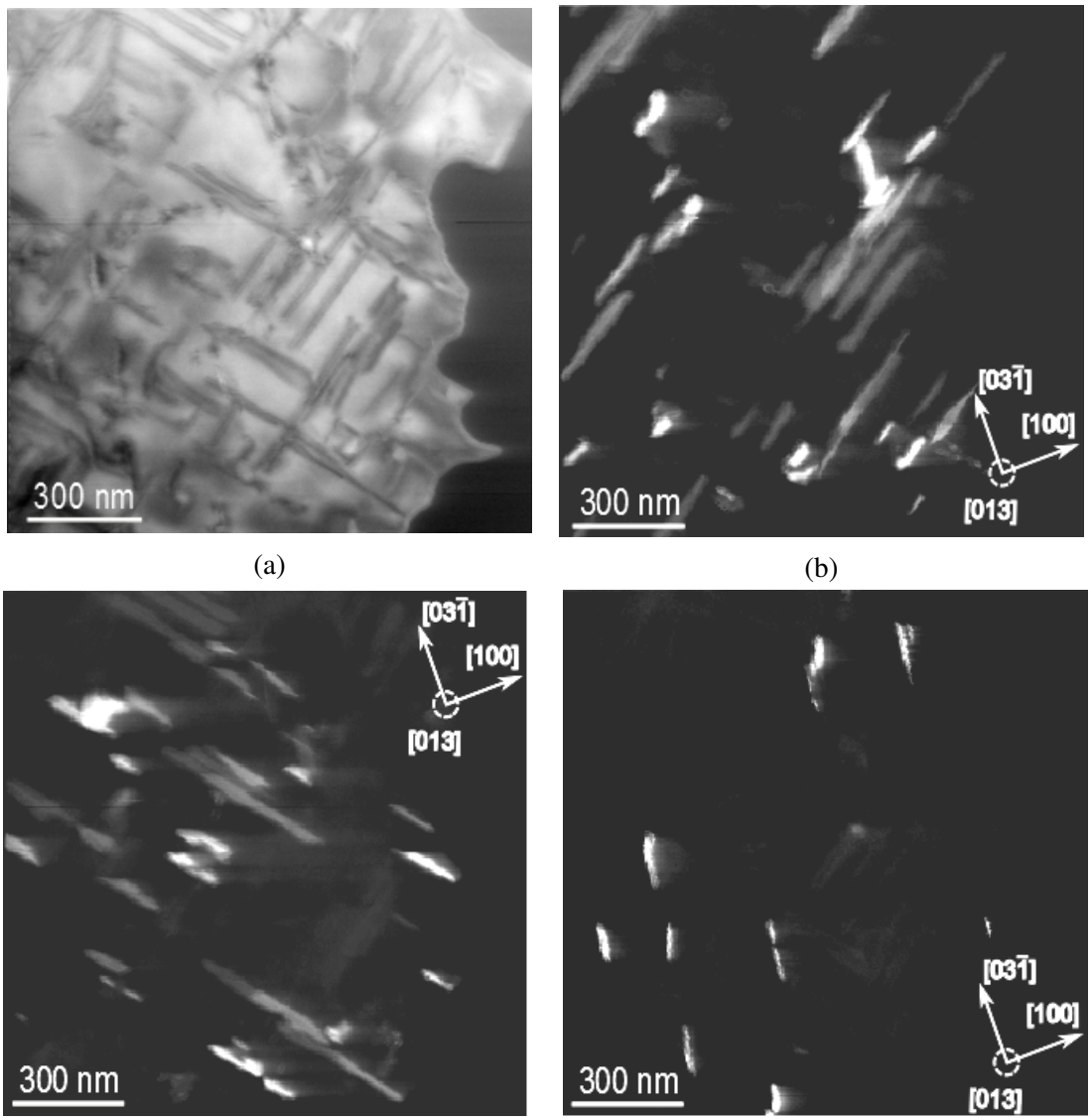

Figure A.9: (a) VBF image of the scanned specimen area near the $[013]_{Al}$ ZA in alloy CL, and (b-d) VDF images highlighting the area precipitates. (b) $(111)_{Al}$ and $(11\text{-}1)_{Al}$ T1-precipitate plates. (c) $(1\text{-}11)_{Al}$ and $(\text{-}111)_{Al}$ T1-precipitate plates. (d) $(010)_{Al}$ θ'-plates. The scanned area is 576 nm^2, using 300^2 pixels.

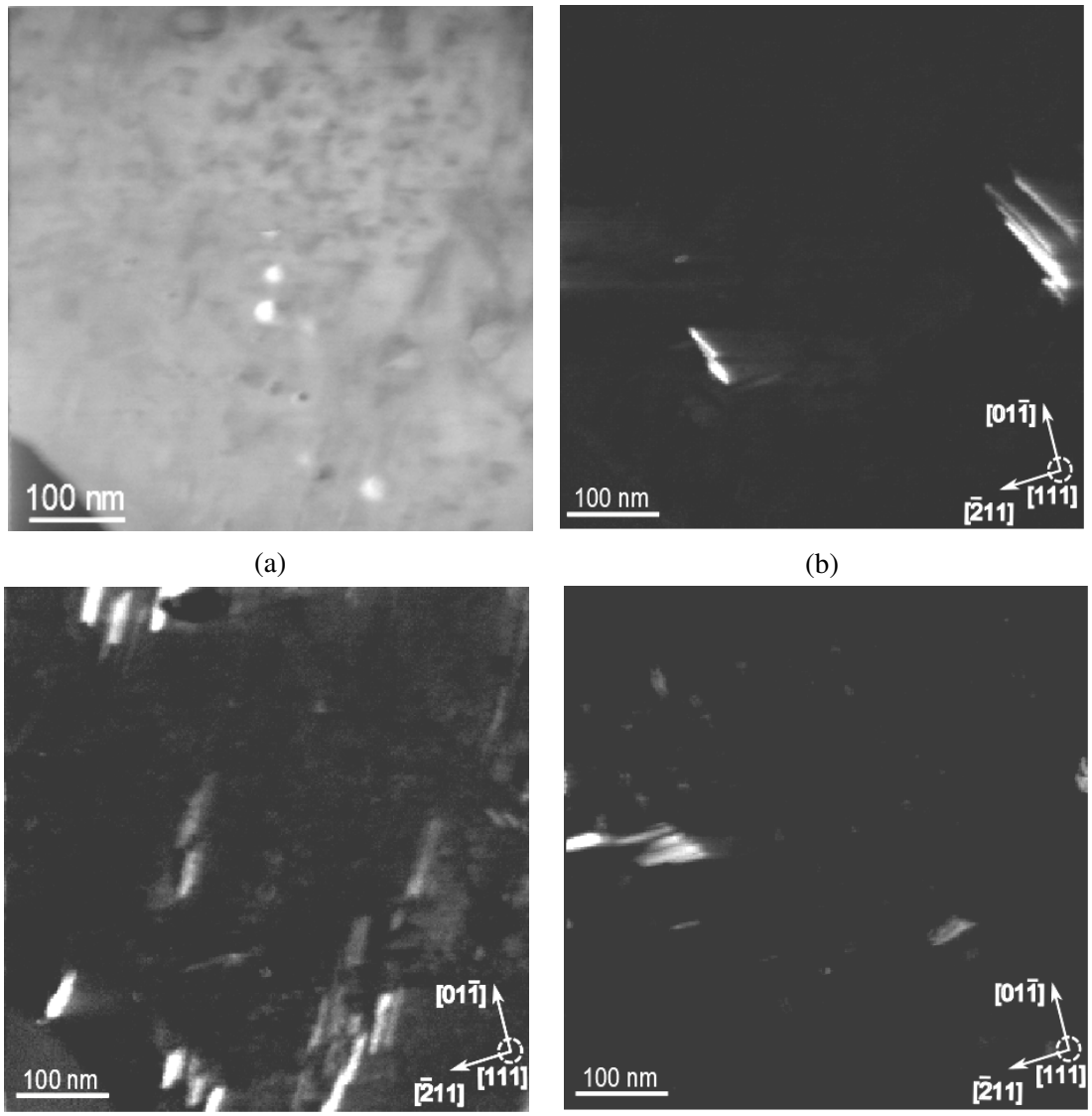

Figure A.10: (a) VBF image of the scanned specimen area near the $[111]_{Al}$ ZA in alloy MCA, and (b-d) VDF images highlighting the area precipitates. (b) S-precipitate laths elongated along $[001]_{Al}$. (c) S-precipitate laths elongated along $[010]_{Al}$. (d) S-precipitate laths elongated along $[100]_{Al}$. The scanned area is 576 nm^2, using 300^2 pixels.

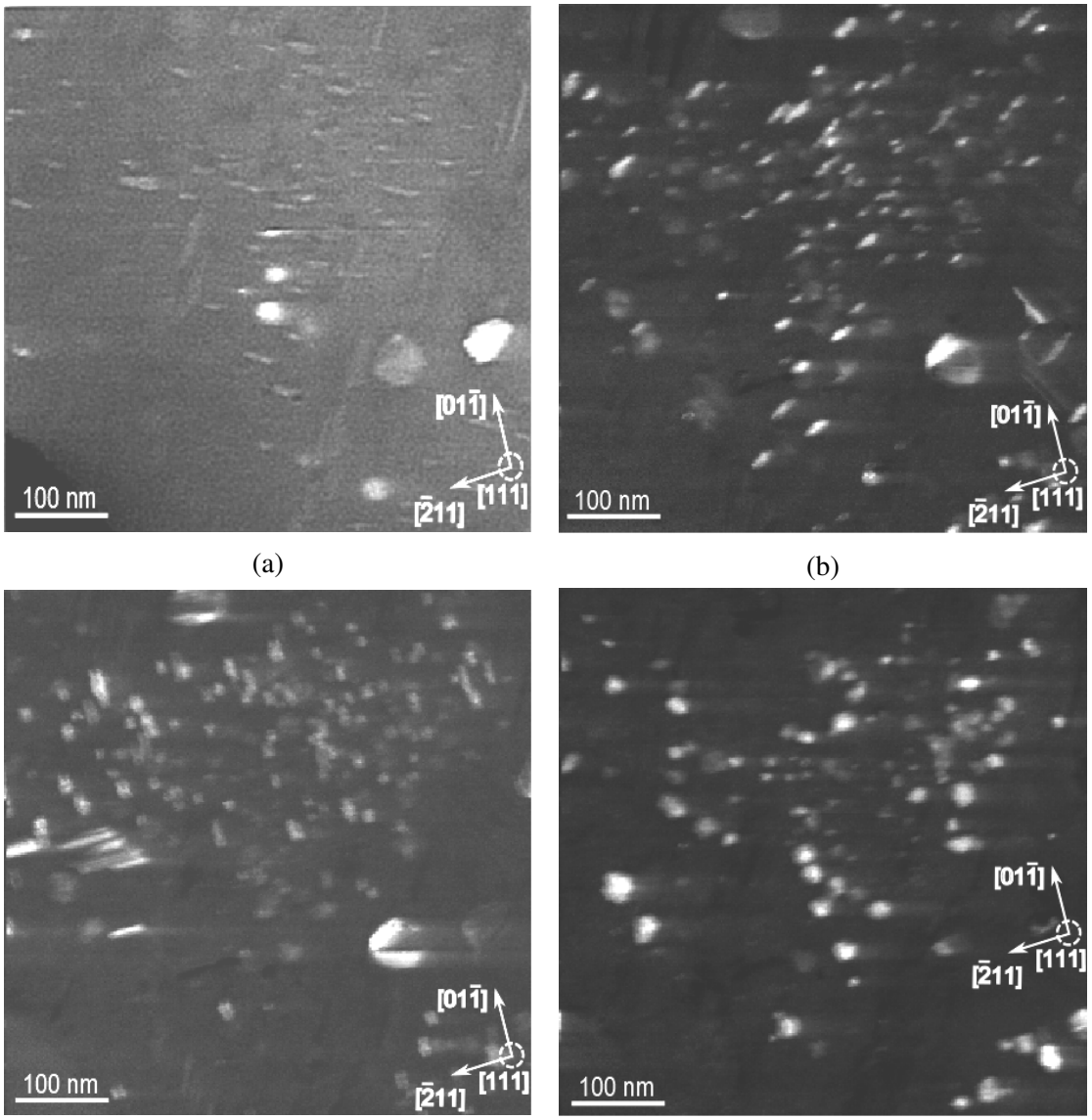

Figure A.11: VDF (a) and BSS loading maps (b-d) showing the four unique orientations of Ω-precipitates near the $[111]_{Al}$ ZA in alloy MCA. (a) $(-111)_{Al}$ Ω-precipitate plates. (b) $(1\text{-}11)_{Al}$ Ω-precipitate plates. (c) $(11\text{-}1)_{Al}$ Ω-precipitate plates. (d) $(111)_{Al}$ Ω-precipitate plates. The scanned area is equal to that of figure A.10.

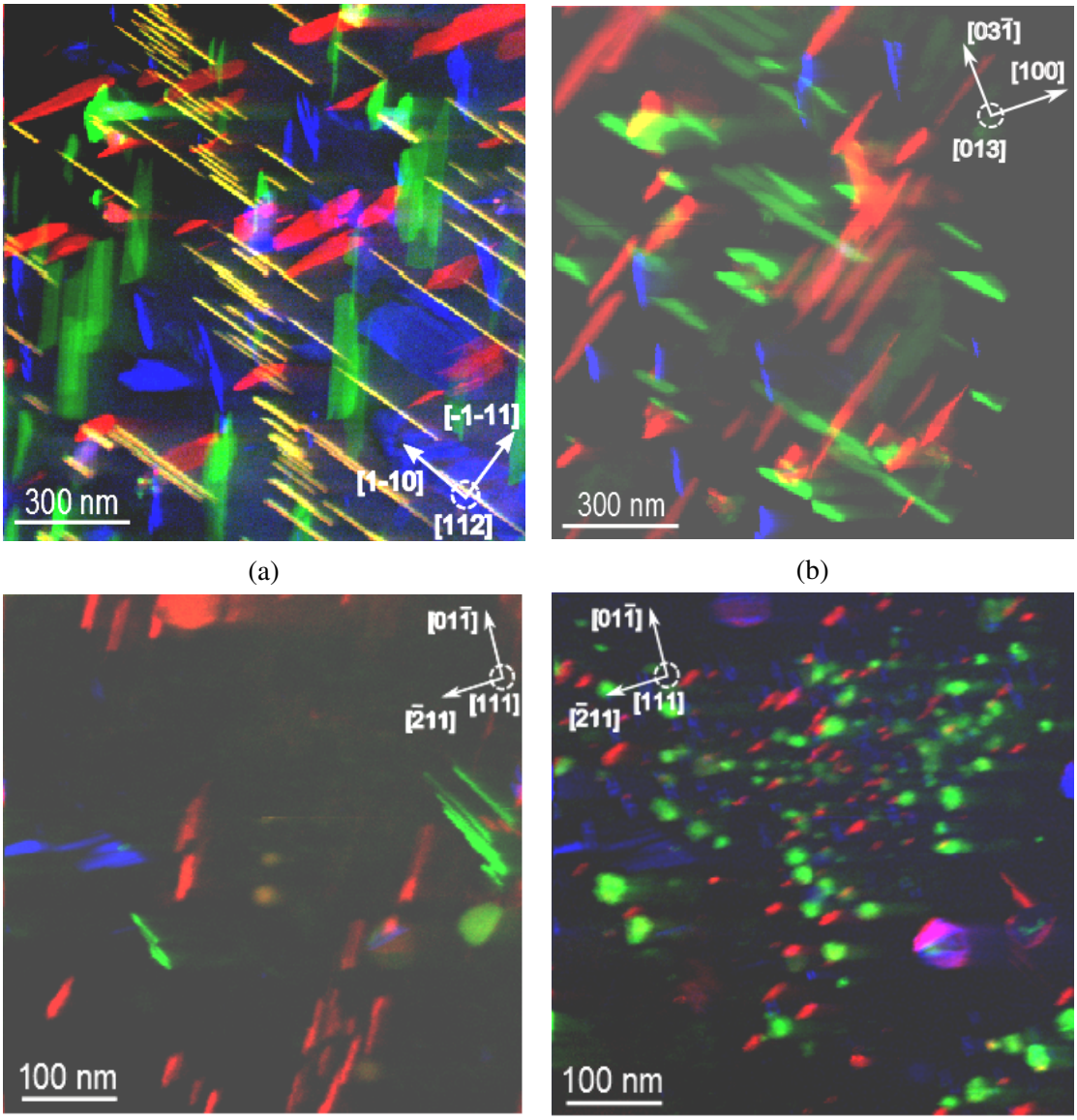

Figure A.12: (a) through (d): Constructed RGB images highlighting the coexisting precipitates within the Al matrix near the $[112]_{Al}$ and $[013]_{Al}$ ZAs in alloy CL (a-b), and near the $[111]_{Al}$ ZA in alloy MCA (c-d). The images have been formed using the individual phase orientations of figures A.8 through A.11.

Appendix B

Semi-Automatic Method for Obtaining Precipitate Statistics

A main interest with microstructure analysis of Al alloys is to obtain quantitative statistical information on key precipitates existing in the alloy after a given material pretreatment. Among the key parameters are; number densities (#/nm^3), volume fractions (%) and precipitate dimensions (nm). As has been thoroughly emphasized throughout this thesis, these precipitate parameters have a crucial impact on the macroscopic properties of Al alloys. This information serves as input for the improvement upon existing, or in the development of new, state-of-the-art Al alloys.

Depending on the existing precipitate morphologies and orientations, the applied imaging technique for obtaining statistical data varies. However, the general approach is to obtain high-quality images from several key ZAs, giving accurate individual precipitate dimensions. Having acquired several images providing such information on a statistically significant number of precipitates, the following procedure is to extract the quantitative information through manual counting and measurement of precipitate dimensions. More automated approaches include image pre-processing, e.g. by colouring the individual precipitates in MS paint or Adobe Photoshop, and to further run image characterization scripts providing the sought statistical information contained in the image.

The goal is reasonably to obtain this information as accurately, and from a large as possible distribution of precipitates. However, the existing manual counting and measurement procedure quickly becomes time consuming. It is therefore highly attractive to develop more automated procedures which could yield information from a larger distribution in a more time efficient manner. The obtained results could hence obtain higher certainties in calculated statistics. Sampling from a larger area and from several grains would average over differing statistics resulting from local effects such as precipitate clustering on dislocations, PFZs, etc.

This appendix suggests a possible step towards a more objective data extraction, by showing a semi-automated method for obtaining precipitate statistics. The method suggestion came about in observing the great 'noise reduction' properties of the BSS algorithm, as applied on the SPED datasets. A simpler idea in obtaining an automated statistics procedure, is to threshold high-quality DFTEM images of the main precipitates taken at key orientations. The thresholding, as applied for instance through the Digital Micrograph software, enables an automated precipitate highlighting based on the image intensities. Having highlighted individual precipitates allows for simple image processing scripts to extract the sought information on precipitate statistics.

The struggle with DFTEM images however, is the inconsistency in S/N ratios, and the unavoidable high background intensity. This problem arises due to difficulty with obtaining ideal aperture placements in the TEM. Precipitate reflections can be very weak compared to the strong Al reflections, and placing the aperture guided by the DP on the fluorescent screen can be challenging when trying to isolate the precipitate reflection. Due to the inconsistent S/N ratio, a problem arises as the background often approach the intensity of the selected precipitates in certain image points. This renders thresholding of precipitates less valuable, and hence one must resort to manual measurements.

However, the loading maps obtained through the BSS algorithm acting on the high-quality SPED datasets, achieve a significantly improved S/N ratio consistency, and a low background intensity. This allows for greatly improved intensity thresholding, see figure B.1.

Having a satisfactory thresholding allows for easy obtainable precipitate statistics. In using the Digital Micrograph software, one can further select the precipitates best outlined through the thresholding. After selection, 'Analyze Particles' with customizable display parameters gives precipitate measurements. Mathematical procedures including Max, Min, Std. Dev., Mean, etc. can further be run on selected precipitates thus giving sought information.

An inconvenient problem arises when the precipitates cross one another, or are located in close proximity. Simple thresholding will not distinguish these as separate, and further pre-image treatments are necessary for precipitate calculations. A quick fix suggestion is to save the optimal thresholded images as .bmp-files. Then, simply colouring the boundary between coalescent precipitates, thus separating them, prior to image script calculations. Combined with thickness measurements, as obtained through e.g. log-ratio electron energy loss spectroscopy or CBED methods, yields full precipitate statistics from the area of interest.

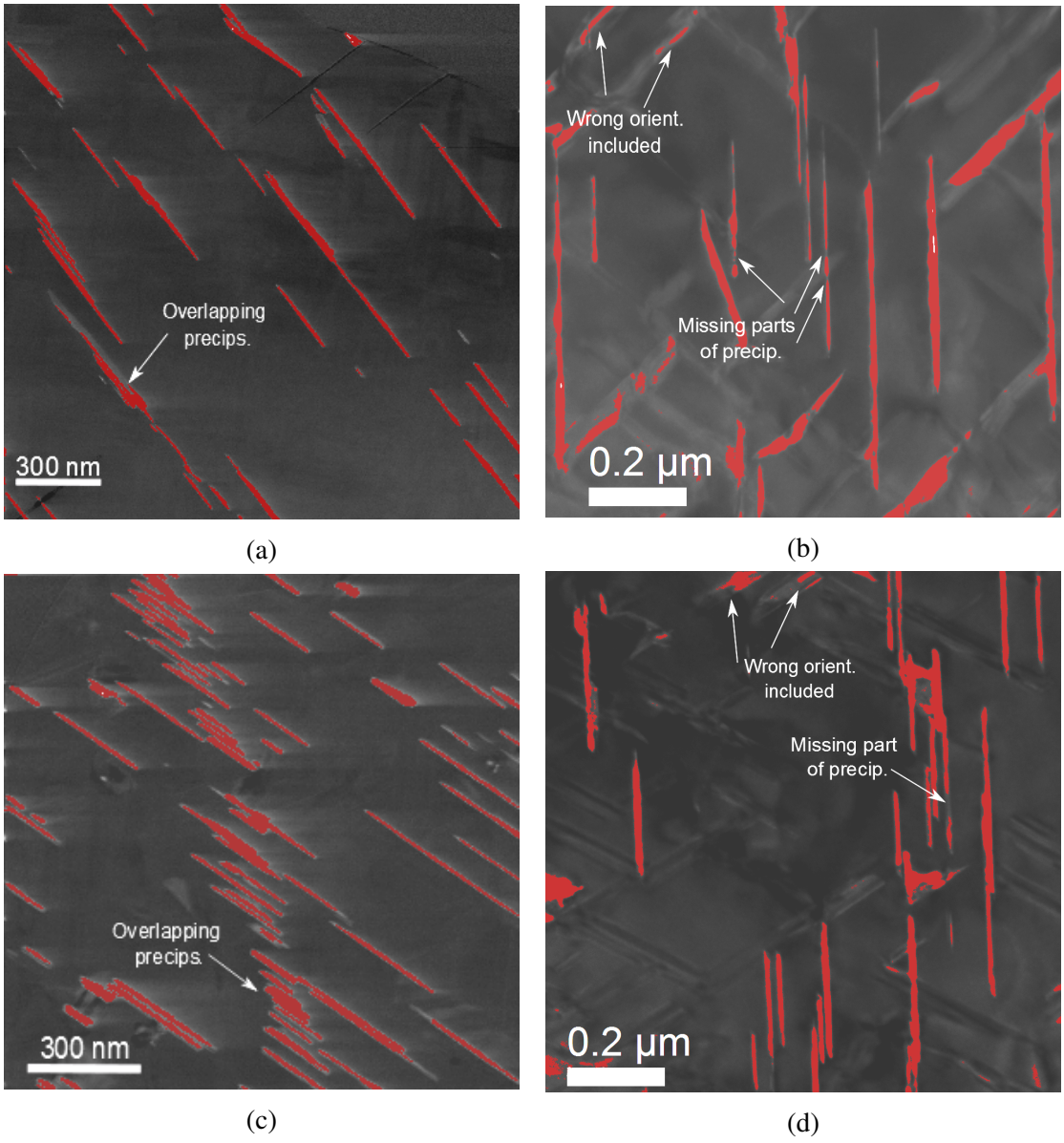

Figure B.1: (a) through (d): Thresholding of loading maps obtained through BSS, and of DFTEM images. (a) and (b) show a loading map and a DFTEM image respectively of θ'-precipitates oriented near the $[001]_{Al}$ ZA. (c) and (d) show a loading map and a DFTEM image respectively of T1-precipitates oriented near the $[112]_{Al}$ ZA.